Multifrequency Raman Generation in the Transient Regime

by

Fraser Cunningham Turner

A thesis
presented to the University of Waterloo
in fulfilment of the
thesis requirement for the degree of
Master of Science
in
Physics

Waterloo, Ontario, Canada, 2006

Author's Declaration for Electronic Submission of a Thesis

I hereby declare that I am the sole author of this thesis. This is a true copy of the thesis, including any required final revisions, as accepted by my examiners.

I understand that my thesis may be made electronically available to the public.

Abstract

Two colour pumping was used to investigate the short-pulse technique of Multifrequency Raman Generation (MRG) in the transient regime of Raman scattering. In the course of this study we have demonstrated the ability to generate over thirty Raman orders spanning from the infrared to the ultraviolet, investigated the dependence of this generation on the pump intensities and the dispersion characteristics of the hollow-fibre system in which the experiment was conducted, and developed a simple computer model to help understand the exhibited behaviours. These dependence studies have revealed some characteristics that have been previously mentioned in the literature, such as the competition between MRG and self-phase modulation, but have also demonstrated behaviours that are dramatically different than anything reported on the subject. Furthermore, through a simple modification of the experimental apparatus we have demonstrated the ability to scatter a probe pulse into many Raman orders, generating bandwidth comparable to the best pump-probe experiments of MRG. By using a numeric fast Fourier transform, we predict that our spectra can generate pulses as short as 3.3fs, with energies an order of magnitude larger than pulses of comparable duration that are made using current techniques.

Acknowledgements

First and foremost, I wish to thank my supervisor Dr. Donna Strickland for the fantastic experience I have had working in her research lab. Under her guidance I had the opportunity to participate in conferences and collaborations that have served to advance my professional skills and experience, far beyond what I expected when I first came to Waterloo. Her patience with my frequent visits (and the occasional argumentativeness), coupled with her endless encouragement has allowed me to feel free to express my opinions and explore what I felt to be important, and for this freedom I am very grateful.

I would also like to thank Dr. Joseph Sanderson, whom in essence was my second supervisor, always willing to discuss my work and lend a wrench or waveplate when needed. Many parts of this experiment were developed or maintained by his group, such as the hollow-fibre apparatus, its vacuum system, and the front-end oscillator. Without these contributions, this experiment would not have been available to me for my Masters.

For being on my defence committee and giving excellent suggestions for this thesis, I wish to thank Dr. Kostadinka Bizheva, Dr. Joseph Sanderson, and Dr. Donna Strickland. I also wish to thank Dr. Jim Martin for being on my Masters committee these last two years.

I sincerely thank Dr. Alexandre Trottier for training me in the particulars of using this laser system, and for his extensive input and development of this experiment. As well, I would like to thank Dr. Leonid Losev, for his original idea to use this laser system to study MRG, his assistance in the experiment, and the use of one of his published figures (Figure 2-3).

A wholehearted thank you goes to the community of students and staff at the University of Waterloo, who have helped with this project through useful discussions, assistance in the building, maintaining, and conducting the experiment, or for their own work towards the developing the apparatus. In particular I would like to thank Andy Colclough, Rob Helsten, Steve Walker, JP Brichta, Jeremy Roth, Owen Cherry, Jeff Carter, and all of the professionals in the Machine and Electronics shop of the University of Waterloo.

I would also like to thank Newport for the use of one of its illustrations (Figure 4-1).

Table of Contents

List of Illustrations

1. Introduction to Multifrequency Raman Generation

1.1. Historical Context

The field of high-intensity laser systems has been of keen interest to researchers since the original harnessing of stimulated emission [Gordon 1954]. With the development of the laser [Maiman 1960], the unprecedented intensities available in the optical regime quickly led to research in non-linear optical processes, such as second harmonic generation [Franken 1961]. As these effects depend on the intensity of the laser as opposed to simply the energy, the growth of this field depended not only on increasing the output from lasers but also on the development of techniques that shortened the pulses in time. Within the first few years of developing the laser, the key short-pulse techniques of Q-switching [McClung 1962] and mode-locking of lasers in the optical regime [Hargrove 1964] had become established, quickly reducing the pulse lengths from their original microsecond time-scale [Maiman 1961] down to a few picoseconds [Armstrong 1967]. Further advances in laser technology allowed researchers to take advantage of these short timescales to generate solid-state lasers with peak powers approaching 1TW [Seka 1980] – almost a 9 order of magnitude increase from the original 5kW laser [Maiman 1961]. At these incredible powers however, the nonlinear index of refraction – an effect present in all bulk materials – causes a self-focussing of the wavefront as it passes through the gain medium, resulting in a reduced beam quality and possible damage to the crystals themselves [Fleck 1973]. This effect put major constraints on high-power systems, necessitating the use of multiple beams to increase the power delivered in high-intensity experiments [Speck 1981].

These TW-scale lasers developed in the 1970s often used pulses with durations in the tens to hundreds of picoseconds range, relying more on increasing the energy in the pulse than decreasing its length to achieve higher intensities. At the same time as these advances were being made, the alternative pulse-duration approach to high intensity lasers was steadily maturing – reaching the 100 femtosecond mark around the same time as the laser fusion facilities were operational [Fork 1981], and breaking 10fs a few years later through the combination of self-phase modulation in single-mode fibres, and pulse compression techniques utilizing negative dispersion [Treacy 1969; Fork 1984; Knox 1985]. At this point the discovery of the impressive lasing properties of titanium-doped sapphire crystals (Ti:Sapphire) [Lacovara 1985], and the development of Chirped Pulse Amplification

[Strickland 1985], allowed for significant advances over the current state of the art dye lasers and doped-glass lasers. The ability to avoid self-focussing by stretching the pulses before amplification quickly resulted in tabletop laser systems reaching close to 1TW [Maine 1988], while the unprecedented bandwidth available in Ti:Sapphire lasers eventually propelled short-pulsed laser systems to the petawatt level [Perry 1999].

Out of this ultrafast boon also emerged the study of the time evolution of ultrafast processes, such as observing the transition-state dynamics of chemical reactions and molecular motion [Zewail 1991]. Analogous to the shutter speed of a camera, shorter pulses allowed for faster snapshots of these processes, providing further motivation to generate as short a pulse as possible. While techniques utilizing self-phase modulation and adaptive compression would eventually produce pulses with durations of 2.8fs [Yamashita 2006], a fundamental limit was being reached as these pulses approached a single cycle of their central frequency. To achieve a pulse with a duration of half an optical period, which in the case of Yamashita et al (2006) was 1fs, the laser would require a bandwidth equal to twice that of the central frequency, stretching from 0Hz to $2\omega_0$. Any further decrease in the pulse duration would therefore require a shift to a higher central frequency, however as the technique of self-broadening in hollow waveguides is a relatively mature technology [Nisoli 1996], any significant improvement in the pulse duration would require new techniques to generate these large bandwidths at much shorter wavelengths.

The most promising technique in the push to break this 1fs barrier grew out of the effort to produce coherent short-wavelength radiation for x-ray spectroscopy [Harris 1973]. It was found that when an intense IR laser was focussed into a gas, many harmonic orders of the pump frequency were generated in a characteristic way: the intensity of the first number of harmonics dropped rapidly, but eventually levelled off into a plateau until finally reaching some cut-off intensity [Ferray et al. 1988]. It was soon realized that the bandwidth generated with this High-Harmonic Generation (HHG), could produce temporal structure on the scale of tens of attoseconds if properly phased [Farkas 1992]. The resulting pulse could then be used as a probe for processes on the timescale of a Bohr orbit of an electron! With a deeper understanding of the dynamics involved [Corkum 1993], it was realized that the generated vuv/X-ray radiation would need minimal phase control, and that while it might not be perfectly phased, it should automatically produce a train of pulses with durations of hundreds of attoseconds [Corkum 1994]: an order of magnitude shorter than those

generated using continuum techniques. The ensuing development eventually led to the isolation and measurement of a single attosecond-scale pulse [Hentschel 2001], and a record pulse duration of 250as [Kienberger 2004].

While this technique has provided unprecedented access to short timescales, its major drawback lies in the relatively low energy in the pulses, as the conversion efficiency into usable radiation is quoted as being anywhere from 10^{-3} to 10^{-8} [Kaplan 1996; Shon 2002; Sali 2005]. This low conversion is also a shortcoming of the latest continuum generation pulses, where each decrease in the pulse length accompanies a dramatic drop in energy: from 5.3fs with 300μJ [Rauschenberger 2006], to 3.8fs with 25μJ [Steinmeyer 2006], to 2.8fs with 0.5μJ [Yamashita 2006]. However, it is the conversion efficiency in which the technique of Multifrequency Raman Generation (MRG) excels, providing access to timescales on the order of a femtosecond while allowing conversion of the pump into usable broadband radiation with efficiencies approaching 100% [Losev 1993; Nazarkin 1999a]. Having demonstrated the generation of pulse trains with pulses as short as 1.6fs [Shverdin 2005], and isolated pulses comparable to the best synthesized using continuum generation [Zhavoronkov 2002], new developments in MRG are showing the potential to generate few-femtosecond pulses with an order of magnitude more energy than current state-of-the-art techniques [Turner 2006].

1.2. General Description of MRG

Coined in the early 90s [McDonald 1994], the technique of Multifrequency Raman Generation refers to the generation of a large number of optical frequencies by irradiating a medium with a two laser beams tuned to a two-photon Raman resonance. Through stimulated Raman scattering, the two beams couple the ground and Raman state and then immediately scatter into their corresponding Stokes and anti-Stokes orders. With sufficient intensities, this process cascades as these generated orders scatter into their own Stokes and anti-Stokes frequencies, eventually generating enough bandwidth to span the entire visible spectrum [Imasaka 1989]. This process is demonstrated schematically in Figure 1-1, which depicts higher-order anti-Stokes scattering as a cascaded third-order nonlinearity. One way to visualize this process is that a pump photon first gives some energy to the molecule (excites it to its Raman state), by becoming a Stokes photon, and then another pump photon takes away that energy to become an anti-Stokes. It can then happen that another pump

photon excites the molecule, but instead the anti-Stokes photon generated before absorbs the energy, producing a second-order anti-Stokes photon.

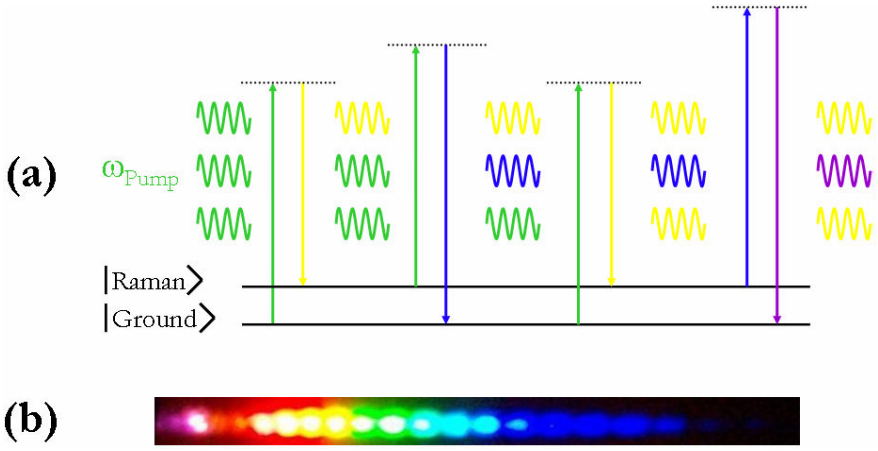

Figure 1-1: (a) Schematic representation of cascaded anti-Stokes scattering in MRG. Colours from red to violet are taken to be increasing in energy. Assumed in the diagram is that the scattering of the pump beam is stimulated by the introduction of its Stokes radiation at $\omega_{Stokes} = \omega_{Pump} - \omega_{Raman}$ (b) Example of a discrete MRG spectrum as dispersed by a prism. The orders shown in light purple are actually in the infrared. This picture was taken in the laboratory of Dr. Strickland.

Alternatively one could consider a classical picture, where the beating two-colour pump beam excites (for example), vibrations in the molecules of interest. The oscillating molecules will then act as a frequency modulator, impressing sidebands on the pump beams in much the same way that acoustic vibrations can be used to phase modulate radio waves in frequency-modulated (FM) radio. A good experimental demonstration of this FM-like behaviour is reported in Nazarkin et al (1999), where a probe injected into excited molecules generated a spectrum strikingly similar to that produced in FM radio (for a good illustration of an FM spectrum, see http://cnyack.homestead.com/files/modulation/modfm.htm). This can be thought of as being due to the change in the index of refraction as the molecule oscillates – as a larger index of refraction corresponds to slower light, the phase of the injected probe is being periodically delayed or pushed forward as the molecule gets bigger or smaller, as illustrated in Figure 1-2.

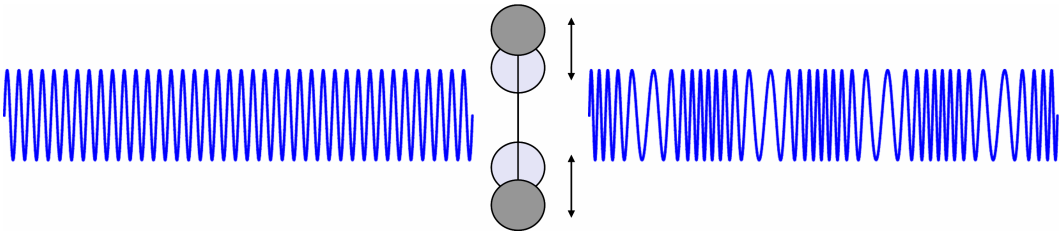

Figure 1-2: Vibrating molecule frequency-modulating an input probe

These descriptions contain the core of the physics that produces this ultra-broad bandwidth, however in practice MRG is split into three distinct regimes depending on the duration of the pump pulses relative to the natural timescales characteristic of molecules. Given the long pulses characteristic of early laser systems, the first regime to be accessed was the adiabatic (or steady-state) regime, which is defined by pulses of durations that are longer than the dephasing time of the molecules ($\boldsymbol{T}_2$). This dephasing time is dominated by effects such as intra-molecular vibrational relaxation or collisions that act to incoherently interrupt the molecular motion, and as such is typically on the scale of picoseconds to nanoseconds [Zewail 1995]. As the pulses become shorter than this dephasing time the transient regime is reached, characterized by pulses that while shorter than this coherence time are still longer than the vibrational period. When the pulses become shorter than a single oscillation of the molecule, the impulsive regime of stimulated Raman scattering is reached [Yan 1985], where in fact each pulse automatically contains frequencies that match the two-photon resonance. As such, only one pump pulse is necessary to generate the Raman excitation.

An alternative approach to visualizing these regimes is given in Figure 1-3, where an energy-level picture is used to demonstrate the difference between them. Absorption and emission of photons are demonstrated by the direction of the arrows, and the bandwidths (or in the case of the excited state the linewidth), are schematically represented using the thickness of the corresponding lines. Note that the bandwidth is inversely related to the pulse duration, so larger bandwidths correspond to shorter pulses . The adiabatic regime in (a) is characterized by pulses with bandwidths smaller than the Raman linewidth of $1/\boldsymbol{T}_2$, and is often described using a detuning δ from the two-photon resonance, where in the diagram δ is depicted as negative according to the convention of Harris & Sokolov (1997). Pulses in the transient regime have bandwidths that are larger than the Raman linewidth but not large enough to span the entire Raman transition. In the impulsive regime only one pulse is necessary, for when the pulse is shorter than a single oscillation of the molecule, it must automatically posses a bandwidth is larger than the Raman separation $\omega_{Raman} = \left(\boldsymbol{E}_{Raman} - \boldsymbol{E}_{Ground}\right)/\eta$.

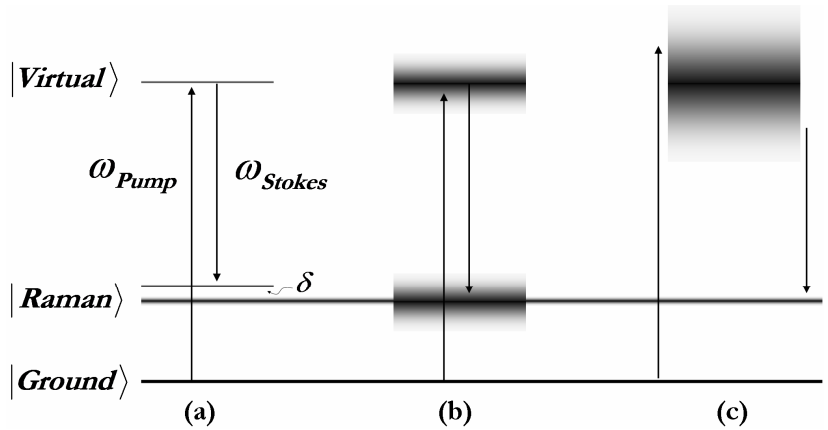

Figure 1-3: Energy level diagram of MRG. (a) Adiabatic, (b) transient, and (c) impulsive regimes.

1.3. Historical Development of MRG

A third-order nonlinear effect, higher-order stimulated Raman scattering was observed soon after the development of high-power laser pulses via the process of Q-switching, a technique where energy is allowed to build up in the gain medium before letting the laser generate a beam [McClung 1962]. It was found that by focussing these high-power pulses into a Raman-active medium, a large number of Stokes and anti-Stokes orders would be generated [Terhune 1963]. To conserve momentum, these orders would emerge at particular phase-matching angles dictated by the dispersion of the nonlinear index of refraction [Maker 1965], and as such would not be focusable to a single spot (see Figure 1-4). This precluded using this radiation as a single multifrequency beam, however the tremendous bandwidths generated – broader than the entire visible spectrum [Johnson 1967] – had significant implications for those developing tuneable radiation in the infrared and ultraviolet regions of the spectrum [Schmidt 1974; Mennicke 1976].

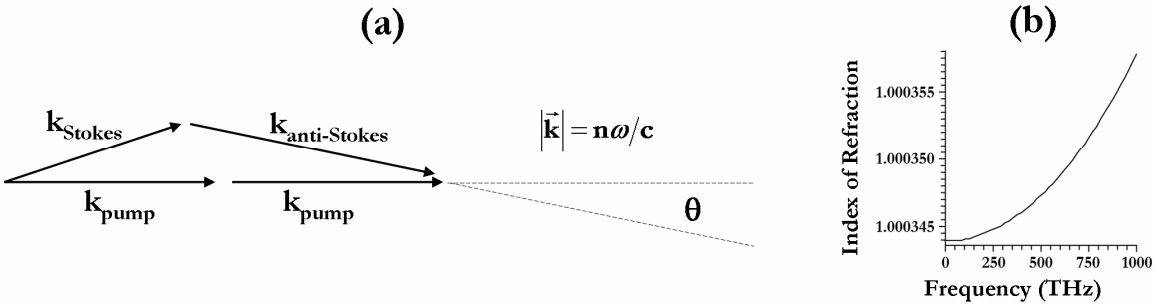

Figure 1-4: Origin of the phase-matching angles. (a) Momentum conservation diagram for two pump photons to make a Stokes and anti-Stokes. (b) While each order is separated by a constant frequency, their momenta are not equally separated due to a frequency-dependent index of refraction

As this process typically relied on the generation of the Stokes radiation through spontaneous Raman scattering [Bloembergen 1967], the high intensities required to start the process complicated the resulting emission, as it generated a number of other nonlinear effects such as self-focussing and Rayleigh-wing scattering [Minck 1966]. With the goal of acquiring more control over this process, it was found that the application of a weak Stokes beam from another laser significantly reduced the threshold for the cascaded four-wave mixing, and allowed one to study stimulated Raman scattering in the absence of other nonlinear effects. This technique of supplying a Stokes seed to stimulate the process found application in the spectroscopic technique known as CARS (coherent anti-Stokes Raman spectroscopy), which identifies Raman transitions by using a tuneable Stokes beam in conjunction with a pump laser [Akhmanov 1972; Wynne 1972].

The intensities of the of the tuneable lasers typically used in the CARS technique were relatively moderate, but with improved experimental setups and more powerful beams it was observed that along with the light produced at the phase-matched angles, MRG could occur in a collinear fashion, albeit with a small phase mismatch, such as shown in Figure 1-5 [Aussenegg 1981]. While this phase mismatch eventually makes the light destructively interfere with itself and restricts the generated bandwidth, it does allow for the generation of a single multifrequency beam. With the suggestion that the Raman orders should be phase locked – meaning that from shot-to-shot the phases across the spectrum should be reproducible – MRG began to receive a lot of attention as a potential technique for the production of ultrashort pulses [Yoshikawa 1993].

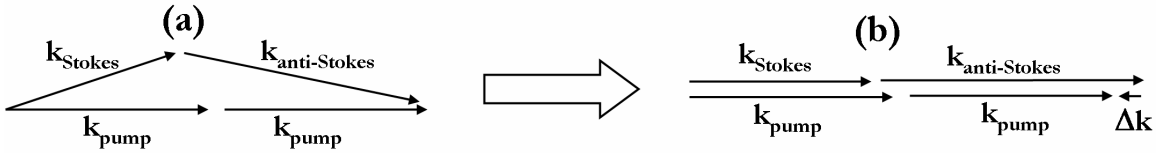

$$\Delta \mathbf{k} = 2\mathbf{k}_{\mathbf{Pump}} - \mathbf{k}_{\mathbf{Stokes}} - \mathbf{k}_{\mathbf{anti-Stokes}}$$

Figure 1-5: Two configurations for generating sidebands. (a) The orders are produced at the phase-matched angle. (b) The orders are produced with a slight phase mismatch Δk

The first model developed to predict the generation of this ultra-broad bandwidth was based on a perturbative classical description of the interaction between light and matter [Losev 1993]. Presented along with an experimental investigation in the adiabatic regime, it was found that their simulations significantly overestimated the generated bandwidth, a

discrepancy which was attributed to the effect of diffraction. A two-dimensional simulation confirmed this, demonstrating that the spatially-dependent Raman gain of a Gaussian beam combined with the effect of diffraction would produce complex ring structures in the beam, which in turn suppressed the generation of higher orders [Syed 2000]. This Raman defocusing effect was studied experimentally soon afterwards, demonstrating a significant increase in the beam diameter with increasing Stokes order, as well as the significant decrease in generated bandwidth for more tightly-focused pump beams [Losev 2002a]. It is because of this detrimental effect that many future experiments in MRG used hollow dielectric waveguides (hollow fibres) filled with a Raman-active gaseous medium, confining the generated spectrum in a single guided mode (therefore forcing it to be collinear as in Figure 1-5b), as well as increasing the interaction length from the diffraction limit to approximately one meter [Nazarkin 1999; Sali 2004].

With a solid theoretical model behind them, investigations immediately ensued into the possibility of conducting MRG with shorter pulses, which would allow for higher intensities and therefore increasing the strength of the nonlinear interaction. While it was found that the generated bandwidth was even more sensitive to dispersion in the transient regime as compared to the adiabatic [McDonald 1994], it was also predicted that the bandwidth could be enhanced by a factor of 1.4 in the case of zero dispersion [Losev 1996]. As attractive as this enhancement was, the experimental difficulties in producing two ultrafast laser pulses separated by a relatively small frequency shift delayed efforts to study this regime until recently [Losev 2002b].

In parallel with the classical description of MRG, an alternative approach based in the density matrix formalism of the Maxwell-Bloch equations suggested the exciting possibility that this multifrequency beam could spontaneously generate bright few-cycle solitons. These static solutions for the electric field result in a pulse containing many Raman orders that propagate at the same group velocity, due to a balance between the nonlinear, frequency-dependent effect of MRG and the linear effect of dispersion [Kaplan 1994]. The observation of these solitons would be a major advance in the field of ultrafast lasers, partly because the complicated phase-correction techniques typical of other few-cycle schemes would be unnecessary, but predominantly because it has been predicted that these pulses would have durations as short as 200as – an order of magnitude shorter than anything that had been observed at the time. As such, these stationary solutions received considerable

theoretical attention in the coming years in the steady-state regime [Kaplan 1996; Yavuz 2000] and in systems that can demonstrate negative dispersion [Nazarkin 1999b]. Soliton formation has also been studied in the transient regime, however it is instead each order that breaks into a soliton train [McDonald 1995], as opposed to multiple orders becoming locked into a single train of solitons travelling at a specific group velocity.

Using the same density-matrix formalism, the simulations of Harris & Sokolov (1997) demonstrated the generation of bandwidths that were comparable to those predicted by Losev & Lutsenko (1993), however their subsequent experimental investigations achieved significantly more conversion than previously reported especially into the anti-Stokes orders [Sokolov 2000]. Indeed, further development of their technique resulted in the most impressive demonstration of MRG to date, producing over 200 Raman orders using a combination of two Raman-active media and three pump pulses [Yavuz 2003]. In the course of their investigations they were also able to demonstrate the synthesis of ultrashort pulses by properly phasing the distinct Raman orders, first producing a pulse train consisting of 2fs pulses by using a series of prisms and delay lines overlap the orders in time [Sokolov 2001], and eventually generating a train of 1.6fs pulses using a liquid-crystal spatial light modulator to adjust their phases [Shverdin 2005].

While these constitute the shortest pulses ever produced with MRG, their main drawback lies in the duration of the pump pulses as compared to the Raman period. As the Raman period dictates the separation between consecutive pulses and the duration of the pump dictates the number of these pulses generated, the 11fs vibrational period of the deuterium they used would produce approximately one million pulses within their 10ns pump pulses. Each ultrashort pulse would then contain an average energy of ~100nJ, minimizing their usefulness as an experimental tool. Soon after the initial adiabatic demonstration however, pulses of a similar duration but an order of magnitude more energy were obtained by another group, who instead of working with ns pumps were using impulsive excitation to generate ultrashort pulses [Zhavoronkov 2002].

Intrinsically, impulsive MRG is less suitable for the generation of ultrashort pulses than continuum generation or even adiabatic MRG, as the interaction between MRG and self-phase modulation (SPM) leads to a suppression of both the high-frequency wing characteristic of SPM, and the high order anti-Stokes scattering characteristic of MRG [Korn 1998; Kalosha 2003]. It is with an alternative pump-probe setup that impulsive excitation

has a real advantage, where the relatively mature pump sources at ~10fs [Rauschenberger 2006], are used simply as a tool to excite a coherence in the system, and it is instead the scattering of a probe pulse injected behind the impulsive pump that is of interest [Nazarkin 1999a]. This pump-probe scattering is qualitatively different than typical MRG, in that from the point of view of the probe, the scattering is essentially a linear process as opposed to a non-linear one [Wittmann 2000; Nazarkin 2002a]. That is, the impulsive pump provides the two photons coupling the ground and excited state, and the probe only needs to supply the third photon to scatter into its Stokes and anti-Stokes orders (see in Figure 1-1a for anti-Stokes scattering). In this linear scattering regime, compression of the radiation into few-femtosecond pulse trains required either the application of positive *or* negative group-velocity dispersion (GVD), which could be accomplished by simply propagating the pulses through a dispersive medium for positive GVD, or by using commercially available chirped mirrors to supply negative GVD [Wittmann 2000; Wittmann 2001]. The symmetric nature of this compression is a consequence of the FM-like modulation experienced by the probe, which would periodically delay or advance the phase of the light (see Figure 1-2 for an illustration of this modulation).

By reducing the duration of the probe to where it was shorter than a single molecular oscillation, this technique was able to generate an isolated few-femtosecond pulse [Zhavoronkov 2002]. With a phase modulation that is no longer periodic (as the probe only exists for a fraction of the molecular oscillation), a more continuous spectrum is generated, which analogous to continuum generation allows the formation of a single pulse. In the course of that particular experiment a pulse with a duration of 3.8fs and an energy of 1.5μJ was synthesized. By utilizing the plasma-like dispersion in hollow fibres to match the group-velocity of the probe to the original pump beam, even shorter pulses may be possible using this technique [Nazarkin 2002b]. Another advantage of this technique is its scalability in terms of the probe frequency – given sufficiently short probes in the mid-infrared and uv regions of the spectrum, pulses of durations around 6fs and 2fs could be generated, which is not currently possible with other short-pulse techniques [Kalosha 2003]. While this operation in previously inaccessible frequency regimes is a major step forward for ultrafast science, the generated probes are still an order of magnitude less energetic than comparable continuum techniques. As there must be some way to disentangle the probe beam from the

pump, it is very difficult to apply in the range where higher-energy probes are most available – the 700-900nm range of the Ti: Sapphire lasers used to generate the impulsive pump beam.

Herein lies the advantage of a symmetric, transient pumping scheme with laser pulses of durations on the order of hundreds of femtoseconds. By selectively irradiating the medium with two pump pulses tuned to the Raman resonance, one can take full advantage of the high energies available in Ti:Sapphire pulses by avoiding the strong SPM characteristic of the impulsive regime, while producing a much shorter pulse train than is possible with nanosecond pumping. The first demonstration of transient MRG was in 2002 using a $KGd(WO_4)_2$ crystal (KGW), as the Raman-active medium [Losev 2002b]. Having earlier predicted that the generated bandwidth is maximized with the ratio of the pulse length to the dephasing time [McDonald 1994], the 1.3ps dephasing time of KGW made it very attractive as compared to the nanosecond dephasing time of many gasses. However, it was found that the sensitive nature of transient pumping to dispersion dominated the possible enhancement from the short dephasing time, and as such only a few orders were generated. Furthermore, the short pumps experienced a significant amount of self-phase modulation as they passed through the crystal, limiting the number of orders generated as compared to stretched pulses [Losev 2002b]. The detrimental effects due to the solid medium were remedied by conducting transient MRG in a hollow fibre filled with a Raman-active gas, where the generated orders spanned at least the wavelength range from 800nm to just below 300nm, from which it is predicted a 1fs pulse can be synthesized assuming perfect phase compensation [Sali 2004]. Further investigations confirmed the detrimental effect of SPM as the growth of the bandwidth with pressure halted with the onset of self-phase modulation, and also demonstrated the overall bandwidth generated with different media were approximately the same, even if the number of orders are different [Sali 2005].

With the demonstration that bandwidths spanning the visible spectrum can be obtained in the transient regime, experimental efforts are being directed towards optimizing and compressing this bandwidth. The investigations presented in this report are the most recent efforts of our group towards generating high-energy ultrashort pulses in the transient regime of MRG. Detailed in the following chapters is the culmination of my efforts towards these goals to date, including a theoretical discussion of the equations pertaining to the classical description of MRG, a computer model based on those equations aimed at explaining the results obtained in the laboratory, the first experimental demonstration of

transient MRG in SF_6 using our two-colour laser system, the scaling of this effect with intensity as reported in Turner et al (2006), the most recent results of its behaviour with pressure in a narrow hollow fibre, and some concluding remarks discussing the future directions of this research.

2. Theory

The theoretical treatment of Losev & Lutsenko (1993) provides a good starting point for understanding the MRG process. A relatively intuitive classical description of MRG, it provides much insight into the predominant mechanisms for the generation of multiple orders, and as well benefits from a parallel and detailed description in the text *Nonlinear Optics* [Boyd 2003]. **§2.1** will describe in detail how to arrive at the equations in Losev & Lutsenko (1993) by drawing upon the discussion in *Nonlinear Optics* from chapters 1, 2, and especially 10. After concluding with the general equations in **§2.1.4**, two characteristic behaviours of MRG – the Bessel-function character of the sidebands and an estimate of the total bandwidth – will be described drawing on a variety of resources. The discussion will then conclude with a description of the program developed to try and model the experimental results.

2.1. Classical description

When an electric field $\vec{E}(z,t)$ is incident upon a molecule, the electronic and nuclear response of this molecule creates a polarization field $\vec{p}(z,t)$ through its polarizability α (the tilde denotes a term that is rapidly-varying). If the driving electric field is much weaker than the atomic field $\left|\vec{E}_{atom}\right| = 2*10^7\ \textbf{statvolt}/\textbf{cm} = 6*10^{11}\ \textbf{V}/\textbf{m}$, the molecule's response can be described using a perturbative technique, where the polarization is related to the $\mathbf{n}^{\text{th}}$ power of $\vec{E}(z,t)$ through an $\mathbf{n}^{\text{th}}$-order tensor $\chi^{(n)}$. In an isotropic medium, this tensor nature is suppressed and the polarization can be expressed as

$$\tilde{p}(z,t) = \chi^{(1)}\tilde{E}(z,t) + \chi^{(2)}\tilde{E}^2(z,t) + \chi^{(3)}\tilde{E}^3(z,t) + O\left(\tilde{E}^4\right) \qquad \textbf{[Eq. 2-1]}$$

When discussing nonlinear effects due to this polarization, any that are related to the cube of the electric field will be referred to as *third-order* or $\chi^{(3)}$ (chi-3), nonlinearities. Note that $O\left(x^n\right)$ is meant to stand for "terms in x to the power of n and higher", and the vector notation has been dropped for clarity.

2.1.1. Driving Force and Molecular Motion

For the present derivation, consider the response of a vibrationally Raman-active diatomic molecule to a linearly polarized pump beam. The polarization field due to a single molecule

is given by its polarizability α through the relation

$$\tilde{\boldsymbol{p}}(\boldsymbol{z},\boldsymbol{t}) = \alpha(\boldsymbol{z},\boldsymbol{t}) \cdot \tilde{\boldsymbol{E}}(\boldsymbol{z},\boldsymbol{t}) \qquad \textbf{[Eq. 2-2]}$$

Note that for this derivation the medium is assumed to be isotropic (which corresponds to our experimental case of SF_6), and as such α is simply a scalar quantity. The key assumption in this derivation is that the polarizability should only be weakly dependent on the internuclear separation, as it is mainly a result of the electronic configuration of the molecule. Written to first order, the polarizability thereby has the form

$$\alpha(\boldsymbol{z},\boldsymbol{t}) = \alpha_0 + \left(\partial\alpha/\partial\boldsymbol{q}\right)_{q=q_0} \cdot \boldsymbol{q}(\boldsymbol{z},\boldsymbol{t}) \qquad \textbf{[Eq. 2-3]}$$

where $\boldsymbol{q}$ is the vibrational coordinate given by

$$\boldsymbol{q}(\boldsymbol{z},\boldsymbol{t}) = \boldsymbol{q}_0 + \tilde{\boldsymbol{q}}(\boldsymbol{z},\boldsymbol{t}) \qquad \textbf{[Eq. 2-4]}$$

as in Figure 2-1. This leads to a polarization of

$$\begin{aligned}\tilde{\boldsymbol{p}}(\boldsymbol{z},\boldsymbol{t}) &= \alpha_0\tilde{\boldsymbol{E}}(\boldsymbol{z},\boldsymbol{t}) + \left[\left(\frac{\partial\alpha}{\partial\boldsymbol{q}}\right)_{q=q_0} \boldsymbol{q}(\boldsymbol{z},\boldsymbol{t})\tilde{\boldsymbol{E}}(\boldsymbol{z},\boldsymbol{t})\right] \\ &= \tilde{\boldsymbol{p}}_{\boldsymbol{Linear}}(\boldsymbol{z},\boldsymbol{t}) + \tilde{\boldsymbol{p}}_{\boldsymbol{Nonlinear}}(\boldsymbol{z},\boldsymbol{t})\end{aligned} \qquad \textbf{[Eq. 2-5]}$$

It will become convenient later to drop the linear part of the polarization, as it does not directly affect the MRG process (but does play a role through the index of refraction).

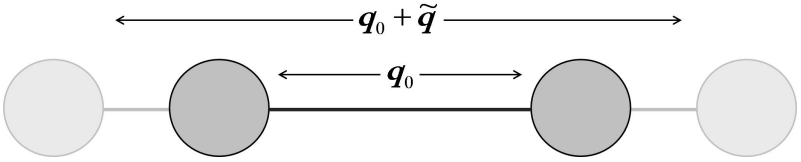

Figure 2-1: Vibrating diatomic molecule

Now, assume that the molecule acts like a simple harmonic oscillator with a single resonant frequency ω_V, reduced nuclear mass $\boldsymbol{m}$, and damping constant γ. Its motion from equilibrium $\tilde{\boldsymbol{q}}$ will follow the equation

$$\frac{\partial^2\tilde{\boldsymbol{q}}}{\partial\boldsymbol{t}^2} + 2\gamma\frac{\partial\tilde{\boldsymbol{q}}}{\partial\boldsymbol{t}} + \omega_V^2\tilde{\boldsymbol{q}} = \frac{\tilde{\boldsymbol{F}}(\boldsymbol{z},\boldsymbol{t})}{\boldsymbol{m}} \qquad \textbf{[Eq. 2-6]}$$

where the applied force $\tilde{F}(z,t)$ acts along the vibrational coordinate q. This force, which is generated by the electric field, can be found by taking the gradient of the work needed to create the polarization $\tilde{p}(z,t)$. Under the dipole approximation this can be written as

$$\tilde{F}(z,t) = -\frac{\partial W}{\partial q} = -\frac{\partial}{\partial q}\left(-\frac{1}{2}\left\langle \tilde{p}(z,t)\cdot\tilde{E}(z,t)\right\rangle\right) \qquad \textbf{[Eq. 2-7]}$$

where the angular brackets denote the time average over an optical period. By substituting the expressions for $\tilde{p}(z,t)$ and $\alpha(z,t)$, this reduces to

$$\tilde{F}(z,t) = \frac{1}{2}\left(\frac{\partial \alpha}{\partial q}\right)_0 \left\langle \tilde{E}^2(z,t)\right\rangle \qquad \textbf{[Eq. 2-8]}$$

. In typical experimental designs, MRG is produced by starting with two pump beams tuned to the Raman resonance, where $\omega_{pump} - \omega_{Stokes} = \Omega \approx \omega_V$ as in Figure 1-1. However it is useful to consider the case of four input fields of comparable intensity to facilitate the generalization of this effect. Therefore, consider a driving field that consists of a pump beam of index 0, a Stokes beam of index -1, an anti-Stokes beam of index +1, and a second-order Stokes beam of index -2. The notation and form of the electric field will be slightly modified from Boyd's description to help ease the transition to the notation of Losev & Lutsenko (1993), which was used to develop the computational model. Note that while the following equations are quite involved, the important information can simply be found by looking at the indices of the amplitude and phase terms to get a sense of what orders are involved.

Each component of this four-component electric field is taken to be of the form

$$\tilde{E}_N(z,t) = \frac{1}{2}\left(E_N\, exp\left[-i\left(k_N z - \omega_N t\right)\right] + E_N^*\, exp\left[i\left(k_N z - \omega_N t\right)\right]\right) \qquad \textbf{[Eq. 2-9]}$$

where the * denotes the complex conjugate. The frequencies are spaced approximately by the Raman frequency such that $\omega_N = \omega_0 + N\cdot\Omega$, where $\Omega \approx \omega_V << \omega_0$, and the wavevector $k_N = n(\omega_N)\cdot\omega_N / c$. The four-colour electric field can then be written as

$$\begin{aligned} 2\tilde{E}(z,t) = &\left(E_1\, exp\left[-i\left(k_1 z - \omega_1 t\right)\right] + E_1^*\, exp\left[i\left(k_1 z - \omega_1 t\right)\right]\right) \\ &+ \left(E_0\, exp\left[-i\left(k_0 z - \omega_0 t\right)\right] + E_0^*\, exp\left[i\left(k_0 z - \omega_0 t\right)\right]\right) \\ &+ \left(E_{-1}\, exp\left[-i\left(k_{-1} z - \omega_{-1} t\right)\right] + E_{-1}^*\, exp\left[i\left(k_{-1} z - \omega_{-1} t\right)\right]\right) \\ &+ \left(E_{-2}\, exp\left[-i\left(k_{-2} z - \omega_{-2} t\right)\right] + E_{-2}^*\, exp\left[i\left(k_{-2} z - \omega_{-2} t\right)\right]\right) \end{aligned} \qquad \textbf{[Eq. 2-10]}$$

where the amplitudes are approximately equal $|\boldsymbol{E}_1| \approx |\boldsymbol{E}_0| \approx |\boldsymbol{E}_{-1}| \approx |\boldsymbol{E}_{-2}|$. Note that in general the index of refraction is a nonlinear function of the frequency. In a more compact notation that will be often be used in this discussion, the electric field can be rewritten as

$$\begin{aligned} 2\tilde{\boldsymbol{E}}(\boldsymbol{z},\boldsymbol{t}) = {} & \boldsymbol{E}_1 \exp\left[-\boldsymbol{i}\left(\boldsymbol{k}_1\boldsymbol{z}-\omega_1\boldsymbol{t}\right)\right] + \boldsymbol{E}_0 \exp\left[-\boldsymbol{i}\left(\boldsymbol{k}_0\boldsymbol{z}-\omega_0\boldsymbol{t}\right)\right] \\ & + \boldsymbol{E}_{-1} \exp\left[-\boldsymbol{i}\left(\boldsymbol{k}_{-1}\boldsymbol{z}-\omega_{-1}\boldsymbol{t}\right)\right] + \boldsymbol{E}_{-2} \exp\left[-\boldsymbol{i}\left(\boldsymbol{k}_{-2}\boldsymbol{z}-\omega_{-2}\boldsymbol{t}\right)\right] \\ & + \boldsymbol{c.c.} \end{aligned} \quad \textbf{[Eq. 2-11]}$$

where the complex conjugate is denoted as c.c. The square of this field is then

$$\begin{aligned} 4\tilde{\boldsymbol{E}}^2(\boldsymbol{z},\boldsymbol{t}) = {} & \boldsymbol{E}_1^2 \exp\left[-\boldsymbol{i}\left(2\boldsymbol{k}_1\boldsymbol{z}-2\omega_1\boldsymbol{t}\right)\right] + \boldsymbol{E}_1\boldsymbol{E}_0 \exp\left[-\boldsymbol{i}\left(\left[\boldsymbol{k}_1+\boldsymbol{k}_0\right]\boldsymbol{z}-\left[\omega_1+\omega_0\right]\cdot\boldsymbol{t}\right)\right] \\ & + \boldsymbol{E}_1\boldsymbol{E}_{-1} \exp\left[-\boldsymbol{i}\left(\left[\boldsymbol{k}_1+\boldsymbol{k}_{-1}\right]\boldsymbol{z}-\left[\omega_1+\omega_{-1}\right]\cdot\boldsymbol{t}\right)\right] + \boldsymbol{E}_1\boldsymbol{E}_{-2} \exp\left[-\boldsymbol{i}\left(\left[\boldsymbol{k}_1+\boldsymbol{k}_{-2}\right]\boldsymbol{z}-\left[\omega_1+\omega_{-2}\right]\cdot\boldsymbol{t}\right)\right] \\ & + \left|\boldsymbol{E}_1^2\right| + \boldsymbol{E}_1\boldsymbol{E}_0^* \exp\left[-\boldsymbol{i}\left(\left[\boldsymbol{k}_1-\boldsymbol{k}_0\right]\boldsymbol{z}-\left[\omega_1-\omega_0\right]\cdot\boldsymbol{t}\right)\right] \\ & + \boldsymbol{E}_1\boldsymbol{E}_{-1}^* \exp\left[-\boldsymbol{i}\left(\left[\boldsymbol{k}_1-\boldsymbol{k}_{-1}\right]\boldsymbol{z}-\left[\omega_1-\omega_{-1}\right]\cdot\boldsymbol{t}\right)\right] + \boldsymbol{E}_1\boldsymbol{E}_{-2}^* \exp\left[-\boldsymbol{i}\left(\left[\boldsymbol{k}_1-\boldsymbol{k}_{-2}\right]\boldsymbol{z}-\left[\omega_1-\omega_{-2}\right]\cdot\boldsymbol{t}\right)\right] \\ \\ & + \boldsymbol{E}_0\boldsymbol{E}_1 \exp\left[-\boldsymbol{i}\left(\left[\boldsymbol{k}_0+\boldsymbol{k}_1\right]\boldsymbol{z}-\left[\omega_0+\omega_1\right]\cdot\boldsymbol{t}\right)\right] + \boldsymbol{E}_0^2 \exp\left[-\boldsymbol{i}\left(2\boldsymbol{k}_0\boldsymbol{z}-2\omega_0\boldsymbol{t}\right)\right] \\ & + \boldsymbol{E}_0\boldsymbol{E}_{-1} \exp\left[-\boldsymbol{i}\left(\left[\boldsymbol{k}_0+\boldsymbol{k}_{-1}\right]\boldsymbol{z}-\left[\omega_0+\omega_{-1}\right]\cdot\boldsymbol{t}\right)\right] + \boldsymbol{E}_0\boldsymbol{E}_{-2} \exp\left[-\boldsymbol{i}\left(\left[\boldsymbol{k}_0+\boldsymbol{k}_{-2}\right]\boldsymbol{z}-\left[\omega_0+\omega_{-2}\right]\cdot\boldsymbol{t}\right)\right] \\ & + \boldsymbol{E}_0\boldsymbol{E}_1^* \exp\left[-\boldsymbol{i}\left(\left[\boldsymbol{k}_0-\boldsymbol{k}_1\right]\boldsymbol{z}-\left[\omega_0-\omega_1\right]\cdot\boldsymbol{t}\right)\right] + \left|\boldsymbol{E}_0^2\right| \\ & + \boldsymbol{E}_0\boldsymbol{E}_{-1}^* \exp\left[-\boldsymbol{i}\left(\left[\boldsymbol{k}_0-\boldsymbol{k}_{-1}\right]\boldsymbol{z}-\left[\omega_0-\omega_{-1}\right]\cdot\boldsymbol{t}\right)\right] + \boldsymbol{E}_0\boldsymbol{E}_{-2}^* \exp\left[-\boldsymbol{i}\left(\left[\boldsymbol{k}_0-\boldsymbol{k}_{-2}\right]\boldsymbol{z}-\left[\omega_0-\omega_{-2}\right]\cdot\boldsymbol{t}\right)\right] \\ \\ & + \boldsymbol{E}_{-1}\boldsymbol{E}_1 \exp\left[-\boldsymbol{i}\left(\left[\boldsymbol{k}_{-1}+\boldsymbol{k}_1\right]\boldsymbol{z}-\left[\omega_{-1}+\omega_1\right]\cdot\boldsymbol{t}\right)\right] + \boldsymbol{E}_{-1}\boldsymbol{E}_0 \exp\left[-\boldsymbol{i}\left(\left[\boldsymbol{k}_{-1}+\boldsymbol{k}_0\right]\boldsymbol{z}-\left[\omega_{-1}+\omega_0\right]\cdot\boldsymbol{t}\right)\right] \\ & + \boldsymbol{E}_{-1}^2 \exp\left[-\boldsymbol{i}\left(2\boldsymbol{k}_{-1}\boldsymbol{z}-2\omega_{-1}\boldsymbol{t}\right)\right] + \boldsymbol{E}_{-1}\boldsymbol{E}_{-2} \exp\left[-\boldsymbol{i}\left(\left[\boldsymbol{k}_{-1}+\boldsymbol{k}_{-2}\right]\boldsymbol{z}-\left[\omega_{-1}+\omega_{-2}\right]\cdot\boldsymbol{t}\right)\right] \\ & + \boldsymbol{E}_{-1}\boldsymbol{E}_1^* \exp\left[-\boldsymbol{i}\left(\left[\boldsymbol{k}_{-1}-\boldsymbol{k}_1\right]\boldsymbol{z}-\left[\omega_{-1}-\omega_1\right]\cdot\boldsymbol{t}\right)\right] + \boldsymbol{E}_{-1}\boldsymbol{E}_0^* \exp\left[-\boldsymbol{i}\left(\left[\boldsymbol{k}_{-1}-\boldsymbol{k}_0\right]\boldsymbol{z}-\left[\omega_{-1}-\omega_0\right]\cdot\boldsymbol{t}\right)\right] \\ & + \left|\boldsymbol{E}_{-1}^2\right| + \boldsymbol{E}_{-1}\boldsymbol{E}_{-2}^* \exp\left[-\boldsymbol{i}\left(\left[\boldsymbol{k}_{-1}-\boldsymbol{k}_{-2}\right]\boldsymbol{z}-\left[\omega_{-1}-\omega_{-2}\right]\cdot\boldsymbol{t}\right)\right] \\ \\ & + \boldsymbol{E}_{-2}\boldsymbol{E}_1 \exp\left[-\boldsymbol{i}\left(\left[\boldsymbol{k}_{-2}+\boldsymbol{k}_1\right]\boldsymbol{z}-\left[\omega_{-2}+\omega_1\right]\cdot\boldsymbol{t}\right)\right] + \boldsymbol{E}_{-2}\boldsymbol{E}_0 \exp\left[-\boldsymbol{i}\left(\left[\boldsymbol{k}_{-2}+\boldsymbol{k}_0\right]\boldsymbol{z}-\left[\omega_{-2}+\omega_0\right]\cdot\boldsymbol{t}\right)\right] \\ & + \boldsymbol{E}_{-2}\boldsymbol{E}_{-1} \exp\left[-\boldsymbol{i}\left(\left[\boldsymbol{k}_{-2}+\boldsymbol{k}_{-1}\right]\boldsymbol{z}-\left[\omega_{-2}+\omega_{-1}\right]\cdot\boldsymbol{t}\right)\right] + \boldsymbol{E}_{-2}^2 \exp\left[-\boldsymbol{i}\left(2\boldsymbol{k}_{-2}\boldsymbol{z}-2\omega_{-2}\boldsymbol{t}\right)\right] \\ & + \boldsymbol{E}_{-2}\boldsymbol{E}_1^* \exp\left[-\boldsymbol{i}\left(\left[\boldsymbol{k}_{-2}-\boldsymbol{k}_1\right]\boldsymbol{z}-\left[\omega_{-2}-\omega_1\right]\cdot\boldsymbol{t}\right)\right] + \boldsymbol{E}_{-2}\boldsymbol{E}_0^* \exp\left[-\boldsymbol{i}\left(\left[\boldsymbol{k}_{-2}-\boldsymbol{k}_0\right]\boldsymbol{z}-\left[\omega_{-2}-\omega_0\right]\cdot\boldsymbol{t}\right)\right] \\ & + \boldsymbol{E}_{-2}\boldsymbol{E}_{-1}^* \exp\left[-\boldsymbol{i}\left(\left[\boldsymbol{k}_{-2}-\boldsymbol{k}_{-1}\right]\boldsymbol{z}-\left[\omega_{-2}-\omega_{-1}\right]\cdot\boldsymbol{t}\right)\right] + \left|\boldsymbol{E}_{-2}^2\right| + \boldsymbol{c.c.} \end{aligned}$$

[Eq. 2-12]

While this is a pretty complicated expression, it can be simplified under the assumption that the medium is dispersionless. In that case $\boldsymbol{n}(\omega) = \boldsymbol{n}_0$, and both the frequencies and wavevectors are separated by a constant value: $\omega_i - \omega_{i-1} = \Omega$ and $\boldsymbol{k}_i - \boldsymbol{k}_{i-1} = \kappa$. It can be further simplified by removing all the terms in the complex

conjugate with positive frequencies, and sending all terms with negative frequencies into the complex conjugate. $\widetilde{\boldsymbol{E}}^2(\boldsymbol{z},\boldsymbol{t})$ can then be grouped as follows:

$$
\begin{aligned}
&4\widetilde{\boldsymbol{E}}^2(\boldsymbol{z},\boldsymbol{t}) = \left|\boldsymbol{E}_1^2\right| + \left|\boldsymbol{E}_0^2\right| + \left|\boldsymbol{E}_{-1}^2\right| + \left|\boldsymbol{E}_{-2}^2\right| \\
&+ \boldsymbol{E}_1^2\, exp\left[-\boldsymbol{i}\left(2\boldsymbol{k}_1\boldsymbol{z} - 2\omega_1\boldsymbol{t}\right)\right] + \boldsymbol{E}_0^2\, exp\left[-\boldsymbol{i}\left(2\boldsymbol{k}_0\boldsymbol{z} - 2\omega_0\boldsymbol{t}\right)\right] \\
&+ \boldsymbol{E}_{-1}^2\, exp\left[-\boldsymbol{i}\left(2\boldsymbol{k}_{-1}\boldsymbol{z} - 2\omega_{-1}\boldsymbol{t}\right)\right] + \boldsymbol{E}_{-2}^2\, exp\left[-\boldsymbol{i}\left(2\boldsymbol{k}_{-2}\boldsymbol{z} - 2\omega_{-2}\boldsymbol{t}\right)\right] \\
&\\
&+ 2\boldsymbol{E}_1\boldsymbol{E}_0\, exp\left[-\boldsymbol{i}\left(\left[\boldsymbol{k}_1 + \boldsymbol{k}_0\right]\boldsymbol{z} - \left[\omega_1 + \omega_0\right]\cdot\boldsymbol{t}\right)\right] + 2\boldsymbol{E}_1\boldsymbol{E}_{-1}\, exp\left[-\boldsymbol{i}\left(\left[\boldsymbol{k}_1 + \boldsymbol{k}_{-1}\right]\boldsymbol{z} - \left[\omega_1 + \omega_{-1}\right]\cdot\boldsymbol{t}\right)\right] \\
&+ 2\boldsymbol{E}_1\boldsymbol{E}_{-2}\, exp\left[-\boldsymbol{i}\left(\left[\boldsymbol{k}_1 + \boldsymbol{k}_{-2}\right]\boldsymbol{z} - \left[\omega_1 + \omega_{-2}\right]\cdot\boldsymbol{t}\right)\right] + 2\boldsymbol{E}_0\boldsymbol{E}_{-1}\, exp\left[-\boldsymbol{i}\left(\left[\boldsymbol{k}_0 + \boldsymbol{k}_{-1}\right]\boldsymbol{z} - \left[\omega_0 + \omega_{-1}\right]\cdot\boldsymbol{t}\right)\right] \\
&+ 2\boldsymbol{E}_0\boldsymbol{E}_{-2}\, exp\left[-\boldsymbol{i}\left(\left[\boldsymbol{k}_0 + \boldsymbol{k}_{-2}\right]\boldsymbol{z} - \left[\omega_0 + \omega_{-2}\right]\cdot\boldsymbol{t}\right)\right] + 2\boldsymbol{E}_{-1}\boldsymbol{E}_{-2}\, exp\left[-\boldsymbol{i}\left(\left[\boldsymbol{k}_{-1} + \boldsymbol{k}_{-2}\right]\boldsymbol{z} - \left[\omega_{-1} + \omega_{-2}\right]\cdot\boldsymbol{t}\right)\right] \\
&\\
&+ 2\boldsymbol{E}_1\boldsymbol{E}_{-2}^*\, exp\left[-\boldsymbol{i}\left(3\kappa\boldsymbol{z} - 3\Omega\boldsymbol{t}\right)\right] \\
&+ 2\left(\boldsymbol{E}_1\boldsymbol{E}_{-1}^* + \boldsymbol{E}_0\boldsymbol{E}_{-2}^*\right) exp\left[-\boldsymbol{i}\left(2\kappa\boldsymbol{z} - 2\Omega\boldsymbol{t}\right)\right] \\
&+ 2\left(\boldsymbol{E}_1\boldsymbol{E}_0^* + \boldsymbol{E}_0\boldsymbol{E}_{-1}^* + \boldsymbol{E}_{-1}\boldsymbol{E}_{-2}^*\right) exp\left[-\boldsymbol{i}\left(\kappa\boldsymbol{z} - \Omega\boldsymbol{t}\right)\right] + \boldsymbol{c.c.}
\end{aligned}
$$

[Eq. 2-13]

As $\Omega \approx \omega_V$, the terms that oscillate at this frequency will dominate the equation of motion (last line in [Eq. 2-13]), and so the other non-resonant terms can be dropped. Furthermore, as Ω is much smaller than any optical frequency, these resonant terms will essentially be constant over the time average, and as such we can simply drop the angular brackets. The driving force is then

$$
\begin{aligned}
\widetilde{\boldsymbol{F}}(\boldsymbol{z},\boldsymbol{t}) &= \frac{1}{2}\left(\frac{\partial\alpha}{\partial\boldsymbol{q}}\right)_0 \left\langle \widetilde{\boldsymbol{E}}^2(\boldsymbol{z},\boldsymbol{t}) \right\rangle \\
&= \frac{1}{4}\left(\frac{\partial\alpha}{\partial\boldsymbol{q}}\right)_0 \left(\boldsymbol{E}_1\boldsymbol{E}_0^* + \boldsymbol{E}_0\boldsymbol{E}_{-1}^* + \boldsymbol{E}_{-1}\boldsymbol{E}_{-2}^*\right) exp\left[-\boldsymbol{i}\left(\kappa\boldsymbol{z} - \Omega\boldsymbol{t}\right)\right] + \boldsymbol{c.c.}
\end{aligned}
\qquad \textbf{[Eq. 2-14]}
$$

Given this driving term, assume a solution to [Eq. 2-6] of the form

$$\widetilde{\boldsymbol{q}}(\boldsymbol{z},\boldsymbol{t}) = \boldsymbol{q}(\boldsymbol{z})\cdot exp\left[-\boldsymbol{i}\left(\kappa\boldsymbol{z} - \Omega\boldsymbol{t}\right)\right] + \boldsymbol{q}^*(\boldsymbol{z})\cdot exp\left[\boldsymbol{i}\left(\kappa\boldsymbol{z} - \Omega\boldsymbol{t}\right)\right] \qquad \textbf{[Eq. 2-15]}$$

and insert this into the equation. The result is

$$-\Omega^2\widetilde{\boldsymbol{q}}(\boldsymbol{z},\boldsymbol{t}) + 2\boldsymbol{i}\gamma\Omega\widetilde{\boldsymbol{q}}(\boldsymbol{z},\boldsymbol{t}) + \omega_V^2\widetilde{\boldsymbol{q}}(\boldsymbol{z},\boldsymbol{t}) = \widetilde{\boldsymbol{F}}(\boldsymbol{z},\boldsymbol{t})/\boldsymbol{m} \qquad \textbf{[Eq. 2-16]}$$

and yields a total solution to the molecular motion of the form

$$\widetilde{\boldsymbol{q}}(\boldsymbol{z},\boldsymbol{t}) = \frac{1}{4\boldsymbol{m}}\left(\frac{\partial\alpha}{\partial\boldsymbol{q}}\right)_0 \frac{\left(\boldsymbol{E}_1\boldsymbol{E}_0^* + \boldsymbol{E}_0\boldsymbol{E}_{-1}^* + \boldsymbol{E}_{-1}\boldsymbol{E}_{-2}^*\right)}{\omega_V^2 - \Omega^2 + 2\boldsymbol{i}\gamma\Omega} exp\left[-\boldsymbol{i}\left(\kappa\boldsymbol{z} - \Omega\boldsymbol{t}\right)\right] + \boldsymbol{c.c.} \qquad \textbf{[Eq. 2-17]}$$

2.1.2. Nonlinear Polarization and Resulting Field

With the molecular motion accounted for, the total nonlinear polarization – or the number of molecules N times the single molecule polarization in [Eq. 2-5]:

$$\tilde{P}_{NL}(z,t) = N \cdot \tilde{p}_{NL}(z,t) = N\left(\frac{\partial \alpha}{\partial q}\right)_0 \tilde{q}(z,t)\tilde{E}(z,t) \qquad \textbf{[Eq. 2-18]}$$

is found to be of the form:

$$\begin{aligned}\tilde{P}_{NL}(z,t) = N(\partial\alpha/\partial q)_0 \\ &[q(z)E_1 \cdot exp(-i[(k_1+\kappa)z-(\omega_1+\Omega)t]) \\ &+ q(z)E_0 \cdot exp(-i[(k_0+\kappa)z-(\omega_0+\Omega)t]) \\ &+ q(z)E_{-1} \cdot exp(-i[(k_{-1}+\kappa)z-(\omega_{-1}+\Omega)t]) \\ &+ q^*(z)E_1 \cdot exp(-i[(k_1-\kappa)z-(\omega_1-\Omega)t]) \\ &+ q(z)E_{-2} \cdot exp(-i[(k_{-2}+\kappa)z-(\omega_{-2}+\Omega)t]) \\ &+ q^*(z)E_0 \cdot exp(-i[(k_0-\kappa)z-(\omega_0-\Omega)t]) \\ &+ q^*(z)E_{-1} \cdot exp(-i[(k_{-1}-\kappa)z-(\omega_{-1}-\Omega)t]) \\ &+ q^*(z)E_{-2} \cdot exp(-i[(k_{-2}-\kappa)z-(\omega_{-2}-\Omega)t]) + c.c.]\end{aligned} \qquad \textbf{[Eq. 2-19]}$$

Notice the affect of q and q^* on the frequencies, where they either increase or decrease the frequency by Ω, and the new frequency components generated at $\omega_2 = \omega_1 + \Omega$ and $\omega_{-3} = \omega_{-2} - \Omega$.

To determine the resulting electric field, the optical wave equation

$$\nabla \times \nabla \times \vec{E}(z,t) + \frac{1}{c^2}\frac{\partial^2}{\partial t^2}\vec{E}(z,t) = -\frac{4\pi}{c^2}\frac{\partial^2}{\partial t^2}\vec{P}(z,t) \qquad \textbf{[Eq. 2-20]}$$

must be solved, where

$$\nabla \times \nabla \times \vec{E}(z,t) = \nabla\left(\nabla \cdot \vec{E}(z,t)\right) - \nabla^2 \vec{E}(z,t) \qquad \textbf{[Eq. 2-21]}$$

is often approximated as

$$\nabla \times \nabla \times \vec{E}(z,t) \approx -\nabla^2 \vec{E}(z,t) \qquad \textbf{[Eq. 2-22]}$$

(since there is typically only a very small component of the electric field pointing in the direction of propagation – for the plane waves being considered, $\nabla\left(\nabla \cdot \vec{E}(z,t)\right)$ vanishes identically). This equation reduces to:

$$-\nabla^2 \hat{\boldsymbol{E}}(\boldsymbol{z},\boldsymbol{t}) + \frac{1}{\boldsymbol{c}^2}\frac{\partial^2}{\partial \boldsymbol{t}^2}\hat{\boldsymbol{E}}(\boldsymbol{z},\boldsymbol{t}) = -\frac{4\pi}{\boldsymbol{c}^2}\frac{\partial^2}{\partial \boldsymbol{t}^2}\hat{\boldsymbol{P}}_{\boldsymbol{NL}}(\boldsymbol{z},\boldsymbol{t}) \quad \textbf{[Eq. 2-23]}$$

where again, only the contributions due to the nonlinear polarization are being investigated – the linear polarization affects the field indirectly through the index of refraction. Equating terms that oscillate at a particular frequency, for example at $\omega = \omega_0$:

$$\begin{aligned} &-\frac{\partial^2}{\partial \boldsymbol{z}^2}\left(\boldsymbol{E}_0\, exp\left[-\boldsymbol{i}\left(\boldsymbol{k}_0\boldsymbol{z}-\omega_0\boldsymbol{t}\right)\right]+\boldsymbol{c.c.}\right) \\ &+\frac{\boldsymbol{n}_0^2}{\boldsymbol{c}^2}\frac{\partial^2}{\partial \boldsymbol{t}^2}\left(\boldsymbol{E}_0\, exp\left[-\boldsymbol{i}\left(\boldsymbol{k}_0\boldsymbol{z}-\omega_0\boldsymbol{t}\right)\right]+\boldsymbol{c.c.}\right) \\ &=-\frac{4\pi\boldsymbol{N}}{\boldsymbol{c}^2}\left(\frac{\partial\alpha}{\partial\boldsymbol{q}}\right)_0\frac{\partial^2}{\partial \boldsymbol{t}^2}\left(\left[\boldsymbol{q}(\boldsymbol{z})\boldsymbol{E}_{-1}+\boldsymbol{q}^*(\boldsymbol{z})\boldsymbol{E}_1\right]exp\left[-\boldsymbol{i}\left(\boldsymbol{k}_0\boldsymbol{z}-\omega_0\boldsymbol{t}\right)\right]+\boldsymbol{c.c.}\right) \end{aligned} \quad \textbf{[Eq. 2-24]}$$

which after differentiation becomes:

$$\begin{aligned} &-\frac{\partial^2\boldsymbol{E}_0}{\partial \boldsymbol{z}^2}exp\left(-\boldsymbol{i}\left[\boldsymbol{k}_0\boldsymbol{z}-\omega_0\boldsymbol{t}\right]\right)+2\boldsymbol{i}\boldsymbol{k}_0\frac{\partial\boldsymbol{E}_0}{\partial\boldsymbol{z}}exp\left(-\boldsymbol{i}\left[\boldsymbol{k}_0\boldsymbol{z}-\omega_0\boldsymbol{t}\right]\right)+\boldsymbol{k}_0^2\boldsymbol{E}_0\, exp\left(-\boldsymbol{i}\left[\boldsymbol{k}_0\boldsymbol{z}-\omega_0\boldsymbol{t}\right]\right) \\ &-\frac{\boldsymbol{n}_0^2\omega_0^2}{\boldsymbol{c}^2}\boldsymbol{E}_0\, exp\left(-\boldsymbol{i}\left[\boldsymbol{k}_0\boldsymbol{z}-\omega_0\boldsymbol{t}\right]\right)+\boldsymbol{c.c.} \\ &=\frac{4\pi\boldsymbol{N}\omega_0^2}{\boldsymbol{c}^2}\left(\frac{\partial\alpha}{\partial\boldsymbol{q}}\right)_0\left(\left[\boldsymbol{q}(\boldsymbol{z})\boldsymbol{E}_{-1}+\boldsymbol{q}^*(\boldsymbol{z})\boldsymbol{E}_1\right]exp\left[-\boldsymbol{i}\left(\boldsymbol{k}_0\boldsymbol{z}-\omega_0\boldsymbol{t}\right)\right]+\boldsymbol{c.c.}\right) \end{aligned}$$

[Eq. 2-25]

A typical approximation when solving this equation is the slowly-varying envelope approximation

$$\left|\frac{\partial^2\boldsymbol{E}_0}{\partial\boldsymbol{z}^2}\right| << \left|\boldsymbol{k}_0\frac{\partial\boldsymbol{E}_0}{\partial\boldsymbol{z}}\right| \quad \textbf{[Eq. 2-26]}$$

which says that the envelope is evolving on a length scale much longer than a wavelength. This, along with the fact that $\boldsymbol{k} \equiv \boldsymbol{n}\cdot\omega/\boldsymbol{c}$, allows one to get rid of the first, third, and fourth terms on the left-hand side, leading to the coupled amplitude equation that describes MRG

$$\frac{\partial\boldsymbol{E}_0}{\partial\boldsymbol{z}} = -\frac{2\pi\boldsymbol{i}\omega_0}{\boldsymbol{n}_0\boldsymbol{c}}\left(\boldsymbol{q}(\boldsymbol{z})\boldsymbol{E}_{-1}+\boldsymbol{q}^*(\boldsymbol{z})\boldsymbol{E}_1\right) \quad \textbf{[Eq. 2-27]}$$

2.1.3. Dispersion

Now, to include dispersion into this model the various phase contributions from the wavevector $\boldsymbol{k}$ need to be accounted for. This could have been done from the beginning, but would have complicated the expressions even further. To put these contributions back in,

one can simply multiply each amplitude $\boldsymbol{E}$ and $\boldsymbol{E}^*$ by a factor of $exp(-\boldsymbol{ik})$ and $exp(+\boldsymbol{ik})$ respectively as in [Eq. 2-9], and relax the condition of a dispersionless medium so that $\boldsymbol{k}_n - \boldsymbol{k}_{n-1} \neq \boldsymbol{k}_m - \boldsymbol{k}_{m-1}$ when $\boldsymbol{n} \neq \boldsymbol{m}$ (however, it is still true that $\omega_n - \omega_{n-1} = \Omega$). For example, the equation for the molecular motion [Eq. 2-17] would become

$$\begin{aligned}\tilde{\boldsymbol{q}}(\boldsymbol{z},\boldsymbol{t}) = \frac{1}{4\boldsymbol{m}}\left(\frac{\partial\alpha}{\partial\boldsymbol{q}}\right)_0 \cdot \frac{1}{\omega_V^2 - \Omega^2 + 2\boldsymbol{i}\gamma\Omega} \\ \cdot\left(\boldsymbol{E}_1\boldsymbol{E}_0^* \, exp\left[-\left(\boldsymbol{k}_1 - \boldsymbol{k}_0\right)\boldsymbol{z}\right]\right. \\ + \boldsymbol{E}_0\boldsymbol{E}_{-1}^* \, exp\left[-\left(\boldsymbol{k}_0 - \boldsymbol{k}_{-1}\right)\boldsymbol{z}\right] \\ \left. + \boldsymbol{E}_{-1}\boldsymbol{E}_{-2}^* \, exp\left[-\left(\boldsymbol{k}_{-1} - \boldsymbol{k}_{-2}\right)\boldsymbol{z}\right]\right)\end{aligned} \qquad \textbf{[Eq. 2-28]}$$

and the coupled amplitude equation [Eq. 2-27] would be

$$\begin{aligned}\frac{\partial\boldsymbol{E}_0}{\partial\boldsymbol{z}} exp\left(-\boldsymbol{ik}_0\boldsymbol{z}\right) = -\frac{2\pi\boldsymbol{i}\boldsymbol{N}\omega_0}{\boldsymbol{n}_0\boldsymbol{c}}\left(\frac{\partial\alpha}{\partial\boldsymbol{q}}\right)_0 \\ \cdot\left(\tilde{\boldsymbol{q}}(\boldsymbol{z},\boldsymbol{t})\boldsymbol{E}_{-1} \, exp\left(-\boldsymbol{ik}_{-1}\boldsymbol{z}\right) + \tilde{\boldsymbol{q}}^*(\boldsymbol{z},\boldsymbol{t})\boldsymbol{E}_1 \, exp\left(-\boldsymbol{ik}_1\boldsymbol{z}\right)\right)\end{aligned} \qquad \textbf{[Eq. 2-29]}$$

or

$$\begin{aligned}\frac{\partial\boldsymbol{E}_0}{\partial\boldsymbol{z}} = -\frac{2\pi\boldsymbol{i}\boldsymbol{N}\omega_0}{\boldsymbol{n}_0\boldsymbol{c}}\left(\frac{\partial\alpha}{\partial\boldsymbol{q}}\right)_0 \\ \cdot\left(\tilde{\boldsymbol{q}}(\boldsymbol{z},\boldsymbol{t})\boldsymbol{E}_{-1} \, exp\left(-\boldsymbol{i}\left[\boldsymbol{k}_{-1} - \boldsymbol{k}_0\right]\boldsymbol{z}\right) + \tilde{\boldsymbol{q}}^*(\boldsymbol{z},\boldsymbol{t})\boldsymbol{E}_1 \, exp\left(-\boldsymbol{i}\left[\boldsymbol{k}_1 - \boldsymbol{k}_0\right]\boldsymbol{z}\right)\right)\end{aligned} \qquad \textbf{[Eq. 2-30]}$$

2.1.4. Generalization

The generalization of these equations to an arbitrary number of fields is relatively straightforward. By simply summing over the field components, the equation for the molecular motion and the coupled amplitude equation become:

$$\tilde{\boldsymbol{q}}(\boldsymbol{z},\boldsymbol{t}) = \frac{1}{4\boldsymbol{m}}\left(\frac{\partial\alpha}{\partial\boldsymbol{q}}\right)_0 \cdot \frac{\sum_{\boldsymbol{n}=-\boldsymbol{M}}^{\infty} \boldsymbol{E}_n\boldsymbol{E}_{n-1}^* \, exp\left(-\boldsymbol{i}\Delta_n\boldsymbol{z}\right)}{\omega_V^2 - \Omega^2 + 2\boldsymbol{i}\gamma\Omega} \qquad \textbf{[Eq. 2-31]}$$

$$\frac{\partial\boldsymbol{E}_n}{\partial\boldsymbol{z}} = \frac{-2\pi\boldsymbol{i}\boldsymbol{N}\omega_n}{\boldsymbol{n}(\omega_n)\boldsymbol{c}}\left(\frac{\partial\alpha}{\partial\boldsymbol{q}}\right)_0 \left(\tilde{\boldsymbol{q}}(\boldsymbol{z},\boldsymbol{t})\boldsymbol{E}_{n-1} \, exp\left(\boldsymbol{i}\Delta_n\boldsymbol{z}\right) + \tilde{\boldsymbol{q}}^*(\boldsymbol{z},\boldsymbol{t})\boldsymbol{E}_{n+1} \, exp\left(-\boldsymbol{i}\Delta_{n+1}\boldsymbol{z}\right)\right) \textbf{[Eq. 2-32]}$$

where $\boldsymbol{M} = \left[\frac{\omega_0}{\Omega} - 1 \right]$ rounded up to the nearest integer and $\Delta_n = \boldsymbol{k}_n - \boldsymbol{k}_{n-1}$. This definition of $\boldsymbol{M}$ allows the summation to include all combinations of positive frequencies whose difference equals the separation Ω.

2.2. Characteristics of MRG

These coupled differential equations describing MRG pose an incredible challenge to those looking for a complete analytical solution, especially considering that experiments have demonstrated the generation of over 200 field components [Yavuz 2003]. As a result, most of the published literature trying to describe this effect present a numerical model when discussing particular experimental results, whether in the steady-state [Losev 1993], impulsive [Kalosha 2003], or transient regimes [Sali 2005]. However as in most areas of physics, much physical insight can still be gained by considering various limiting cases of these equations – of particular importance is the demonstration of 1) the Bessel-function character of the Raman orders as they propagate through the system, and 2) an estimate of the total number of orders one would expect with intensities on the same order of magnitude.

2.2.1. Bessel-Function Character of MRG

This discussion is based primarily on the report by Harris & Sokolov (1998), which investigated MRG in the steady-state regime using a two-colour pump at ω_0 and ω_{-1}. While a density matrix formalism involving the Maxwell-Bloch equations are used to describe this process as opposed to the classical argument, the resulting equations (after some simplifications), are formally equivalent. For example, equation #6 in their report:

$$\frac{\partial \tilde{\boldsymbol{E}}_q}{\partial \boldsymbol{z}} = -i\beta_q \left(\tilde{\rho}_{ab} \tilde{\boldsymbol{E}}_{q-1} + \tilde{\rho}^*_{ab} \tilde{\boldsymbol{E}}_{q+1} \right) \qquad \textbf{[Eq. 2-33]}$$

looks like [Eq. 2-32] by collecting the constants from [Eq. 2-32] into a single constant β and by making the substitution $\beta_q = \omega_q \cdot \beta$ in [Eq. 2-33]. One must also assume that $\tilde{\rho}_{ab}$ plays the role of $\tilde{\boldsymbol{q}}(\boldsymbol{z},\boldsymbol{t})$.

The key realization is that the coupled amplitude equation of Eq. 2-3 has a parallel in the Bessel function identity

$$\frac{\partial \boldsymbol{J}_q(\boldsymbol{x})}{\partial \boldsymbol{x}} = \frac{1}{2}\left(\boldsymbol{J}_{q-1}(\boldsymbol{x}) - \boldsymbol{J}_{q+1}(\boldsymbol{x})\right) \qquad \textbf{[Eq. 2-34]}$$

[Spiegel 1999]. Following this, the authors assume a dispersionless medium in the limit of weak excitation, such that only a limited bandwidth is produced and that the molecular excitation $\boldsymbol{q}(\boldsymbol{z},\boldsymbol{t})$ is constant throughout the medium. This leads to the approximations that $\boldsymbol{q}(\boldsymbol{z},\boldsymbol{t})$ can be described by a simple phase $\boldsymbol{q}(\boldsymbol{z},\boldsymbol{t}) \equiv \boldsymbol{q}_0 \propto exp(\boldsymbol{i}\phi_0)$ and all of the generated frequencies $\omega_n \approx \omega_0$, which together reduce [Eq. 2-32] to

$$\frac{\partial \boldsymbol{E}_n}{\partial \boldsymbol{z}} = -\boldsymbol{i}\beta\left(\boldsymbol{q}_0 \boldsymbol{E}_{n-1} + \boldsymbol{q}_0^* \boldsymbol{E}_{n+1}\right) \qquad \textbf{[Eq. 2-35]}$$

where β is a positive and real constant. The authors then assume a solution of the form

$$\begin{aligned}\boldsymbol{E}_n(\boldsymbol{z}) = {} & \boldsymbol{E}_0(0)\,exp\left(\boldsymbol{i}\left[\phi_0 - \pi/2\right]\boldsymbol{n}\right)\boldsymbol{J}_n(\gamma \boldsymbol{z}) \\ & + \boldsymbol{E}_{-1}(0)\,exp\left(\boldsymbol{i}\left[\phi_0 - \pi/2\right]\cdot\left[\boldsymbol{n}+1\right]\right)\boldsymbol{J}_{n+1}(\gamma \boldsymbol{z}) + \boldsymbol{c.c.}\end{aligned} \qquad \textbf{[Eq. 2-36]}$$

where γ is a phenomenological constant taken to be real and positive. To motivate this choice of solution, a few issues concerning the initial condition $2\tilde{\boldsymbol{E}}(0,\boldsymbol{t}) = \boldsymbol{E}_0(0)\,exp\left(\boldsymbol{i}\omega_0 \boldsymbol{t}\right) + \boldsymbol{E}_{-1}(0)\,exp(\boldsymbol{i}\omega_{-1}\boldsymbol{t}) + \boldsymbol{c.c.}$ need to be considered:

1. The flow of radiation should depend on the initial values of both pumps
2. Of the ordinary Bessel functions $\boldsymbol{J}_n(\boldsymbol{x})$, only $\boldsymbol{J}_0(\boldsymbol{x})$ has an initial value that is non-zero, and so each pump field $\boldsymbol{E}_0(\boldsymbol{z},\boldsymbol{t})$ and $\boldsymbol{E}_{-1}(\boldsymbol{z},\boldsymbol{t})$ must be multiplied by the appropriate Bessel function.
3. The initial values of the pumps do not depend on the phase of the molecular motion ϕ_0, however any radiation scattered from other fields should depend on this factor, as the light must scatter from $\tilde{\boldsymbol{q}}(\boldsymbol{z},\boldsymbol{t})$.

While these considerations do not require the inclusion of $-\pi/2$ in the phase terms, this will become important later in the derivation. Substituting [Eq. 2-36] into [Eq. 2-35]:

$$\begin{aligned}\frac{\partial \boldsymbol{E}_n(\boldsymbol{z})}{\partial \boldsymbol{z}} = {} & \gamma \boldsymbol{E}_0(0)\,exp\left(\boldsymbol{i}\left[\phi_0 - \pi/2\right]\boldsymbol{n}\right)\frac{\left(\boldsymbol{J}_{n-1}(\gamma \boldsymbol{z}) - \boldsymbol{J}_{n+1}(\gamma \boldsymbol{z})\right)}{2} \\ & + \gamma \boldsymbol{E}_{-1}(0)\,exp\left(\boldsymbol{i}\left[\phi_0 - \pi/2\right]\cdot\left[\boldsymbol{n}+1\right]\right)\frac{\left(\boldsymbol{J}_n(\gamma \boldsymbol{z}) - \boldsymbol{J}_{n+2}(\gamma \boldsymbol{z})\right)}{2} \\ & + \boldsymbol{c.c.}\end{aligned} \qquad \textbf{[Eq. 2-37]}$$

which can be rearranged to form

$$\begin{aligned}\frac{\partial \boldsymbol{E}_n(\boldsymbol{z})}{\partial \boldsymbol{z}} = \frac{\gamma}{2}\Big[&\boldsymbol{E}_0(0)\exp\big(\boldsymbol{i}[\phi_0 - \pi/2]\boldsymbol{n}\big)\boldsymbol{J}_{n-1}(\gamma \boldsymbol{z}) \\ &+ \boldsymbol{E}_{-1}(0)\exp\big(\boldsymbol{i}[\phi_0 - \pi/2]\cdot[\boldsymbol{n}+1]\big)\boldsymbol{J}_n(\gamma \boldsymbol{z})\Big] \\ -\frac{\gamma}{2}\Big[&\boldsymbol{E}_0(0)\exp\big(\boldsymbol{i}[\phi_0 - \pi/2]\boldsymbol{n}\big)\boldsymbol{J}_{n+1}(\gamma \boldsymbol{z}) \\ &+ \boldsymbol{E}_{-1}(0)\exp\big(\boldsymbol{i}[\phi_0 - \pi/2]\cdot[\boldsymbol{n}+1]\big)\boldsymbol{J}_{n+2}(\gamma \boldsymbol{z})\Big] \\ &+ \boldsymbol{c.c.}\end{aligned} \qquad \textbf{[Eq. 2-38]}$$

Note the mismatch between the index of the Bessel functions and the index of the exponentials. This can be adjusted by pulling out an appropriate phase from the exponentials:

$$\begin{aligned}\frac{\partial \boldsymbol{E}_n(\boldsymbol{z})}{\partial \boldsymbol{z}} = \frac{\gamma}{2}\exp(\boldsymbol{i}\phi_0)\exp(-\boldsymbol{i}\pi/2)\Big[&\boldsymbol{E}_0(0)\exp\big(\boldsymbol{i}[\phi_0 - \pi/2]\cdot[\boldsymbol{n}-1]\big)\boldsymbol{J}_{n-1}(\gamma \boldsymbol{z}) \\ &+ \boldsymbol{E}_{-1}(0)\exp\big(\boldsymbol{i}[\phi_0 - \pi/2]\cdot \boldsymbol{n}\big)\boldsymbol{J}_n(\gamma \boldsymbol{z})\Big] \\ -\frac{\gamma}{2}\exp(-\boldsymbol{i}\phi_0)\exp(\boldsymbol{i}\pi/2)\Big[&\boldsymbol{E}_0(0)\exp\big(\boldsymbol{i}[\phi_0 - \pi/2]\cdot[\boldsymbol{n}+1]\big)\boldsymbol{J}_{n+1}(\gamma \boldsymbol{z}) \\ &+ \boldsymbol{E}_{-1}(0)\exp\big(\boldsymbol{i}[\phi_0 - \pi/2]\cdot \boldsymbol{n}\big)\boldsymbol{J}_{n+2}(\gamma \boldsymbol{z})\Big] \\ &+ \boldsymbol{c.c.}\end{aligned} \qquad \textbf{[Eq. 2-39]}$$

After comparing this to [Eq. 2-36], one can rewrite this as

$$\begin{aligned}\frac{\partial \boldsymbol{E}_n(\boldsymbol{z})}{\partial \boldsymbol{z}} &= -\frac{\boldsymbol{i}\gamma}{2}\exp(\boldsymbol{i}\phi_0)\boldsymbol{E}_{n-1}(\boldsymbol{z}) - \frac{\boldsymbol{i}\gamma}{2}\exp(-\boldsymbol{i}\phi_0)\boldsymbol{E}_{n+1}(\boldsymbol{z}) \\ &= -\boldsymbol{i}\beta\big(\boldsymbol{q}_0\boldsymbol{E}_{n-1}(\boldsymbol{z}) + \boldsymbol{q}_0^*\boldsymbol{E}_{n+1}(\boldsymbol{z})\big)\end{aligned} \qquad \textbf{[Eq. 2-40]}$$

where $\gamma = 2\beta$. Thus, in the limit of weak excitation, the equations for individual field components is a sum of two Bessel functions as shown in [Eq. 2-36].

2.2.2. Components of comparable intensity

To make short pulses one needs a large bandwidth, and so the question of how many orders can be produced (and therefore bandwidth), is natural to consider. A simple expression can be found using the approximations described in **§2.2.1**, however Losev & Lutsenko (1993) address this question with relatively few approximations, and as such can discuss the behaviour of MRG even beyond the limit of weak excitation.

To compare directly to the formalism of Losev & Lutsenko (1993), assume again that the pump is a two-colour beam at ω_0 and ω_{-1}, but that it is exactly on resonance so that $\omega_0 - \omega_{-1} = \Omega = \omega_V$. Adjust the phase of molecular motion so that $\boldsymbol{Q} \equiv \boldsymbol{i}\cdot\tilde{\boldsymbol{q}}(\boldsymbol{z},\boldsymbol{t})$,

normalize the field amplitudes $E_n(z)$ such that $A_n \equiv \frac{E_n(z)}{E_0(0)}$, and define the irradiance (hereafter to be referred to as the intensity), as $I_n(z) \equiv E_n(z)E_n^*(z)$. With these definitions, equations [Eq. 2-31] and [Eq. 2-32] become equations (1) and (2) in the manuscript:

$$Q = \alpha I_0(0) \sum_{n=-M}^{\infty} A_n A_{n-1}^* \exp(-i\Delta_n z) \qquad \textbf{[Eq. 2-41]}$$

$$\frac{\partial A_n}{\partial z} = \beta \frac{\omega_n}{\omega_0}\left(Q^* A_{n+1} \exp[-i\Delta_{n+1} z] - Q A_{n-1} \exp[i\Delta_n z]\right) \qquad \textbf{[Eq. 2-42]}$$

where the real and positive coefficients $\alpha \equiv \frac{1}{4m\gamma\omega_V}\left(\frac{\partial \alpha}{\partial q}\right)_0$ and $\beta \equiv \frac{\pi N \omega_0}{n(\omega_n)c}\left(\frac{\partial \alpha}{\partial q}\right)_0$.

With this revised notation, consider again the case of weak excitation, where it was found that the field could be described using Bessel functions, but this time in the context of [Eq. 2-41] and [Eq. 2-42]. One property of ordinary Bessel functions $J_n(x)$ is that the number of orders **n** with approximately the same amplitude is given by twice the argument x. As this gives a direct measure of the number of fields generated in MRG, the argument of these functions should in turn provide an estimate of the generated bandwidth, where $\Delta\omega \approx (\#\ of\ Fields - 1)\cdot\omega_V$. In the discussion of **§2.2.1**, the arguments of the Bessel functions included the factor γ, which itself was twice the value of the constant in the coupled amplitude equation. Pulling the real constants from Q into $\partial A_n/\partial z$, one can obtain the slightly modified coupled amplitude equation

$$\frac{\partial A_n}{\partial z} = \alpha\beta I_0(0)\frac{\omega_n}{\omega_0}\left(Q^* A_{n+1} \exp[-i\Delta_{n+1} z] - Q A_{n-1} \exp[i\Delta_n z]\right) \textbf{[Eq. 2-43]}$$

Within the assumptions of weak excitation and a dispersionless medium, the argument of the Bessel functions is then

$$\gamma z = \frac{\pi}{2c}\frac{N}{n_0 m\gamma}\frac{\omega_0}{\omega_V}\left(\frac{\partial \alpha}{\partial q}\right)_0^2 \cdot I_0(0)\cdot z \qquad \textbf{[Eq. 2-44]}$$

implying that the bandwidth (which is $\approx 2\gamma z\omega_V$), should increase linearly with distance, pressure (N), intensity, pump frequency, and the dephasing time of the molecular vibrations ($1/\gamma$). Notice however that the bandwidth should *not* scale with the vibrational

frequency ω_V, implying that it should be roughly the same between molecular species, provided other molecular parameters are similar.

Relaxing the conditions that $\omega_n = \omega_0$ and $\partial q(z)/\partial z = 0$, a general formula for the number of components generated can be derived. As presented in Losev & Lutsenko (1993), it can be shown with the approximation of zero dispersion that the parametric growth rate $\xi \equiv \beta \int_0^z \boldsymbol{Q} \cdot \boldsymbol{dx}$, which defines the strength of the MRG interaction, is approximately equal to both the number of Stokes and anti-Stokes orders generated. As well, with the assumption that the amplitudes $\boldsymbol{A_n}$ fall off rapidly with increasing $|\boldsymbol{n}|$ such that $\boldsymbol{A_n}|\boldsymbol{n}|^{-1/2} \to 0$ as $\boldsymbol{n} \to -\boldsymbol{M}$ *or* ∞, ξ can be determined by considering the normalized intensity $\boldsymbol{J} = \sum_{-M-1}^{\infty} \boldsymbol{A_n A_n^*}$ and the normalized polarizability amplitude $\boldsymbol{S} = \sum_{-M}^{\infty} \boldsymbol{A_n A_{n-1}^*}$. Through the significant manipulations described in Losev & Lutsenko (1993) these lead to an expression for the parametric growth rate

$$\xi(\mathbf{B}) = \frac{\omega_0}{\omega_V} ln \left| \frac{tanh\left(\frac{\mathbf{J}(\infty)\mathbf{B}\omega_V/\omega_0 + arctanh(\mathbf{J}(\infty))}{2} \right)}{tanh\left(\frac{arctanh(\mathbf{J}(\infty))}{2} \right)} \right| \quad \textbf{[Eq. 2-45]}$$

where the limiting value of the intensity $\mathbf{J}(\infty)$ tends toward

$$\mathbf{J}(\infty) = \sqrt{1 - [\mathbf{S}(0)/\mathbf{J}(0)]^2} \quad \textbf{[Eq. 2-46]}$$

This growth rate ξ is given as a function of the Raman Parameter $\boldsymbol{B}$ which, similar to the γz parameter in [Eq. 2-44], is related to the propagation distance, pressure, the initial intensity, and the ratio between the pump frequency and the vibrational frequency

$$\boldsymbol{B} = \frac{\pi}{2c} \frac{N}{n_0 m \gamma} \frac{\omega_0}{\omega_V} \left(\frac{\partial \alpha}{\partial q} \right)_0^2 (I_0(0) + I_{-1}(0)) z \quad \textbf{[Eq. 2-47]}$$

Note that again, the total bandwidth which is now given by $\Delta\omega \approx 2\xi\omega_V$ is invariant with respect to the Raman frequency ω_V, as the parameter $\boldsymbol{B}$ is multiplied by ω_V/ω_0 in [Eq. 2-45].

As shown in Figure 2-2, this expression for ξ will be approximately linear at low values of $\boldsymbol{B}$, but as the pressure, pump intensity, or propagation distance starts to become

large the process begins to saturate (see Figure 2-2). In the limiting case, the parametric growth rate tends to the value

$$\xi(\infty) = (\omega_0/\omega_V) ln\left| coth\left[\frac{arctanh(\mathbf{J}(\infty))}{2}\right]\right| \qquad \textbf{[Eq. 2-48]}$$

Note that this expression is *only* dependent on the initial relative strength of the two pumps (in the expression for $\mathbf{J}(\infty)$). This implies that the total possible bandwidth is only dependent on the pump frequency and the relative strengths of the pump and Stokes beams – all other factors such as the intensity, pressure, the properties of the molecule and the propagation distance simply affect the rate at which one obtains this bandwidth.

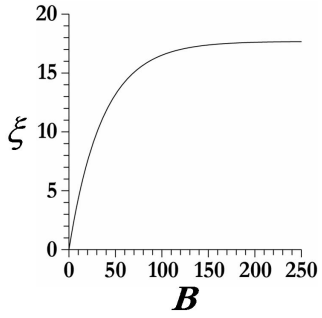

Figure 2-2: Plot of the parametric growth rate as a function of the Raman parameter B. Note the initial linear behaviour and the subsequent saturation.

2.3. Computational model

To help describe the observations of the experiment, a computational model describing MRG was developed in Matlab. While the accuracy of the model is simply limited by the level of complexity one chooses to include, for practical purposes the first attempt only included the classical on-resonance description of Losev & Lutsenko (1993), which neglects diffraction, population of the vibrational level, and the effects of other $\chi^{(3)}$ processes such as self-phase modulation.

As both the Raman generation and dispersion can be described in the frequency domain within the classical formalism, the electric field is treated as a single array in ω, even when working in the transient regime where the pulses are short and the bandwidths large. While this differs from the typical carrier-envelope treatment typical of models starting from the Maxwell-Bloch equations, where each order is given a temporal envelope for a particular carrier frequency $\omega_n = \omega_0 + n\omega_V$ and the Raman generation is described in the temporal domain [Sali 2005], it is in many ways similar to the recently developed single-field Maxwell-

Bloch model where a single array in $\boldsymbol{t}$ is used to describe the electric field [Kinsler 2005]. As the classical description only requires one to work in the frequency domain, a single-field description in frequency was chosen for this model as opposed to an adaptation of the carrier-envelope technique.

To verify the validity of the computational model, the results for plane-wave excitation in the zero dispersion limit were compared to those that are published [Losev 1993]. Using the same parameters as reported in the manuscript, the result of the comparison is demonstrated in Figure 2-3. Although the agreement is generally good, there is a discrepancy in the values of some of the troughs. It is believed that the spatial resolution in z is limiting the agreement, however within the resources of the PC that was used this could not be enhanced further. They are close enough however that it was expected the essence of MRG had been captured in the program, and that while it may not give an exact solution, a qualitative discussion should be feasible.

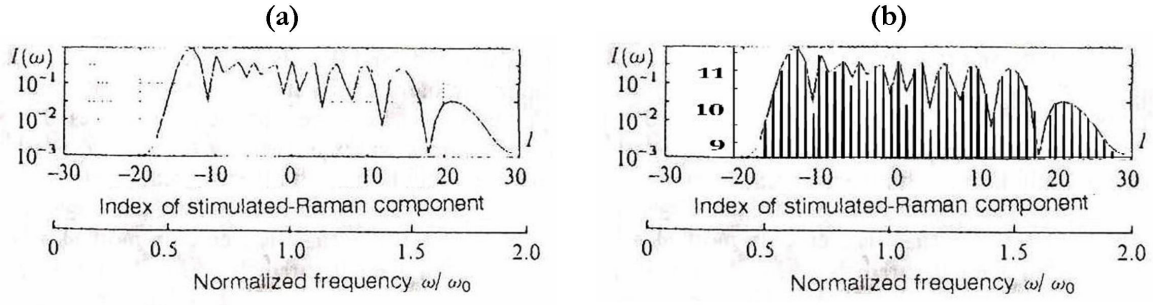

Figure 2-3: Comparison of the program to published results. (a) Figure 4b in Losev & Lutsenko (1993). (b) Superposition of the simulation with the spectrum in (a)

For clarity, the simulation is presented again in Figure 2-4a. Note the generation of a bandwidth that, within an order of magnitude of the peak, contains ~31 Raman orders. This corresponds well to the predicted analytical value of $2\xi = 35$. Qualitatively there are two important features of this spectrum aside from the generated bandwidth – the first is the large number of anti-Stokes orders generated compared to the Stokes, which may be a result of the frequency dependence of the coupled amplitude equation (for the parameters chosen the Raman order at an index of -20 is at a frequency of 215THz, whereas the Raman order at an index of +30 is four times as large at 1095THz). The second feature of interest is that while there are more anti-Stokes orders generated, the Stokes orders are generally more intense. These higher intensities is a consequence of the parametric nature of MRG – to

generate an anti-Stokes photon, one must also generate a Stokes photon, which implies that the flow of energy from the two pumps to higher frequencies must be matched by a flow of energy to lower frequencies. This should not to be confused with a statement of the form "each order of anti-Stokes must be matched by a corresponding Stokes order", which is not true – Figure 1-1a demonstrates how a second-order anti-Stokes photon can be generated by converting pump photons into only first-order Stokes photons. In that case, one pump photon absorbed an energy $2\eta\omega_v$ by forcing two pump photons to lose an energy of $\eta\omega_v$, thereby conserving energy.

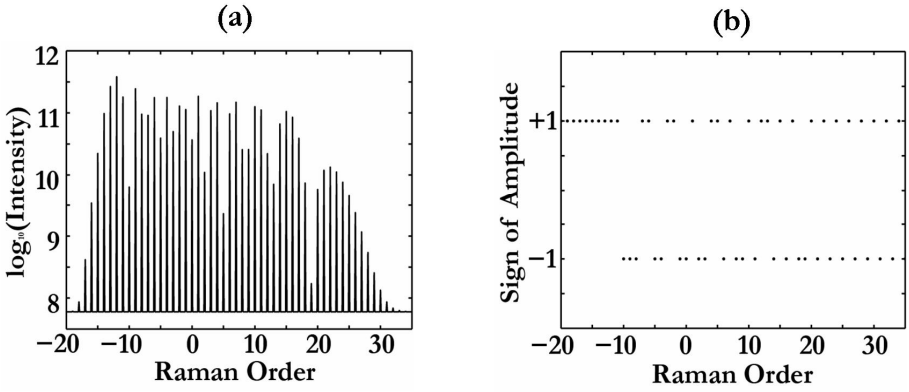

Figure 2-4: Resulting spectrum from on-resonance excitation with zero dispersion. (a) Intensity spectrum of Raman orders. (b) The sign of the amplitude for each order: note the regular phase jumps of π

Another insight that can be gained from the simulation is the fact that the dispersionless MRG spectrum does not spontaneously produce short pulses. This is illustrated in Figure 2-5, where a numeric fast Fourier transform of the spectrum was used to produce a temporal profile in parts (a) and (b), however in part (a) the phase was left unchanged and in (b) it was assumed that the phases were perfectly compensated, and so of the same sign across the entire spectrum. The broad temporal profile observed in Figure 2-5a is therefore a result of the regular phase jumps of π apparent in Figure 2-4b, where the amplitudes of the Raman orders flip back and forth from positive to negative across the spectrum. Both the spectrum and the signs determined in this model are consistent with the model of Kalosha & Herrmann (2000), with slight deviations similar to those found when comparing the results to Losev & Lutsenko (1993) in Figure 2-3.

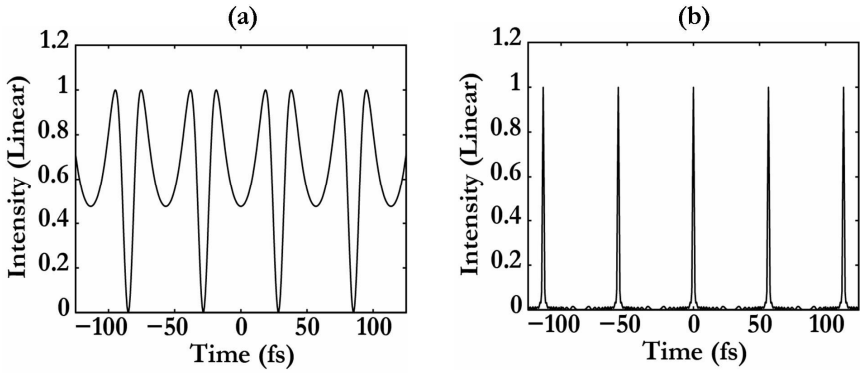

Figure 2-5: Fast Fourier transform of the spectrum in Figure 2-4a. (a) The phase of the spectrum includes the jumps of π as in Figure 2-4b. (b) The phase is assumed to be flat across the spectrum.

3. Experimental Apparatus

The optical setup in general follows the block diagram of Figure 3-1. In brief, a broad-bandwidth pulse is generated in the laboratory of Dr. Joseph Sanderson, where it is stretched to ~1ns and delivered via single mode fibre to the laboratory of Dr. Donna Strickland. This pulse is amplified using a dual-wavelength regenerative amplifier [Zhang 2000], and then further amplified using a dual-wavelength multipass amplifier [Xia 2002]. The pulses are then compressed and focussed into a hollow dielectric waveguide filled with SF_6 gas. The resulting MRG spectrum is then sent to two spectrometers simultaneously to record the ultra-broad bandwidth.

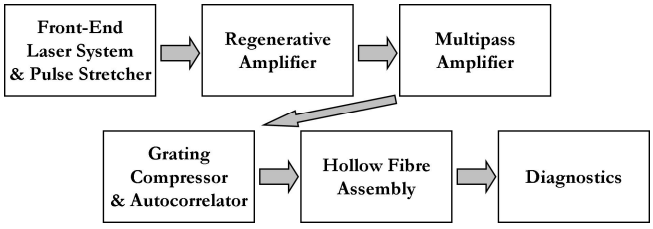

Figure 3-1: Block Diagram of the Experimental Apparatus

Sulphur hexafluoride was chosen as the Raman-active medium due to a number of qualities that made it particularly suitable for study with this system. Primarily, its Raman-active 23THz A_{1g} vibrational mode [Herzberg 1945], was well within the range of the two-colour amplifiers, which in the past have been used to generate colours as far apart as ~40THz [Xia 2003]. A secondary benefit of this small vibrational frequency (small compared to simple diatomic molecules), is that it should result in a relatively large pulse spacing of about 43fs according to Fourier theory. With pump envelopes of a few hundred femtoseconds, the bulk of the energy should be contained in only a few ultrashort pulses after compression. The second main advantage of SF_6 is its vibrational dephasing time of 6.6ps [Everall 1987]. The gain in transient MRG has been found to depend on the ratio of the pulse duration to the dephasing time [McDonald 1994], and as such we should be able to get efficient generation with pulse durations of a few hundred femtoseconds, as compared to molecules such as H_2 with a dephasing time of 1ns or CH_4 with a dephasing time of 30ps. Finally, the MRG spectrum generated with SF_6 will not be complicated by the rotational orders often observed with diatomic molecules [Johnson 1967; Imasaka 1989], as its spherical symmetry precludes any rotational excitation.

3.1. Front-End Laser System & Pulse Stretcher

The overall experimental setup is based on Chirped-Pulse Amplification (CPA), a technique developed by Strickland & Mourou (1985). In CPA, a short pulse first needs to be stretched before it can be amplified and used for an experiment. To accomplish this stretching, our pulse is sent through a medium that exhibits normal positive dispersion, where the index of refraction – a measure of the velocity of light as it propagates through the medium – increases nonlinearly with increasing frequency (see Figure 3-2). As a higher index of refraction corresponds to a slower light velocity, red wavelengths will pull ahead of the blue and stretch the pulse.

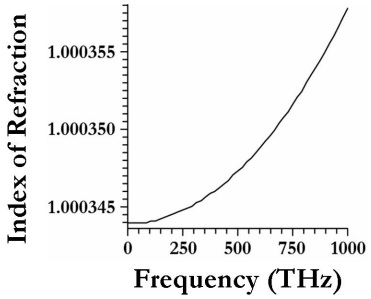

Figure 3-2: Index of refraction curve for SF_6, as determined using the equations and constants from Kalosha & Herrmann (2003)

The stretching of short pulses in a medium can also be described via a frequency-dependent phase delay added to the pulses. The origin of this phase delay comes from the term $e^{-i(kz-\omega t)}$ in the equation for the electric field, where the wavevector $k = n\omega/c$ is a nonlinear function of the frequency due to the index of refraction. Using the Sellmeyer equation, the index of refraction is found to be [Kalosha 2003]

$$n^2(\omega) = 1 + \sum_i \frac{C_i}{\omega_i^2 - \omega^2} \qquad \textbf{[Eq. 3-1]}$$

where the sum over i is a sum over the resonances in the material. A Taylor expansion about a particular frequency ω_0 results in the form

$$n(\omega) \approx n_0 + \left(\frac{dn}{d\omega}\right)_{\omega_0} \cdot (\omega - \omega_0) + \left(\frac{d^2 n}{d\omega^2}\right)_{\omega_0} \frac{(\omega - \omega_0)^2}{2} + \left(\frac{d^3 n}{d\omega^3}\right)_{\omega_0} \frac{(\omega - \omega_0)^3}{2} + \ldots \qquad \textbf{[Eq.3-2]}$$

where the different orders affect the propagation of the pulse in various ways. Following the description in Chapter 9 of Siegman (1986), one can determine the effect of these terms as demonstrated in Figure 3-3. In Figure 3-3a, a phase delay due to the constant index of refraction simply shifts the oscillations of the electric field underneath the envelope. Figure

3-3b demonstrates the effect of a linearly increasing index of refraction, which is often termed group delay as it is the entire envelope that is shifted instead of just the phase. Figure 3-3c shows a stretching of the pulse due to the second-order dispersion, which describes the dispersion of the group delay, or equivalently how the group velocity changes with respect to wavelength. The asymmetric pulse-splitting due to third-order dispersion is shown in Figure 3-3d. Ideally, the normal positive dispersion experienced by the pulse in the stretcher should be exactly matched by the negative dispersion in the compressor, which will be discussed again in **§3.4**.

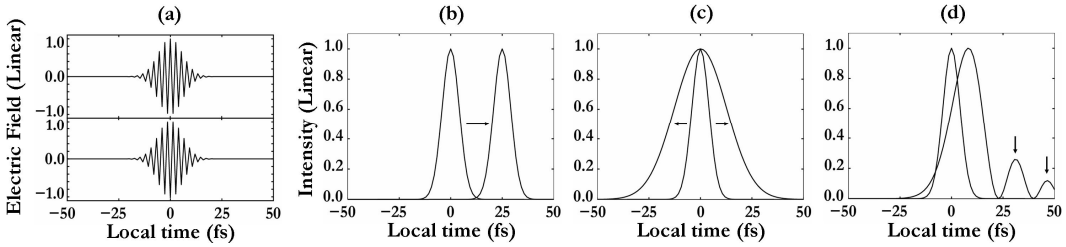

Figure 3-3: Effect of various orders of the dispersion on a short pulse: (a) a constant phase shift simply adjusts the phase of the oscillation – depicted is a phase shift of π; (b) first-order dispersion results in a delay of the pulse in time; (c) second-order dispersion stretches the pulse; (d) third-order dispersion stretches and splits the pulse

The mode-locked oscillator used to provide the short pulses is a commercial Femtolasers Scientific Pro that generates 10fs pulses with a central wavelength of 800nm. These are produced at a rate of ~75MHz and an average power of 400mW. A quarter of this power is split off and then, to prevent self-phase modulation later in the system, is stretched by propagation through a 5cm glass block and a 5cm water cell, where the two media are used simply because of their availability in the lab. No phase distortions from self-phase modulation occur during this stretching, as the pulses only contain ~1nJ of energy and have a beam diameter of ~2mm FWHM. These pulses are then focussed into a ~100m polarization-maintaining (PM) fibre, which provides the dual purpose of further stretching the pulses using the normal positive dispersion of the fibre (to ~1ns), and transporting the pulses to Dr. Strickland's laboratory, where they are used to seed a two-colour regenerative amplifier. A polarization-maintaining fibre was used as opposed to a simple single-mode fibre as a frequency-dependent polarization rotation was observed in the original single-mode fibre stretcher. This frequency-dependent polarization would generate holes in the spectrum after sending the seed through a polarizing Faraday Isolator, hence making it difficult to seed the two wavelengths in the regenerative amplifier well. While this problem

was not observed with the PM fibre, it was found by using a waveplate and polarizer that it did not actually maintain the initial linear polarization, but instead randomized it across the entire spectrum. This was certainly not expected, but is still preferable to the frequency-dependent behaviour exhibited by the single mode fibre, and did allow for sufficient seeding of the regenerative amplifier. An example of the spectrum obtained from the oscillator is given in Figure 3-4.

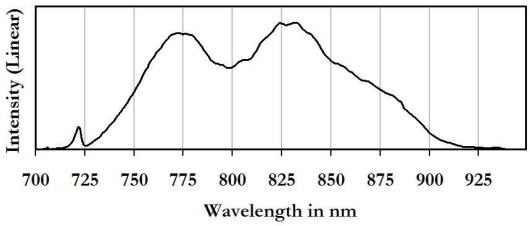

Figure 3-4: Measured spectrum of the Femtolasers Scientific Pro oscillator

3.2. Dual-Wavelength Regenerative Amplifier

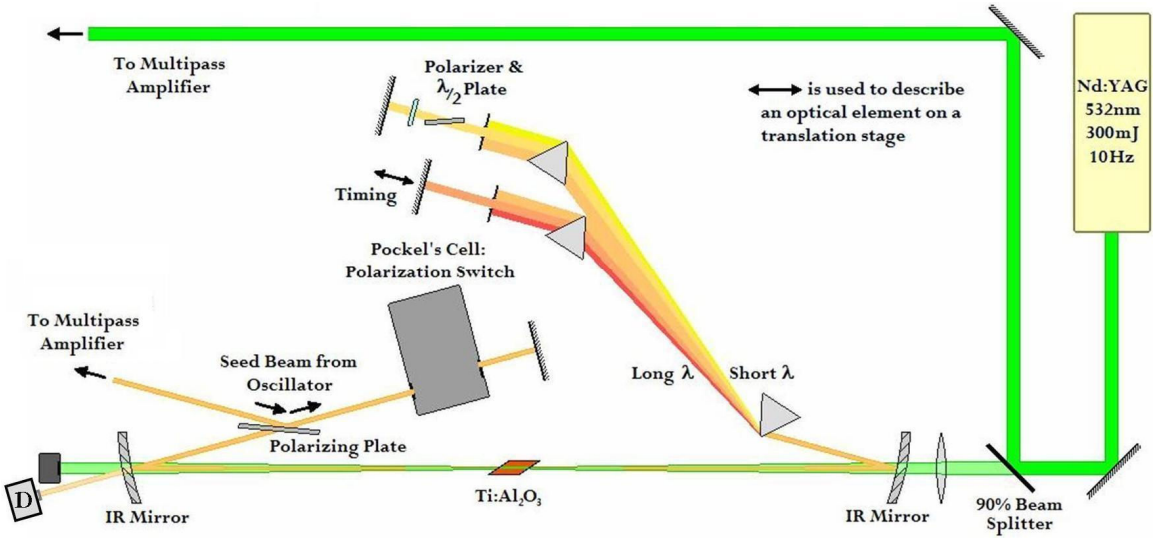

Figure 3-5: Illustration of the dual-wavelength regenerative amplifier

The main advantage of this laser system for the study of transient MRG is the ability to provide two high-energy broadband pulses shifted from each other in frequency. Key to the dual-wavelength operation of this system is the lab-built regenerative amplifier (Regen) reported in Zhang et al (2000), where it is seeded by the ultra-broad bandwidth of the oscillator pulses as opposed to the original lab-built two-colour oscillator. As the maintenance and operation of this system was critical to this study, its design and alignment are presented in appendices A and B respectively.

In brief, a single ultra-broad bandwidth pulse from the oscillator is injected into a four-mirror cavity using a combination of a polarizer and a polarization-switching element called a Pockels Cell. It is then focussed into a Titanium-doped Sapphire crystal (Ti:Sapphire), which is optically excited using a frequency-doubled Spectra-Physics Nd:YAG laser (Neodymium-doped Yttrium-Aluminium-Garnet laser). A system of prisms act to disperse the infrared pulse in the cavity, splitting it into two pulses of separate frequencies defined by slits in the cavity. Once the pulses have attained their maximum energy, as determined by a diode collecting the light leaked through one of the mirrors, they are ejected again via the polarizer/Pockels Cell combination.

3.2.1. Seeding of the Amplifier

A schematic of the seeding apparatus is shown in Figure 3-6. After entering the laboratory through the PM fibre, the oscillator pulses are sent through a Faraday Isolator (FI) to prevent damage to the fibre optic by the returning beams. That is, any light that is sent back along the path of the seed will be redirected. This is accomplished by using a pair of polarizers in conjunction with a Faraday rotator, an element that applies a magnetically-induced direction-dependent rotation to the polarization of the beam via the Faraday effect [Hecht 2002]. This element also includes a half-wave plate to optimize its isolating action for a particular wavelength, which is tuneable in the two-colour regenerative amplifier.

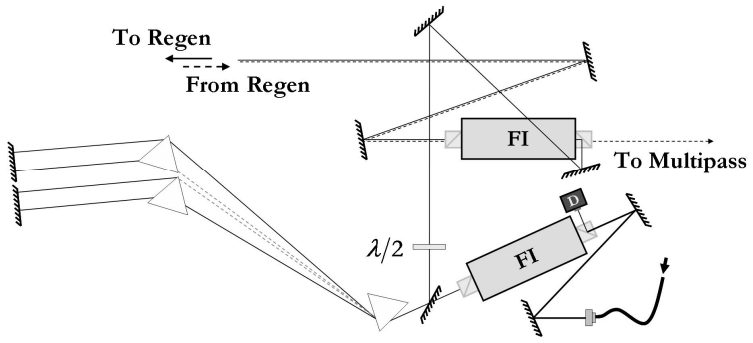

Figure 3-6: Two-colour seeding of the Regen

As mentioned earlier, the polarization of the seed beam is randomized by the PM fibre, and as such it is split by the first polarizer of the Faraday Isolator. The rejected polarization is sent to a fast diode (D) to act as a clock signal for the Pockels Cell and detection instruments. The transmitted seed is spectrally separated using a system of three prisms, as there is then independent control of the seeding for the two wavelengths in the Regen. By aiming the back mirrors slightly downwards to a lowered mirror, the pulses are

recombined and sent through a broadband half-wave plate ($\lambda/2$) before going through a second Faraday Isolator. Two Faraday Isolators are used because it was observed that a single FI could not fully prevent the two pulses generated in the Regen from damaging the fibre optic, given their large separation in frequency. Note that the convoluted path of the beam before the second Faraday Isolator is designed to allow the returning pulses from the Regen to go straight through, reducing the potential for spatial chirp and misalignment of the beams. A significant divergence between the two amplified pulses was observed when the Faraday Isolator was used in the opposite manner (sending the seed straight through and making the Regen pulses reflect at an angle), as the reflection through the polarizer is not actually at a 90^{o} angle, making it act as a wedge. This wedge-like behaviour was also the reason the independent control of the two seed pulses was required and installed once the Faraday Isolator was turned around.

To control how the seed pulses enter and exit the cavity, a combination of a polarizer and a polarization switch is used in the cavity. The polarization switch is a commercial Medox Pockels Cell, which uses a voltage-dependent birefringence called the Pockels effect to adjust the polarization of the beam as it passes through. During regular operation, the birefringence is set to make the cell act as a quarter-wave plate with the voltage off, and with the two consecutive pulses of different voltages, it is set to act first as a half-wave plate, and then as a three-quarters-wave plate. Its operation is as follows:

1. An initially s-polarized seed pulse (polarized perpendicular to the optical bench), reflects off the polarizer
2. With the voltage off, the seed becomes circularly polarized light as it first goes through the Pockels Cell. It is immediately reflected by a plane mirror back through cell again, changing it to p-polarized light (parallel to the optical bench)
3. Before the next seed pulse can enter the cavity, a voltage pulse is sent to the Pockels Cell to convert it to a half-wave plate. Therefore, any subsequent seed pulses will simply be reflected out of the cavity by the polarizer, as they will be rotated and then counter-rotated upon traversing the cell, returning to s-polarization
4. The trapped p-polarized seed pulse oscillates back and forth in the cavity, as the Pockels Cell again only rotates and counter-rotates the polarization.
5. After the seed pulse has been amplified, the second voltage pulse puts the Pockels Cell into its three-quarter-wave mode, ejecting the seed from the cavity as it

becomes s-polarized again. The Pockels Cell is then electrically grounded in preparation for the next pump pulse.

3.2.2. Amplification

The amplifier itself is essentially a two-colour laser, and can generate its own pulses through the amplification of its own spontaneous emission. To differentiate this light from that of the amplified seed pulse, the amplified spontaneous emission of the Regen is referred to simply as the ASE as opposed to the amplified seed pulse. This ASE will have the same frequency spectrum as the seed would have during amplification in the Regen, however it lacks the definite phase relationship that is characteristic of a mode-locked pulse, and is therefore not compressible. Any ASE that is generated along with the seed pulse will therefore act as a background and compete for the gain in the amplifier, and as such it is desirable to align the seed beam into the Regen as well as possible to maximize its gain and minimize the ASE. In particular, there must be more seed light coupled properly into the cavity than there would be ASE at the time of the seed injection. To aid in this effort, the seed is spectrally separated prior to the Regen assembly allowing for total and independent control of the two colours. A fast diode is also placed behind a mirror in the Regen to monitor the small amount of light that leaks through, allowing one to observe the radiation in the cavity as a function of time to aid in the alignment (see the element labelled **D** in Figure 3-5). A characteristic trace from this diode is illustrated in Figure 3-7, where the sharp peaks are due to the seed pulse and the broad background is from the ASE. The time between the peaks corresponds to the round-trip time of the pulse in the cavity. By monitoring the ratio of the seed signal to that of the ASE, one can optimize the seed alignment. The point at which the seed is injected with the same power as the existing ASE is when $\mathbf{V_{Seed}/V_{ASE}}$ is 2:1, such that the seed peaks sitting on the background are as intense as the background itself. A typical value for this ratio obtained in our experiments is 40:1.

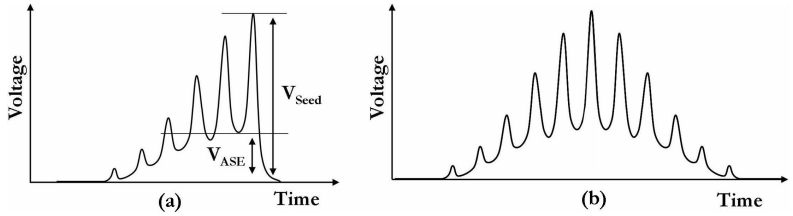

Figure 3-7: Characteristic trace of the fast diode from behind the curved mirror in the Regen. (a) Pockels Cell switches the beam out when the energy of the pulse is at a maximum. (b) Pockels Cell switches the beam out after it has diminished due to losses in the cavity.

Notice the interplay between the gain and loss in the cavity in Figure 3-7b. As the light oscillates in the cavity, it successively takes more and more energy stored in the Ti:Sapphire crystal. This continues until the energy gained from the crystal is less than the energy lost due to imperfections in the cavity, such as the small transmission through the cavity mirrors monitored by the diode. At this point the energy in the pulse decreases with each pass such as depicted in Figure 3-7b, but not necessarily in the symmetric fashion as illustrated. To obtain the highest pulse energies, the Pockels Cell is switched from its half-wave voltage (where it acts as a half-wave plate), to its three-quarter-wave voltage (which ejects the pulses from the Regen), when the diode signal reaches its peak, as shown in Figure 3-7a. This technique of selecting when to eject the pulses is called cavity dumping.

One problem that has not been completely remedied is the generation of pre-pulses in the beam. Each time the seed pulse oscillates in the Regen cavity, as small amount of light is switched out by the polarizer due to the small imperfections in the cavity. This leakage can be measured by putting a diode into the laser beam such as in Figure 3-8 (along with some very strong attenuation, such as multiple pieces of paper). Because of this, the energies measured during the experiments are not contained in a single pulse, but spread over a number of them. In Figure 3-8 about 60% of the energy is contained in the main pulse. This unfortunately was not considered until after the experiments had been completed, and so there is no complete record of the pre-pulses for each scan. However, Figure 3-8 was a pretty standard trace, and as such it will be assumed that approximately 60% of the recorded energy is contained in the main laser pulse for the entire study.

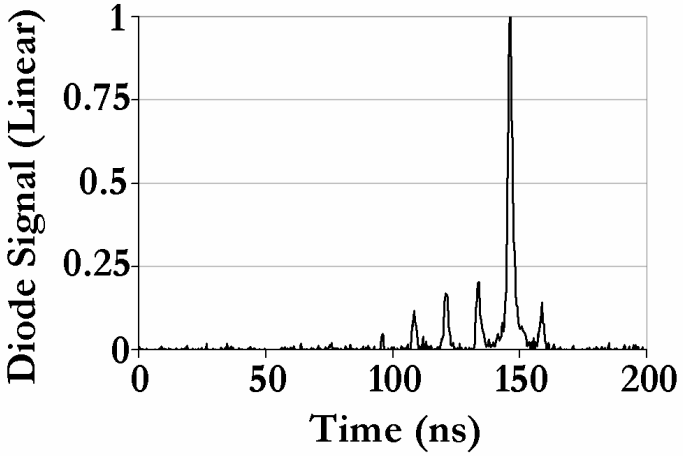

Figure 3-8: Signal from a diode placed directly in the beam

3.2.3. Beam Control

It is important in the operation of the dual-wavelength Regen that one can independently manipulate the characteristics of the two beams, such as their central wavelengths, their bandwidths, and the relative energy and timing between them. As such, the cavity was designed to include elements that could provide this control. The wavelength and bandwidth of the individual beams can be adjusted using slits that are placed after the prisms, as the spectra are then spatially dispersed. The slit width allows one to reduce the bandwidth of the pulses, and the slit positions control the central wavelengths. The relative timing between the pulses can be adjusted by using a translation stage on one of the back mirrors (see Figure 3-5), where it is desirable for the two pulses to be overlapped in time. To adjust the energy of the pulses, one can insert a polarizer/half-wave plate combination in one of the arms to provide a variable attenuator. This is placed in the short-wavelength arm of the Regen, as the shorter wavelengths tend to experience more gain than longer ones, and can therefore afford the loss. In a limited way, one can also adjust the energy balance by adjusting the position of the pump beam in the crystal using its lens. This controls the relative gain seen by each beam, as the two beams diverge slightly in the crystal due to the dispersion of the index of refraction, as shown in Figure 3-9. The typical energy in the pulses from the Regen was about 2.5mJ for pulses with central wavelengths of 780nm and 830nm, which is consistent with what was obtained in Zhang et al (2000).

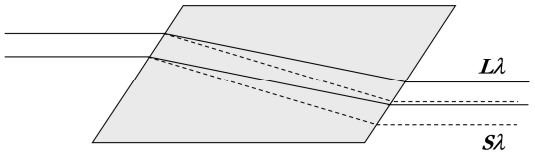

Figure 3-9: Illustration of the divergence of the two pulses as they propagate through the crystal. The short-wavelength beam is denoted Sλ, and the long-wavelength beam is denoted Lλ.

3.3. Multipass Amplifier

To increase the energy of the pulses further, the high-energy multipass amplifier developed by Xia et al (2002) was used. As opposed to a regenerative amplifier there is no cavity; it is instead through the redirection of the beam by a series of mirrors that the pulses go through the crystal multiple times (Figure 3-10). The somewhat complicated setup of using two turning mirrors on each pass was used due to the observation in Xia et al (2002) that the two colours of the Regen were spatially separated by 1mm, and that by using the two turning-mirror setup, the beam separation could be reduced with each successive pass. Going into

the crystal from the right, the short-wavelength beam would be below the long-wavelength beam as depicted in Figure 3-9 and as such should come together as they pass through the crystal, but to do this from the left, the short-wavelength beam should be on top. Switching the relative position of the beams is not possible with a single redirecting mirror, and so a pair of them are used.

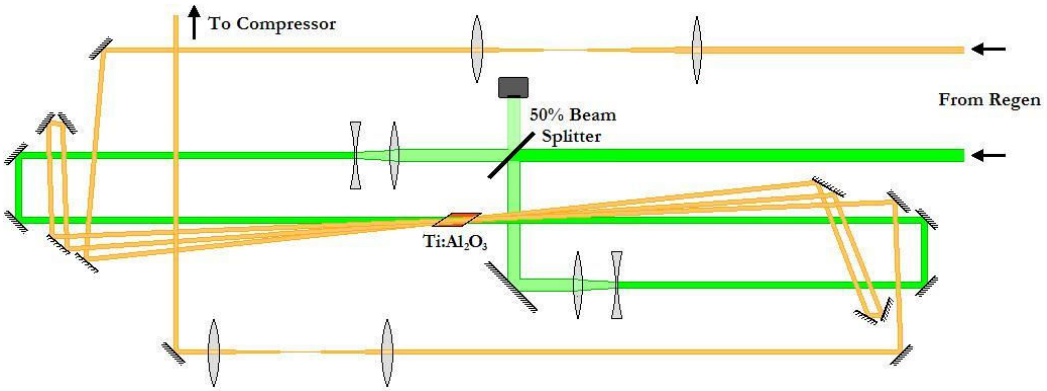

Figure 3-10: Illustration of the multipass amplifier when working in a three-pass operation. This was increased to five passes for much of the experiment to increase the available energy.

While the losses for each pass were consistent with the small reflection losses expected (~6% loss with each pass), the net gain in the system was poor compared to that reported in Xia et al (2002). The total energy in the pulses was 14mJ directly out of a five-pass amplifier, which is approximately a five-fold increase from the typical 2.5mJ out of the Regen. This is compared to the 30mJ output that was reported in Xia et al (2002) with input pulses of 1.5mJ. The discrepancy between these amplification factors could in retrospect be due to the new seeding arrangement. The multipass design shown in Figure 3-10 was used to compensate for a separation of the beams, which was thought to have been caused by the divergence of the beams through the Ti:Sapphire crystal in the Regen. However, recall the discussion in **§3.2.1** about the Faraday Isolator acting as a wedge, due to the fact that the reflection through it's polarizer was not exactly 90°. In the configuration of Xia et al (2002), the Faraday Isolator was set in such a way that the Regen pulses would go through this wedge, and thus would diverge given their separation in frequency. By switching this configuration to instead make the seed go through this wedge, the divergence of the Regen pulses was corrected before the multipass, and therefore instead of bringing the two pulses together, the two turning-mirror setup would actually be separating them. This was realized after our experiments, however at the time it was decided that 14mJ was enough to conduct our investigations.

3.4. Grating Compressor and Autocorrelator

A three-grating compression system was used to compress the two-colour output from the amplifiers, which is based on a standard negative dispersion grating compressor [Treacy 1969], and as reported in Xia et al (2002) had a transmission of approximately 50%. By convention, when light of a low frequency travels faster than light of higher frequencies the material dispersion is said to be positive, and it is positive dispersion that is typically observed in normal transparent media (see Figure 3-2). When the light has been dispersed in this fashion, it is often said to have a positive chirp, where the term "chirp" comes from the sound of a bird. If observed, the dispersed light should sweep from low frequencies to high frequencies, which with acoustic waves makes the sound of a chirp. Having then stretched a pulse through material dispersion, one would need a system to apply a negative chirp to recompress the pulse using a negative dispersion. While this is difficult to obtain in normal materials, various geometrical arrangements of normally dispersive elements can be constructed to advance higher-frequency light as compared to lower frequencies. Figure 3-11 gives an illustration of negative dispersion using a system of gratings, and it is this setup, with a plane mirror placed after the first set of gratings, which is used to apply negative dispersion in the compressor. However, due to the large frequency separation of the two beams, three gratings and two plane mirrors are used instead of two gratings and one plane mirror, where in analogy with Figure 3-11, after the initial angular dispersion each beam would have its own grating and plane mirror. To redirect the beams towards the experiment, these plane mirrors are then tilted slightly downwards towards a lowered mirror earlier in the setup, much like in the seeding apparatus of Figure 3-6 (this is again described and illustrated in Appendix B.5).

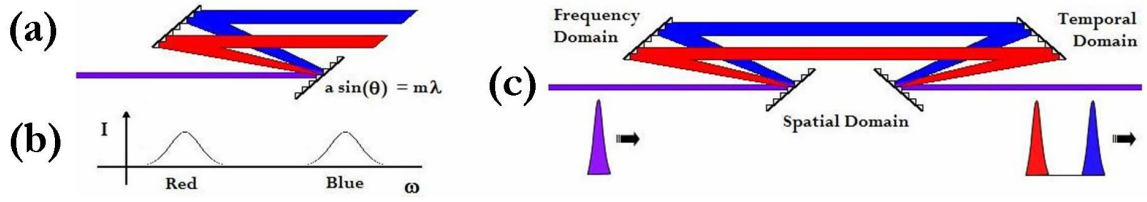

Figure 3-11: Negative dispersion. (a) Due to their angular dispersion, a pair of gratings will advance high-frequency light ahead of lower frequencies. (b) Spectrum of the beam in part (a). (c) Stretching a pulse with negative dispersion. A positively dispersed pulse will be compressed by this system. Instead of adding an extra pair of gratings, a plane mirror is often placed after the first pair.

To determine the dispersion necessary to compress the pulses, the pulse widths are monitored by a non-collinear single shot autocorrelator [Janszky 1977], where a schematic of this device is shown in Figure 3-12. Essentially, one of the two beams is sent through a periscope to switch the polarization from p-polarized (parallel to the optical bench), to s-polarized (perpendicular to the optical bench). The light is then split using a 50-50 beamsplitter, where one arm contains a delay line to time up the pulses. The two beams are then sent at an angle through a birefringent frequency-doubling crystal, which in this case is a 0.25mm thick Barium Borate (BBO) crystal. The overlap of the beams in the crystal produce frequency-doubled light, where the direction of the resulting beam is given by the sum of the wavevectors from the two pulses, and its width gives a measure of the temporal duration of the pulses via the pulse autocorrelation. The 2ω light is then recorded on a CCD camera to give a single-shot determination of the pulse length.

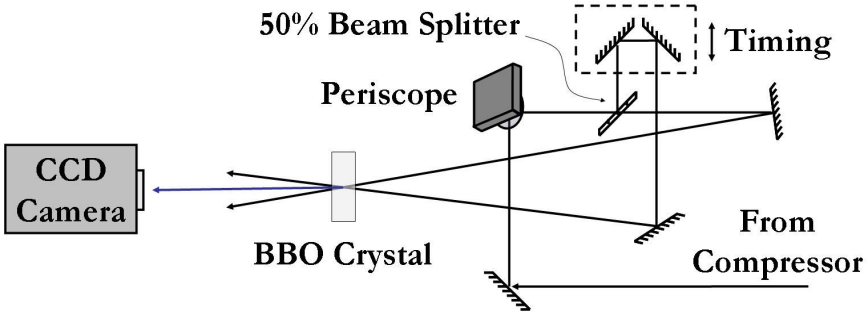

Figure 3-12: Single-shot non-collinear autocorrelator.

To get a sense of how this gives a measure of the temporal duration, refer to Figure 3-13. As the two pulses propagate through the crystal (propagation is shown by the dotted lines), they generated frequency-doubled light in three directions: each individually makes a frequency-doubled beam along its own path, and when they overlap they produce frequency-doubled light that, due to momentum conservation, propagates in a direction that is the vector sum of the directions of the two pulses. The integrated sum-frequency light that is generated from this overlap is called their autocorrelation, and in general the shape of the distribution depends on both the temporal and spatial profile of the pulses. The resulting distribution recorded by a camera gives a measure of the pulse duration (see Figure 3-14), where the width of the autocorrelation distribution must be scaled by an appropriate form factor when determining the pulse width, to take into account the fact that the pulses overlap more in the centre of the distribution than at the edges. A simple approximation of the autocorrelation width is given by Kolmeder et al (1979), where it is linear with respect to

the pulse length if the longitudinal width of the pulse (c times the pulse duration), is less than one third of the beam diameter. As the beams used in this experiment were 3mm FWHM, the maximum pulse duration that can be measured should be approximately 3ps.

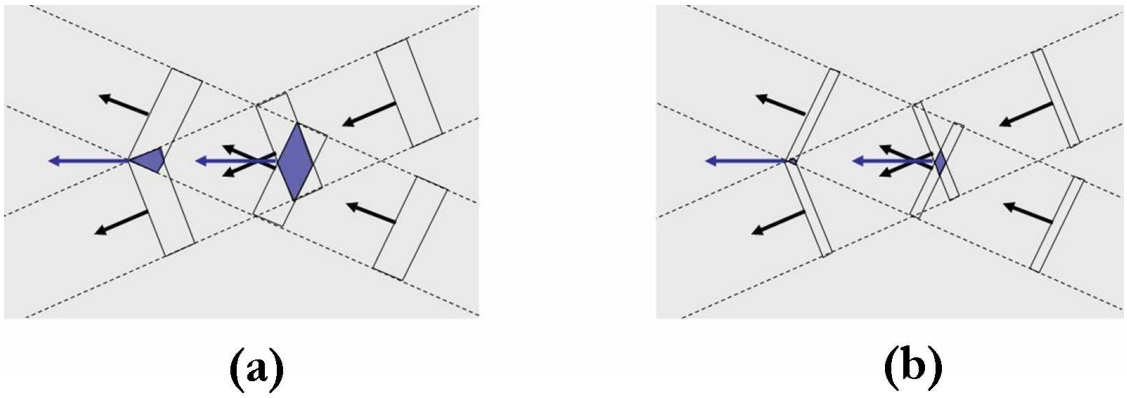

Figure 3-13: Sum-frequency generation using two identical non-collinear pulses. Note how the vertical dimensions of the generated light depend on the temporal width of the pulses.

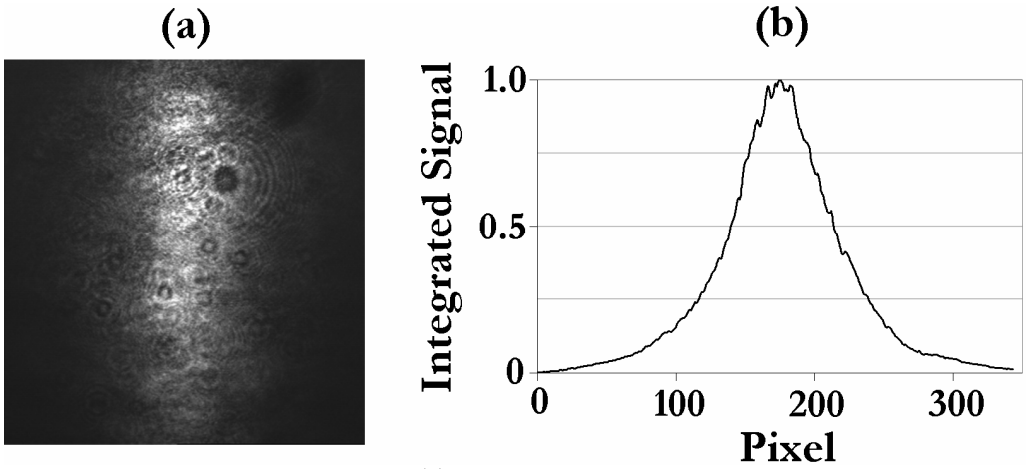

Figure 3-14: Sample Autocorrelation. (a) Time-integrated sum-frequency signal as recorded by the camera. (b) Profile as determined by the camera (summed along the y-axis)

To characterize the operation of the autocorrelator, two scans needed to be conducted. The first was a calibration of the time per pixel as recorded on the CCD camera, where one pulse was delayed with respect to the other and the centre of the generated distribution was recorded. The result of the calibration is plotted in Figure 3-15a, where a linear regression found a scaling factor of about 7.3fs per pixel. Note that the time scale in Figure 3-15a has been divided by $\sqrt{2}$, which corresponds to the autocorrelation form factor for Gaussian pulses. This form factor was included in the calibration to simply save time in the analysis, as it was assumed for the duration of this experiment that the pulses were Gaussian.

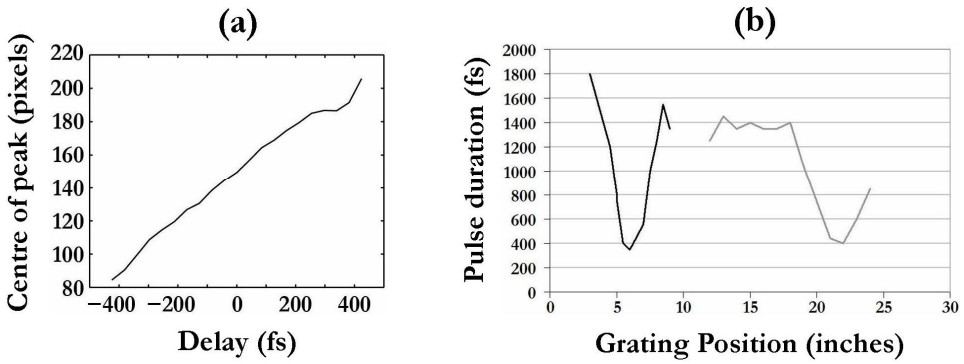

Figure 3-15: Scans using the autocorrelator. (a) Mapping the pulse delay to the peak position on the CCD camera. (b) Mapping the grating position to pulse width. The black line shows the width of the long-wavelength pulse, and the grey line shows the width of the short-wavelength pulse.

The second scan was a study of the pulse width with the grating position, which used the previous calibration to determine the pulse widths as observed by the CCD camera. This is shown in Figure 3-15b, where it was found that the maximum measurable pulse width was approximately 1.4 picoseconds, which is not too far from the predicted maximum pulse width of 3ps. The grating position is not taken with respect to anything meaningful – it is simply measured from a convenient spot on the optical bench. However, one thing to note is that the long wavelength grating is found closer to the first grating than the short wavelength grating. This is opposite to what would be expected, as can be seen in Figure 3-11 where the red beam (long wavelength) is further away from the first grating than the blue beam (short wavelength). This discrepancy can be attributed to a mismatch in the third order dispersion experienced during the stretching and compression of the pulses. As a significant amount of second-order dispersion was required to stretch the pulses, a large amount of third-order dispersion was added as well, which could not be perfectly matched by the gratings [Backus 1998]. This mismatch limits the compression possible with this setup, and while it was not corrected for this experiment there are plans to replace the long fibre used to stretch the seed with a grating stretcher, which in principle should be better matched to the grating compressor.

3.5. Hollow Fibre Assembly

As is often used for nonlinear optics in a gas, this experiment was conducted in a fused-silica hollow dielectric waveguide, primarily to increase the length of the beam focus (which in this case was increased from approximately 4cm to 1m), but also to contain the beam in a single,

highly selective mode. This is especially important in MRG because of the detrimental effects of the Raman defocusing described in Syed et al (2000) and Losev et al (2002a).

Described originally by Marcatili & Schmeltzer (1964) using a modal analysis, the waveguiding properties may at first seem counter-intuitive, given that the light is trapped in a region with a low index of refraction as opposed to a regular fibre-optic waveguide where a beam is trapped in a region with a high index of refraction. However, the conditions necessary for coupling efficiently into the fibre [Abrams 1972; Mohebbi 2004], mean that the beams are actually focussed at relatively small angles into the fibre, roughly at 0.2°. Upon consideration of the Fresnel coefficients of a dielectric, the waveguiding nature of the hollow fibre can be realized as simply small-angle reflections from the inner surface [Nisoli 1996], given that any smooth surface acts as a mirror at small angles.

Two hollow fibres were used in the experiment, one with an inner diameter of 250μm and one with an inner diameter of 129μm. Two different fibres were used to examine the effect of their plasma-like dispersion – according to the modal analysis of Marcatili & Schmeltzer (1964) the hollow fibre exhibits negative dispersion, where longer wavelengths travel slower than shorter ones. Balanced with the normal dispersion of SF_6, this should produce zero dispersion point at a particular frequency. This is illustrated in Figure 3-16, where the group delay is plotted for (a) SF_6 by itself, (b) SF_6 in a hollow fibre with an inner diameter of 250μm, and (c) SF_6 in a hollow fibre with an inner diameter of 129μm. The group delay gives a measure of how much one frequency is delayed with respect to the other, where the minimum corresponds to the point of zero dispersion. Note that these group delays are all taken relative to the group delay of SF_6 at zero frequency, and all are calculated assuming the SF_6 is at a pressure of 1atm.

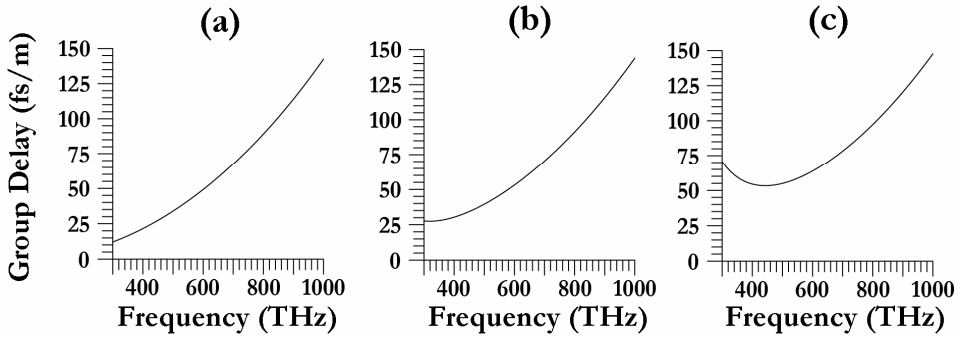

Figure 3-16: Balance between the normal dispersion of SF_6 and the negative dispersion of the hollow fibre. (a) Group delay (GD), of SF_6 relative to the zero-frequency GD at a pressure of 1atm. (b) GD of SF_6 in a 250μm hollow fibre at 1atm. (c) GD of SF_6 in a 129μm hollow fibre at 1atm.

An example of the setup of one of the fibres is illustrated in Figure 3-17. To couple best into the fibres, the $1/e^2$ beam size at the entrance (or 1/e diameter of the field), should be approximately 60% of the inner diameter of the fibre. As such, we used lenses of 750mm and 300mm to focus into the two fibres. A variable attenuator was placed in front of the apparatus to control the energy, and after the chamber the beam was collimated and redirected towards a variety of diagnostics.

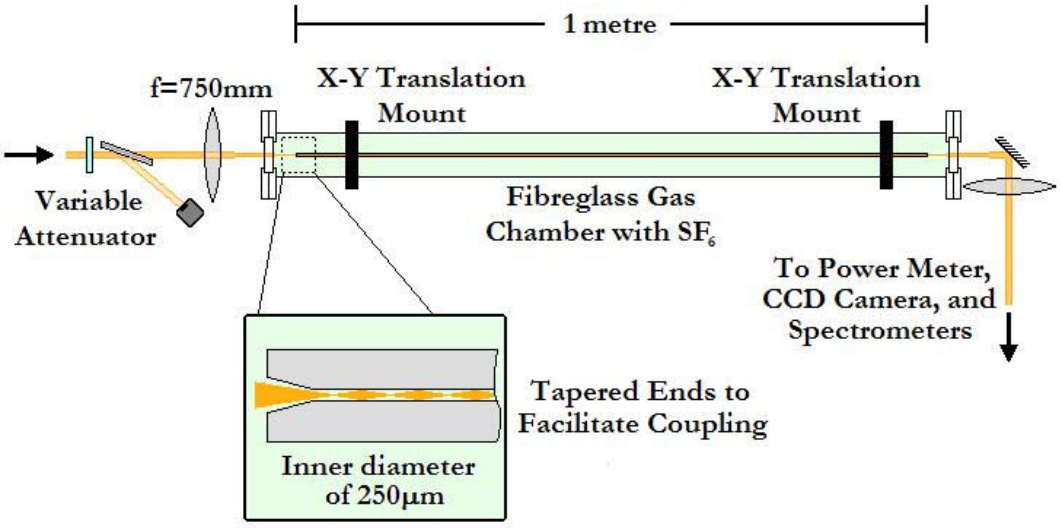

Figure 3-17: Illustration of the hollow fibre apparatus. Note the inset showing small-angle reflections.

The high-pressure fibreglass chamber designed by Mr. Robin Helsten contained a v-groove aluminium bar to seat the hollow fibre, which was made as straight as possible to minimize transmission losses. To facilitate alignment, two X-Y translation mounts were positioned at the tips of the fibre, which should provide independent control of the position of the entrance of the fibre and the angle of the fibre. The ends of the fibre were sealed with 2mm thick windows plus end caps, with a vacuum-grade seal provided by greased O-rings and a gas delivery system designed and built by Mr. Jean-Paul Brichta. This chamber was filled with SF_6 gas with pressures from one to three atmospheres. Typically, transmission through the assembly with the 250μm fibre was about 17%, and that through the 129μm fibre was about 7%. This is low compared to what is expected [Marcatili 1964], which we attribute to coupling and surface-roughness in the fibres.

The alignment of a hollow fibre was non-trivial to determine initially. Indeed, it is nearly impossible to align the beams through the fibre using mirrors before the apparatus, and as well it is nearly impossible to determine the best alignment using a simple power

meter after the fibre. The main issues were 1) when a beam is misaligned into the fibre it produces a very complex multi-modal output, as opposed to the circular profile of the fundamental hybrid mode, and 2) when the beam is moved slightly from the entrance aperture of the fibre, it can be guided by the glass walls, which gives a false sense of transmission. To overcome this, a procedure was developed in the lab that made use of a CCD camera to view the profile of the pulses, and a piece of paper attached to the end of the fibre to help align the beam to the top of the fibre before sending it in.

The alignment procedure is as follows (refer to Figure 3-18). A piece of paper is first cut and placed on the hollow fibre before sealing the chamber. Using an iris to reduce the size of the beam before the chamber, the beam is aligned without the focussing lens along the top of the fibre, as determined by a grazing reflection from the front surface and the piece of paper at the end of the fibre (Figure 3-18a). This can be done either with the X-Y mounts on the chamber or with two mirrors earlier in the beamline. With the iris still closed, the focussing lens is positioned in the beam such that the beam ends up at the same place on the paper. The iris minimizes the focussing of the beam as it travels through the lens, allowing for an accurate positioning. The fibre is then raised into the beam using the X-Y translation mounts – plane mirrors are definitely *not* used for this part of the alignment or any of the following steps, as the time it takes to get the beam through properly is on the scale of hours, as opposed to the few minutes it takes with the translation stages. As the iris is opened to focus the light properly, the first X-Y translation stage is adjusted to bring the entrance aperture of the fibre into the beam focus, while monitoring the beam as it comes out of the apparatus (Figures 3-18b and c). When the beam is entering the hollow core properly, a tight and diverging circular dot should be observed immediately after the chamber, which should be very sensitive to any adjustments of the first X-Y mount (Figure 3-18b). If the beam enters the glass part of the fibre, it will make a diffuse pattern as in Figure 3-18c, that is diverging far less than the dot from Figure 3-18b, and which is far less sensitive to the adjustments of the first X-Y mount. Once even a weak circular dot is obtained, the light is split using a glass slide and sent to both a CCD camera and a power meter (the front-surface reflection going to the CCD camera). The brightness of the dot can then be monitored on a screen as the alignment is completed using the second X-Y mount, with the power meter used to double-check.

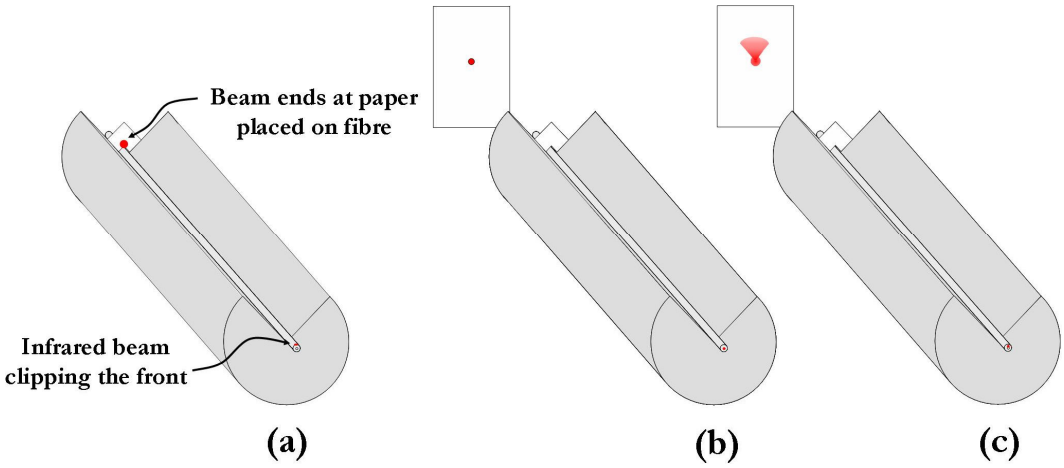

Figure 3-18: Alignment of the hollow fibre. (a) First align the beam to the top of the fibre. (b) Once the beam is focussed into the fibre properly, it should form a tight circular dot as it exits. (c) If the beam is focussed into the glass instead of the core, a diffuse pattern is formed.

3.6. Diagnostics

The ultra-broad bandwidths obtained in MRG span beyond the visible spectrum and into the infrared and ultraviolet, making its measurement difficult as the instruments used to measure a spectrum are normally optimized for particular wavelength regions. As such, two measuring devices are used in parallel to measure the generated spectrum. For the infrared an Ando Optical Spectrum Analyzer (OSA) is used, as it is optimized for operation in optical communications band which typically ranges in wavelengths from 1.3μm to 1.5μm. Essentially a scanning monochrometer, it is quoted as having a usable range of 400nm to 1750nm, however with its age, the behaviour at shorter wavelengths has become questionable, in that light visible by eye could not be detected by the OSA even on a logarithmic scale. It was therefore typically used in the 600nm to 1750nm region to collect the Stokes orders, along with the pump and a few anti-Stokes orders. The spectrum from about 850nm to 300nm was recorded using an Oriel MS127i Spectrograph – an imaging spectrometer with an astigmatism-corrected Czerny-Turner configuration, where the light entering through a 10μm slit is collimated, dispersed by a grating, and is imaged on a linear CCD array. There is also the addition of an astigmatism-correcting mirror in the MS127i.

To record these two regions of the spectrum simultaneously, the light from the hollow fibre was split using a thin wedge as in Figure 3-19. The transmitted light was sent to the OSA, where a piece of tape moderately diffused the beam before it went into the fibre optic coupler to correct for any angular dispersion due to the wedge. The front edge reflection was sent to the Oriel Spectrometer (referred to hereafter as the spectrometer), to

avoid absorption in the ultraviolet portions of the spectrum by transmission through the wedge. It was then attenuated by a second reflection from a wedge to avoid saturation in the spectrometer, where only the front-surface reflection from each wedge was used. This reflective attenuation was chosen as opposed to using the absorptive neutral density filters available in the lab, because even though their response should be flat across the spectrum, it was found that these filters attenuated longer wavelengths more than the short-wavelength anti-Stokes orders. This could possibly have been due to some nonlinear absorption or saturation effect, as the strong pump beams are in the infrared and should reach the filters before the anti-Stokes orders due to dispersion.

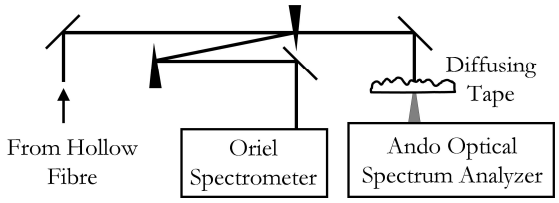

Figure 3-19: Schematic of the measurement apparatus. The light transmitted through the second wedge was blocked.

In terms of collecting the data, the OSA would output a simple text file with two columns of data, one for the wavelength and one for the intensity. As the dynamic range was very good, only one scan needed to be taken for a given spectrum. While the spectrometer would also output two columns of data, it suffered from a number of issues that made the analysis problematic. A typical output was shown in Figure 3-20, where the Pixel number on the linear CCD runs from 0 to 2009, and the intensity reading runs from 0 to 4095. The main problems with using the spectrometer were 1) it could not be triggered, with the result that laser shots were occasionally missed or extra ones added, increasing the range of intensities over which saturation was observed, and 2) there was a very large threshold in its intensity measurement, which reduced the usable dynamic range to at best a single order of magnitude. This small dynamic range necessitated the accumulation of a number of scans for each spectrum, where from one scan to the next the integration time of the CCD camera was increased by a factor of 2. To ensure that the scans were directly comparable, for each integration time the number of shots to average was chosen to keep the number of total number of shots constant. A linear regression between the two scans was then determined in Excel to patch the scans together and form a single spectrum, which resulted in a dynamic range larger than that possible with a single scan.

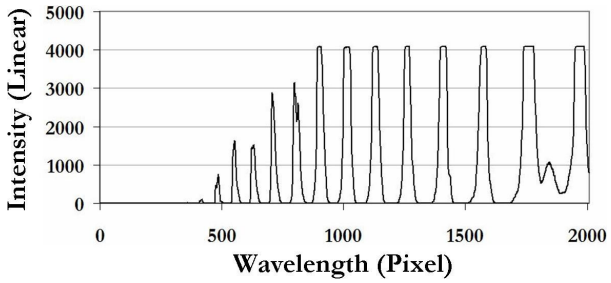

Figure 3-20: Typical plot from the Oriel Spectrometer

To demonstrate how these behaviours affect the analysis, refer to the plots in Figure 3-21. The intensity of two successive scans were plotted against each other (and therefore two successive integration times), where each data point is at a coordinate of

$$(x, y) = (\textit{Intensity of Short Integration},\ \textit{Intensity of Long Integration})$$

for a particular pixel number. One would predict a linear regression of y = 2x, as the integration time had simply increased by a factor of two. However, as can be seen in Figure 3-21a, this plot is far from linear, which is due to saturation effects and the fact that the spectrometer could not be triggered, which contributes to the curvature of the plot at lower intensities. Therefore, any data points that did not exhibit a linear behaviour were deleted. Specifically, the data points at the threshold of the detector are deleted (where the intensity of the short integration time is less that 100), as in (Figure 3-21b), and any near the saturation of the detector are deleted (where the intensity of the long integration time is greater than 3000) (Figure 3-21c). To avoid skewing the fit, all points along the x-axis after the first saturated data point are deleted as well (see the shaded areas in Figure 3-21). A least-squares linear fit is then determined with the remaining points.

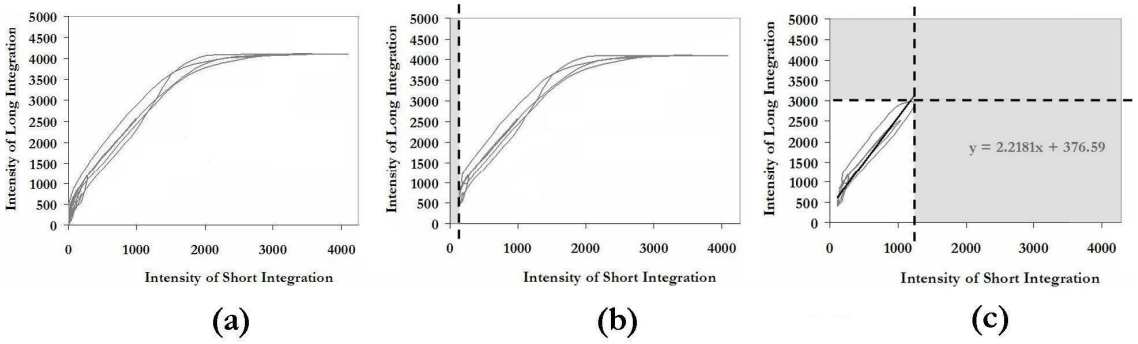

Figure 3-21: Generating a linear regression with the spectrometer. (a) Raw data, where the intensities between successive scans are plotted against each other. (b) Any points with an x-value below 100 are deleted. (c) Starting at the first point with a y-value above 3000, all points with higher x or y values are deleted. The resulting linear regression is shown.

Note that in Figure 3-21c, the resulting linear regression gives an intercept of 377, which implies that there is a threshold intensity necessary before the CCD reads an intensity. On average, this intercept was about 720, which means that out of the total possible signal that can be read (4095 + 720), 15% of the signal was below the threshold of the detector. Of the usable signal (3000 + 720), 20% is below the threshold, resulting in a dynamic range that is less than an order of magnitude. To overcome this poor range, a series of at least 6 scans were compiled to generate a single spectrum. Starting with the most sensitive scan (the one with the highest integration time), each successive scan was scaled by what was obtained in the linear regression, which when plotted would look like Figure 3-22a. To clean up the spectrum, all intensities below 100 or above 3000 for each scan was deleted, resulting in final spectrum much like Figure 3-22b. Note that occasionally a number of floating peaks can be observed in different parts of the spectrum as shown in the circled area of Figure 3-22b. This is predominantly due to intensity fluctuations in the laser beam, as MRG is a highly nonlinear process and a single compiled spectrum takes approximately 15 minutes to complete. As such, these floating peaks give a sense of the errors bars in the spectra.

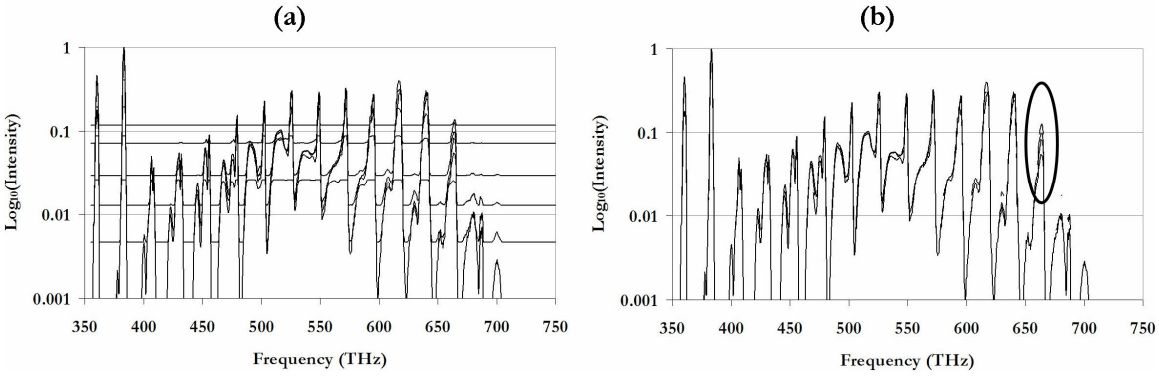

Figure 3-22: Compiled spectrum. (a) Each spectrum is scaled by the constants determined in the linear regression. (b) The spectra are cleaned up by ignoring data points with intensities below 100 or above 3000, on a scale of 0 to 4095. Note the residual multi-peak structure due to intensity fluctuations.

4. Experimental Results & Discussion

The primary aim of this study was to determine the potential of Dr. Strickland's two-colour laser system for the production of high-energy few-femtosecond pulses, by utilizing multifrequency Raman generation in the transient regime. To this end, we first had to establish a reproducible and reliable experimental procedure, during which we fine-tuned or rebuilt each part of the system to maximize the generated bandwidth. After a proof-of-principle measurement where at least 30 Raman orders were generated, attention turned to the scaling of the bandwidth as the energy in the pump beams was adjusted. The results obtained from this scan indicated a number of promising features, such as the preferential growth of the high-frequency anti-Stokes orders and the formation of a plateau on the scale of the short-wavelength pump beam. The scan also demonstrated the limiting effect self-phase modulation has on the potential bandwidth, which provided insight into how to further optimize our apparatus.

Our most recent investigations involved the effect of dispersion of the generated spectrum. As mentioned in **§3.5** the size of a hollow fibre affects its dispersion characteristics, and so a number of studies were conducted in a smaller-diameter fibre where these effects should be apparent. It was shown that dispersion was a very important determinant in the behaviour of the Raman generation, as a very dramatic and counter-intuitive enhancement was observed as the pressure was decreased from 3atm to 1atm. Furthermore, the structure of the generated Raman orders at lower pressures was very interesting, and may possibly point to the interesting physics of soliton formation, though not necessarily the few-femtosecond multifrequency solitons discussed in Kaplan (1994).

4.1. Procedure and Measurement

As in any new experimental investigation, this study experienced a period of trial and error when developing and fine-tuning the experimental procedure. As such, out of the nearly 1000 spectra taken, only a relatively small subset are actually meaningful. Many of the issues encountered were to do with the measurement of the incredibly large bandwidths, most of which were discovered only upon analysis of the data.

Originally the OSA was used to observe the entire generated spectrum, as its quoted range of 1750nm to 400nm should have allowed for the collection of a large number of Stokes and anti-Stokes orders. During these initial measurements with the OSA, at least

three factors were working to corrupt the data, as will be described with the help of Figure 4-1. First and foremost, while the scale of the OSA was in nanowatts on a potential scale of milliwatts, a number of the peaks were strongly saturating the detector (the seven central peaks in Figure 4-1). This saturation was confirmed when absorptive filters were placed in the beam with little effect on the level of the peaks. With some thought this is not surprising – the scale describes the average power of the beam, but the pump pulses being used had peak powers on the order of 100MW. With sufficient attenuation, the intensities as recorded by the OSA eventually demonstrated a linear behaviour.

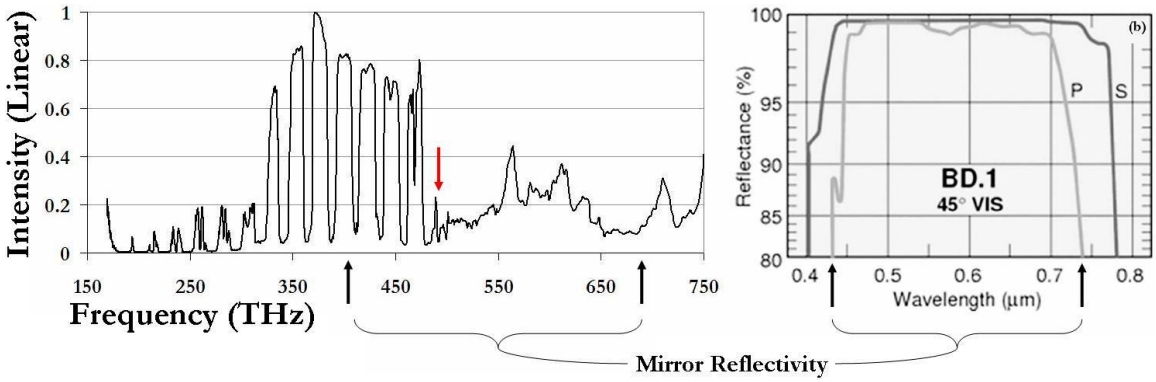

Figure 4-1: Early Ando spectrum and reflectivity curve of a mirror used after the hollow fibre, © Newport Corporation – Used by permission from http://www.newport.com/store/genproduct.aspx?id=141092&lang=1033&Section=Spec.

Secondly, the mirrors that were being used after the fibre had reflectivity curves that did not cover the entire generated spectrum, in particular the silver BD.1 and ER.2 coated mirrors from Newport. The BD.1 curve taken from the Newport website is shown in Figure 4-1, and the corresponding reflectivity range is shown within the arrows. Note that below the pump frequencies of 352THz and 375THz the intensity of the spectra drop dramatically, which would be expected as the reflectivity drops below 428THz. The final problem encountered is highlighted by the arrow pointing down at the Raman order at ~500THz. This order, which is very weak as depicted by the OSA, was easily visible to the naked eye. Given this fact along with 1) the other orders were strongly saturated and 2) the fact that the mirrors were nearly perfect at the wavelength of that Raman order, it was concluded that the OSA could not properly detect wavelengths around and shorter than 600nm (500THz). As the behaviour of the OSA in this wavelength region could not to be trusted, the spectrometer was chosen as the primary measurement device, whereas the OSA

was used to only monitor the Stokes orders that the spectrometer could not detect (the range of the spectrometer was ~350THz to 1000THz).

The next issue encountered involved the scaling of the spectra to one another. As is described in **§3.6**, the spectrometer suffered from a small dynamic range due to its large threshold intensity, and as such required the compilation of a number of scans, where either the intensity of the light or the integration time on the CCD was adjusted. Originally, both of these techniques were used to scale the data, where the light was attenuated by using absorptive Neutral Density filters (ND filters). Unfortunately, possibly due to the large intensities involved in the experiment, the ND filters did not exhibit a flat attenuation as expected, but imparted a frequency-dependent attenuation on the beam. This went unnoticed for a significant amount of time, as it was only definitively demonstrated using the most recent technique of compiling the spectra. Figure 4-2 gives an exceptional but somewhat involved example of how the filter affected the light. As described in **§3.6**, the most recent method of compiling the data consisted of determining a linear regression between consecutive intensities, and using those scaling factors to patch various spectra together. Figure 4-2a demonstrates an example where the integration time was decreased by a factor of two, where its characteristic linear then saturation behaviour was described in **§3.6**. In contrast with this regular behaviour, Figure 4-2b shows the effect an extra filter had on the spectrum. Notice the erratic behaviour in the graph describing the filters – in some places the intensity has even been increased with the addition of an extra filter (high x value, low y value). The path that the curve follows is determined by the intensities of each pixel in turn, from pixel #0 to pixel #2009. For example, the first two data points on the graph would be (x_1, y_1) = (Intensity of Pixel #0 with 4 Filters, Intensity of Pixel #0 with 3 Filters) and (x_2, y_2) = (Intensity of Pixel #1 with 4 Filters, Intensity of Pixel #1 with 3 Filters). This helps to give a sense of how the attenuation changes as the wavelength increases.

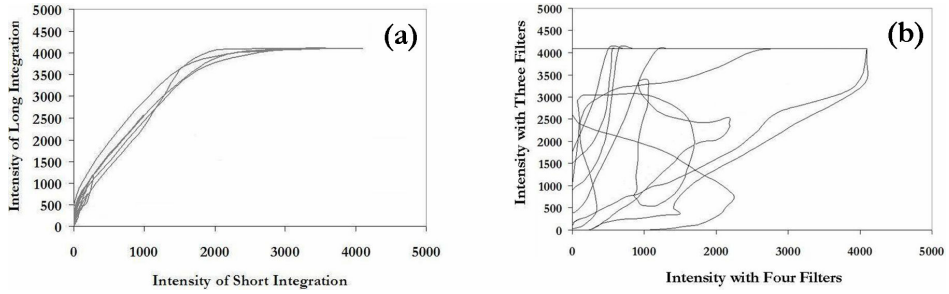

Figure 4-2: Anomalous behaviour of an absorptive filter vs. a change in integration time. (a) Integration time had been changed by a factor of two. (b) An extra 50% filter was placed in the beam.

Figure 4-3 gives a more concrete demonstration of this erratic attenuation, where two consecutive spectra are simply plotted as they were recorded from the Oriel. The two features of note are denoted as (a) and (b). In (a), numerous orders in the spectrum with the extra filter have actually grown, as opposed to the normal attenuation experienced beyond Pixel #1100. In (b), the troughs between the Raman orders also give a good indication of this wavelength dependence, as demonstrated by the curves drawn in the plot. To avoid using these filters, the setup was modified such that the generated spectrum was attenuated by the front-surface reflections off of two glass wedges before being sent into the spectrometer, as depicted in Figure 3-19. With this arrangement, the pumps would not saturate the spectrometer when set on the shortest possible integration time (which is determined by the 10Hz repetition rate of the two-colour laser).

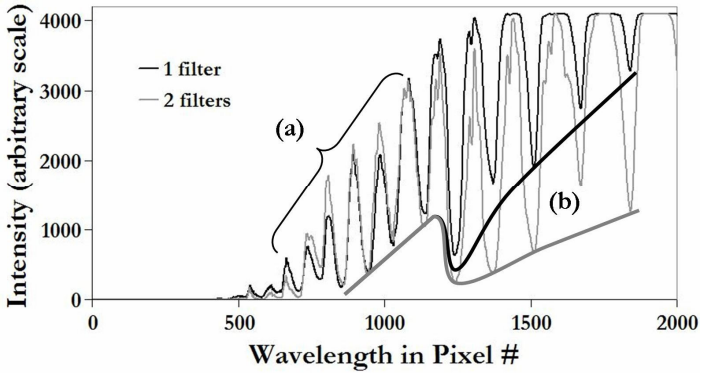

Figure 4-3: Two consecutive spectrometer plots where an extra filter had been added. (a) Some parts of the spectrum experienced an enhancement with the addition of a filter. (b) The troughs give a sense of the wavelength-dependent attenuation, as the lines drawn on the graph show.

The final problem to be discovered was how sensitive the pulse compression was to the wavelengths set in the Regen. As part of the normal experimental procedure, once a small amount of MRG is observed, all possible parameters are adjusted to maximize the generated anti-Stokes spectrum, including the relative timing between the pulses, the energy balance, and the wavelength separation. However, due to the intensive nature of the autocorrelation measurement, and the fact that it required redirecting the laser beam, the compression was typically set before aligning the beams into the fibre. It was only recently discovered that by adjusting the wavelengths a few nanometres (within the bandwidth of the pulses), the pulse duration could as much as double in length. This could possibly be due to the mismatch between the third-order dispersions of the fibre stretcher and the grating compressor, which as mentioned is an issue that is being addressed in the laboratory by replacing the fibre stretcher with a grating stretcher. To accommodate this sensitivity, the

autocorrelations are re-measured after each series of adjustments by using a removable mirror to redirect the beam.

4.2. Demonstration of Broadband MRG

The first benchmark to be met was a proof-of-principle demonstration of our capability to produce large bandwidths. Our first attempts were conducted using the Regen alone, however bandwidths comparable to those reported in the literature were only obtained after the introduction of the multipass amplifier. By maximizing the compression, pressure, and energy in the beams we were able to generate at least 30 Raman orders spanning 750THz. In particular we used two beams centred at 384THz and 359THz with a total of 3mJ split between them with a ratio of ~1.6: 1. Recall however the discussion in **§3.2.2** where the pre-pulses contained ~40% of the energy, and as such there was really only 1.8mJ to split between the two beams. These beams were then compressed down to ~300fs, and were focussed into a 250μm hollow fibre which held SF_6 at a pressure of 3atm. The resulting spectrum is shown in Figure 4-4, where the grey curve is that recorded by the OSA, and the black is the data compiled from the spectrometer. Apparent in the graph is a large continuum pedestal generated by the competing effect of self-phase modulation, which acts to redirect energy from the MRG process. At this point, we had not realized the absorptive ND filters were applying a frequency-dependent attenuation to the spectrum, and so the most intense orders were attenuated using these filters. While the absolute scale of the orders may therefore not be accurate, the generation of at least 30 Raman lines demonstrated significant conversion into broadband light, especially considering that the ultraviolet orders were visible to the naked eye (after fluorescence from white paper, much like in Figure 1-1b).

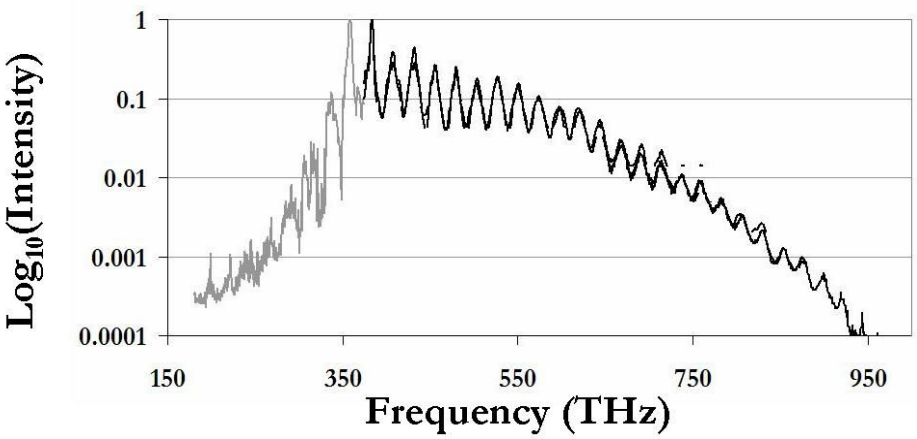

Figure 4-4: Generated MRG spectrum using two compressed pulses with a total energy of 1.8mJ.

As a short digression, the difference between the most recent technique described in **§3.6** and the original procedure is demonstrated in Figure 4-5, using the anti-Stokes spectra in Figure 4-4. Note that both the shape of the spectrum and the relative scale of the peaks are widely different between the two plots – in the second plot, the continuum base is not apparent until the ninth anti-Stoke order, and the total scale is larger by two orders of magnitude. This behaviour is due to the fact that in the original method, the various spectra were scaled by matching one peak from one spectrum with the same peak from another, assuming that the spectra were different by simply a multiplicative factor. This did not take into account the threshold of the spectrometer, and relied on the very subjective decision of which peaks to use from each spectrum. The method described in **§3.6** is now taken as standard, as it allows for a more accurate depiction of the spectra and because it relies on an algorithm that does not require any subjective decision making.

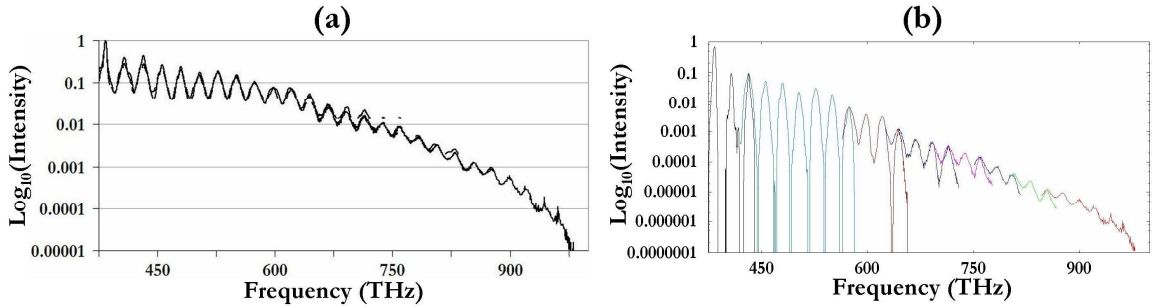

Figure 4-5: Comparison between compilation methods for the spectrometer. (a) The compilation described in §3.6 (b) The original compilation. Note the different scales on the y-axis.

4.3. Demonstration of Pump-Probe MRG

As both impulsive and adiabatic pump-probe schemes have been demonstrated in the literature [Nazarkin 1999a; Liang 2000], we decided to follow suit and explore a transient pump-probe setup. A frequency-doubled probe pulse was introduced into the system by simply placing a BBO crystal into the pump beams as they were being focussed into the hollow fibre. This setup generated a three-frequency probe pulse, which consisted of the doubled frequency from each pump plus the sum-frequency between the two. As the pump beams used in this scan were the same as those that generated the spectrum in Figure 4-4, this led to a probe with frequencies of 718THz, 743THz, and 768THz. The results of this experiment are shown in Figure 4-6, and are comparable to the best pump-probe results published to date [Nazarkin 2002].

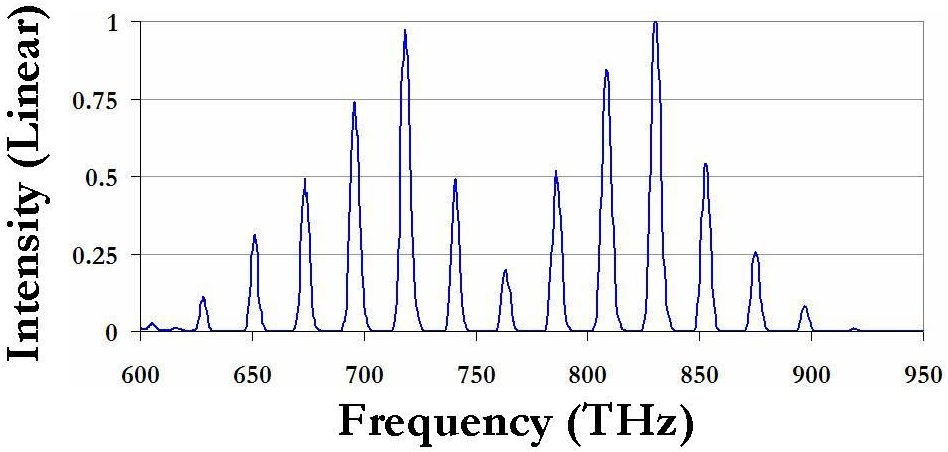

Figure 4-6: Modulated probe beam. The total energy contained in this spectrum was 47μJ, accounting for pre-pulses.

Given the relative ease of this technique, a scan of the probe spectrum was conducted as a function of pressure. As the gas chamber could only be used for pressures above one atmosphere up to a maximum of 3atm, the pressures were taken at intervals of 5psi, or approximately one-third of an atmosphere. For this reason the pressure will be quoted as being 1atm + ***x*** psi. The resulting scan is shown in Figure 4-7, where the shaded areas show regions of the spectrum that were saturating. Note that the BBO crystal had been adjusted prior to the pressure scan, and as such the spectrum in Figure 4-6 is not included in the scan. The behaviour was not found to be overly dramatic, as the main features were 1) a bandwidth that decreased as the pressure was decreased, and 2) some variation in the relative intensities of the peaks. These are both easily explained in reference to **§2**, where the generated bandwidth was shown to depend on the pressure (i.e. the number of molecules ***N***), and the amplitude of the Raman orders were shown to possess an oscillatory Bessel-like character.

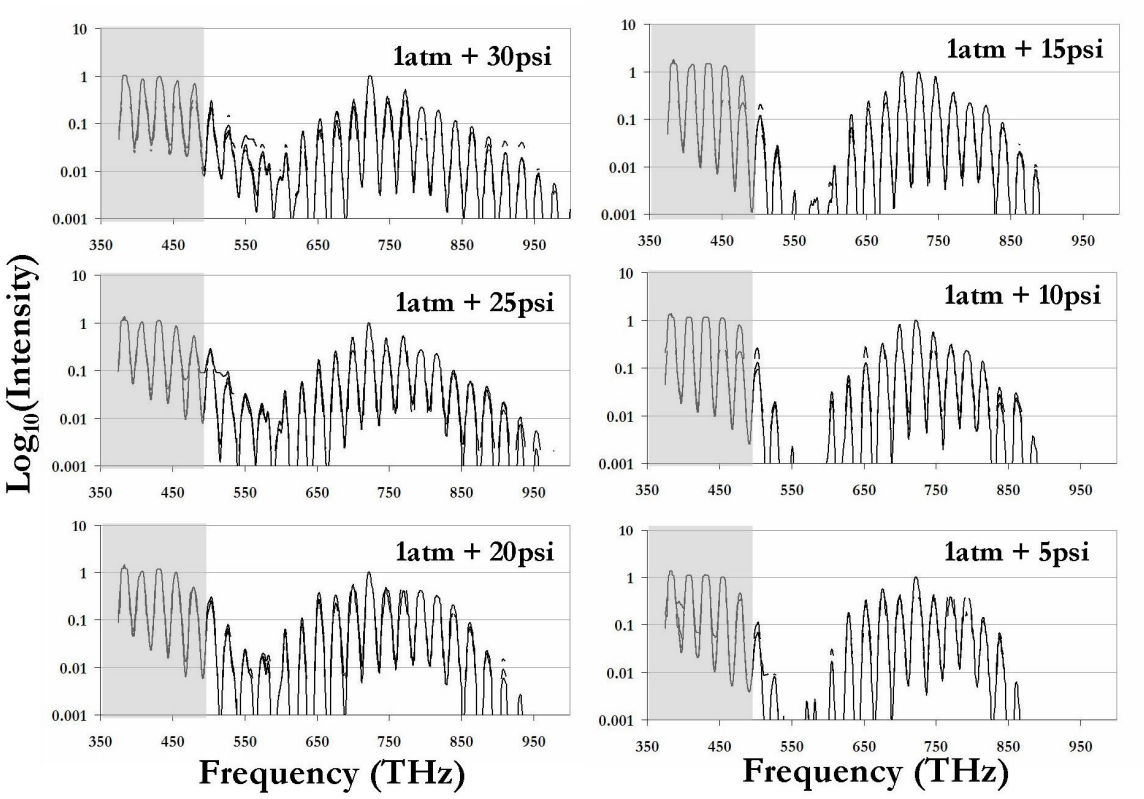

Figure 4-7: Pressure scan of the modulated probe. The shaded region shows the saturated MRG spectrum of the IR pumps.

4.4. Five-pass Amplifier

Following these initial demonstrations, further efforts focussed on obtaining a scan of the generation with intensity, which had not to that point been discussed in the literature. To assist in this exercise, the number of passes in the multi-pass amplifier was increased from three to five, which at its best supplied double the energy that was attainable with three passes. While testing the new multipass and the new procedure of using reflective attenuation instead of absorptive filters, again an ultra-broad spectrum was obtained that contained a significant amount of SPM, which broadened the orders to produce a continuum pedestal. This is apparent in figure 4-8a, where the pressure was again set at 3 atmospheres, the pump beams were set to frequencies of 380THz and 357THz, and the energy contained in the pulses were 2.6mJ and 0.07mJ respectively accounting for pre-pulses. Recall that as a standard procedure, the beam parameters were adjusted to maximize the output, and so the large difference in the energies is a result of this optimization process as opposed to any deliberate intent. Unfortunately, no autocorrelation had been taken after

these adjustments to give an accurate sense of the relative intensities. However, what is interesting is the strong similarity in the way it drops off exponentially at higher orders as compared to Figure 4-4 (reproduced in Figure 4-8b for comparison). By taking a fit of the anti-Stokes peaks from orders 6 to 20 in Figure 4-8a and the orders from 10 to 21 in Figure 4-4, they were found to drop off as $e^{-1.76n}$ and $e^{-1.74n}$ respectively, where n stands for the index of the anti-Stokes order.

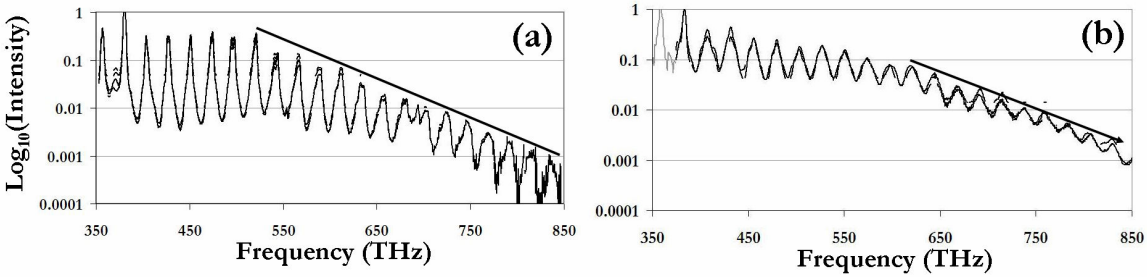

Figure 4-8: Two MRG spectra with strong SPM, where the line placed on each spectrum is meant to lead the eye along the spectrum's exponential decay. (a) Spectrum obtained with five passes in the multi-pass amplifier with . (b) The spectrum in Figure 4-4, where the multi-pass had three passes.

Next, we again tested the efficiency with which the pulses could scatter a probe beam. Surprisingly, much stronger conversion was observed than in the case of Figure 4-7, where the pump energies were more evenly matched. As a comparison, the MRG spectrum of Figure 4-8a is re-plotted on a linear scale next to the spectrum that contained the probe (see Figure 4-9). The scattered probe pulse in (b) shows Raman orders that are much more intense than the MRG spectrum in Figure 4-9a (relative to the pump beam). This conversion has been the best obtained with our technique to date. Note that the frequency scale in Figure 4-9a is replaced with a picture taken of the spectrum after being dispersed by a prism to give some sense of what the orders looked like by eye, compared to what is recorded by the spectrometer.

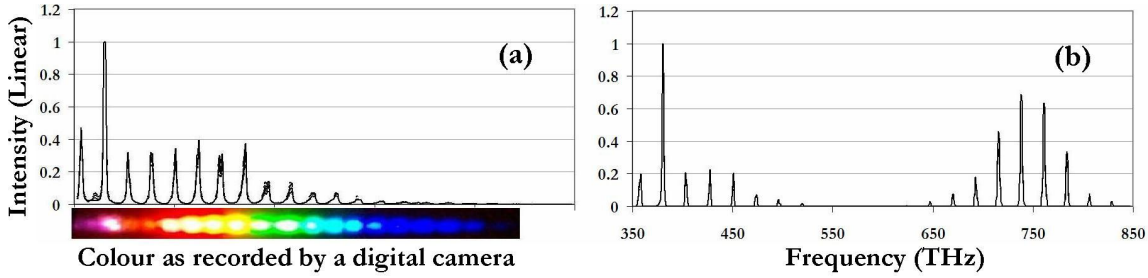

Figure 4-9: Spectra obtained with a five-pass amplifier. (a) Figure 4-8a on a linear scale. (b) Scattered probe pulse using the pumps in (a).

4.5. Intensity Scan

Having successfully installed the two extra passes in the multi-pass amplifier, attention turned to determining the behaviour of the transient MRG spectrum with the strength of the nonlinear interaction. This had been studied in part by Sali et al (2005), where the evolution of the spectrum with pressure had been investigated, however the pressure not only affects the strength of the nonlinearity, but also changes the dispersion of the system. To study the growth of MRG independent of dispersion, we chose to vary the intensity of the pump pulses. In particular, we adjusted the energy by inserting a polarizer/waveplate attenuator in the beam, which could adjust the intensity without affecting the alignment, pulse duration, or focussing. The resulting scan is shown in Figure 4-10, where the total energy contained in the two pumps is shown in the corner (accounting for the pre-pulses), and the two arrows highlight the pumps at 382THz and 359THz.

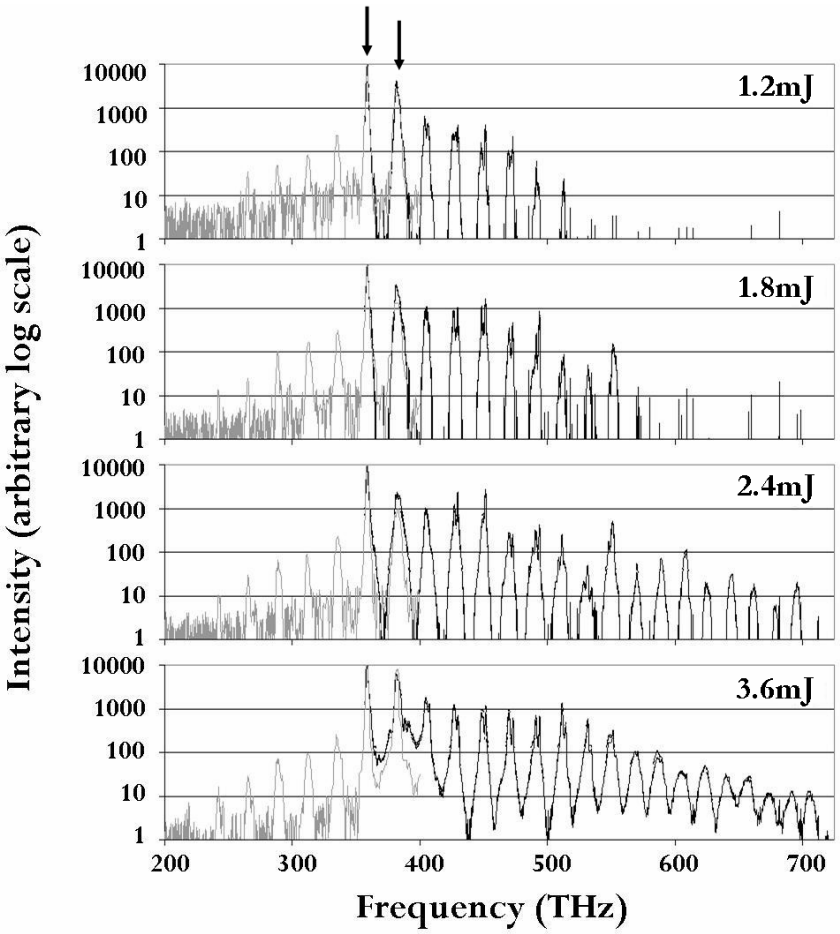

Figure 4-10: Variation of the generated bandwidth with total pulse energy. The Stokes orders obtained with the OSA are shown in grey, and the anti-Stokes orders obtained with the spectrometer are shown in black. The total energy in the two pulses are shown in the top right corner taking into account the pre-pulses.

It was in obtaining these spectra that the sensitivity of the pulse duration to the wavelengths of the pumps was first realized. Initially, the pump beams were set to be compressed at ~300fs each. However, it was discovered after the experiment that the long wavelength pump had inadvertently been stretched to twice the duration of the short wavelength when optimizing the various parameters of the experiment, resulting in durations of ~600fs and ~300fs respectively. However, this proved to be an asset as the onset of self-phase modulation was suppressed until the highest energy (an effect similar to that noted in Sali et al (2005) when they stretched on of their pumps), which allowed for the study of MRG in isolation from other nonlinear effects. The pressure in this experiment was set to its maximum of three atmospheres.

A number of features stood out in the course of this energy scan. First, as the energy in the pumps was increased, the higher-order anti-Stokes orders experienced significantly more growth than the higher-order Stokes. This preferential scattering into higher frequencies would be an important asset in producing short pulses, as the pulse duration is fundamentally limited by the wavelengths used to synthesize it.

Secondly, the anti-Stokes orders are observed to grow into the plateau-like structure observed in previous scans, but in this case eventually grew to become comparable to the short-wavelength pump intensity (as apparent in the 2.4mJ scan). The importance of this fact can be illustrated in the context of Fourier theory, where the parameters of frequency and time possess an inverse relationship with respect to each other. That is, narrow features in the frequency domain map to broad temporal features, and conversely a broad spectrum will map to a short optical burst, assuming of course that there is no phase dispersion. Intuitively then, a broad plateau feature in the generated spectrum is highly desirable, as it then has a greater potential to produce a short pulse than a rapidly diminishing spectrum. As well, that the plateau is forming on a scale comparable to the pump beams is also beneficial to the formation of short pulses, as it avoids the situation shown in Figure 4-11a. In this figure, the computer generated spectra on the left were Fourier-transformed using Matlab into the temporal pulses shown on the right. With a dominant narrow feature in a very broad spectrum, the short pulse is essentially a weak feature on top of a long and intense pulse (Figure 4-11a). When the plateau is within an order of magnitude of the peak however, it is the short pulse that is dominant over the broad background (Figure 4-11b).

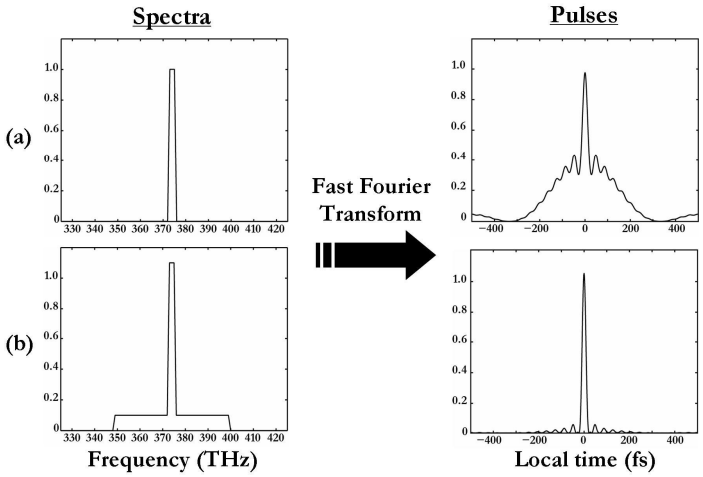

Figure 4-11: Fourier transform of a 3THz-broad peak on a 50THz base. (a) The base is one thousandth the intensity of the peak. (b) The base is one tenth the intensity of the peak.

The third feature of interest is that with the onset of self-phase modulation, the growth of the total bandwidth relative to the pump was found to cease, which is shown quantitatively in Figure 4-12. Displayed in the graph are the trends of the number of orders within one, two, and three orders of magnitude of the short-wavelength pump, where it is obvious upon inspection that SPM halts the growth of this bandwidth. The reasons for the halting of this growth may be twofold – the first being that SPM shifts some energy away from the Raman pumps into frequencies that are not resonant, thereby weakening the driving force on the molecules. This detrimental effect was also noted in Losev et al (2002b) where transient MRG had been attempted in a crystal. The second is that the radiation now in the wings of the pump can then scatter from the generated coherence, absorbing energy from the molecules and suppressing the scattering of the primary Raman orders.

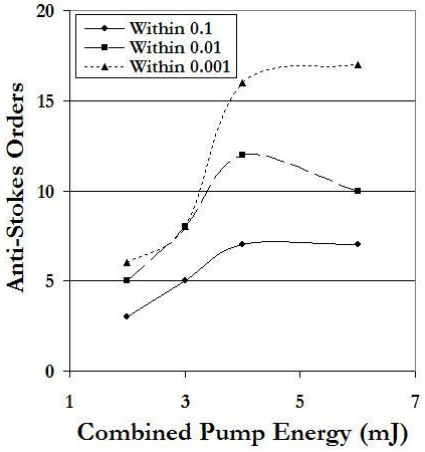

Figure 4-12: Number of anti-Stokes orders relative to the short-wavelength pump beam, as measured from Figure 4-10

The last interesting feature of this energy scan is the sudden regularity in the intensities of higher orders, where the large oscillations in the amplitude of the Raman orders (as observed in the 1.8mJ and 2.4mJ plots), are largely absent at 3.6mJ, where instead the peaks experience more of an exponential decay similar to the two spectra in Figure 4-8. By taking a fit from anti-Stokes orders 6 to 17, one arrives at an exponential form of $\sim e^{-1.79n}$, where again n stands for the index of the anti-Stokes orders. In all three cases where SPM and MRG coexist this exponential decay is present, which is contrary to the prediction that the orders should have oscillating Bessel-like amplitudes as observed in the 1.8mJ and 2.4mJ plots. That the three spectra yield exponents of -1.74n, -1.76n, and -1.79n for the higher anti-Stokes orders is a remarkable coincidence, given that the they were generated using three different sets of beam parameters on three different days. However, any discussion of this behaviour is likely to require the inclusion of self-phase modulation into a computer model, which has been reported in the case of impulsive MRG models [Kalosha 2003], but was beyond the scope of the model developed in this study.

4.6. Modelling Transient MRG

As described in **§2.3**, a computer model was written in Matlab to help us understand the behaviour observed in the intensity scan. This model used equations [Eq. 2-31] and [Eq. 2-32] to describe the nonlinear interaction of the pump beams, and was able to capture the essential physics involved as was demonstrated in Figure 2-3. Unfortunately, in trying to match the results shown in the figure, the resources available to the PC were completely maxed out and still fell slightly short of the published spectrum. As such, the more complicated case of short pump pulses was far too involved to get an acceptable convergence of the solution, however we felt that there is still some insight to be gained from this model considering the qualitative behaviour of transient MRG.

The major differences when modelling transient MRG as opposed to the plane-wave case are threefold. First, the frequency resolution was greatly enhanced, allowing the Regen spectrum to be read into the program and used for the simulation. Secondly, a convolution algorithm was added into the program to allow for the linewidth of the Raman transition. Finally, an arbitrary phase profile could be constructed for the pump beams, which could allow one to stretch the pulses, delay one with respect to the other, or apply third-order dispersion. In practice, only the increase in frequency resolution was actually used, as the

program required too many resources otherwise. Other parameters that could be adjusted in the program were the pressure, the diameter of the fibre, the length of the fibre, and the strength of the interaction, a parameter which includes all of the constants of [Eq. 2-31] and [Eq. 2-32], and which was left to be determined by trial and error.

The major insight drawn from this transient model is that if the bandwidth of the pumps are slightly mismatched, such that part of the spectrum of one pump does not have a resonant counter-part in the other, the oscillatory behaviour of the MRG spectrum becomes smoothed out. This is demonstrated in Figure 4-13, where two Gaussian pulses centred at 780nm and 830nm and with bandwidths of 5nm scatter from SF_6. It is assumed in the simulation that there is no dispersion, and that the Raman level is infinitely narrow. In part (a), the pulses are exactly on resonance, and the Bessel behaviour described in **§2.2.1** is apparent. In part (b) however, where the short-wavelength pump has been shifted to 775nm, the oscillations have been smoothed out. This behaviour is further illuminated in Figure 4-13c, where the colours from blue to red show increasing intensity. Notice the propagation of the 0^{th} order in particular, and observe that as it scatters into other Raman orders, the mismatched bandwidth from the Stokes pump (index of -1), scatters back into it, smoothing out the oscillation apparent in part (a).

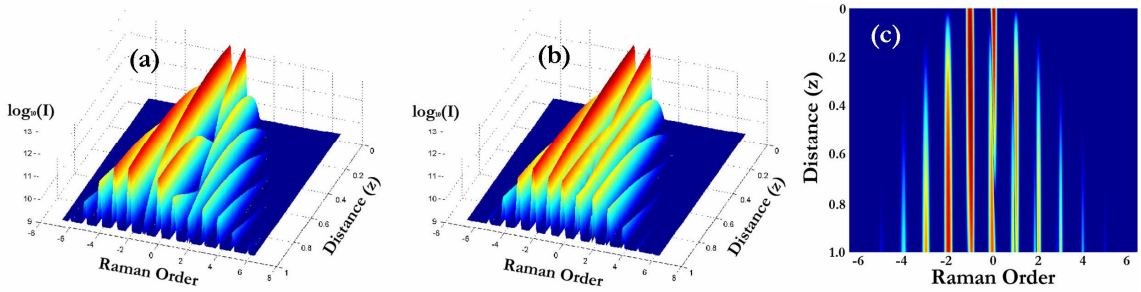

Figure 4-13: Modelling transient MRG with Gaussian pulses. (a) Pulses perfectly on resonance. (b) The pulses are detuned from the resonance by 5nm. (c) Top view of part (b)

This mismatched bandwidth could describe some of the structure observed in the Raman orders, such as the jagged peaks apparent in Figure 4-10. Figure 4-14 directly compares the results of the 1.2mJ scan with a simulation that used the Regen spectrum from that same data set. While the magnitude of the peaks do not correspond well, the structure is somewhat similar. To better match the data in the future, efforts are underway to develop a comprehensive nonlinear model on a more powerful computer, which will be designed to take SPM into account as well. The most recent form of the model is given in Appendix C.

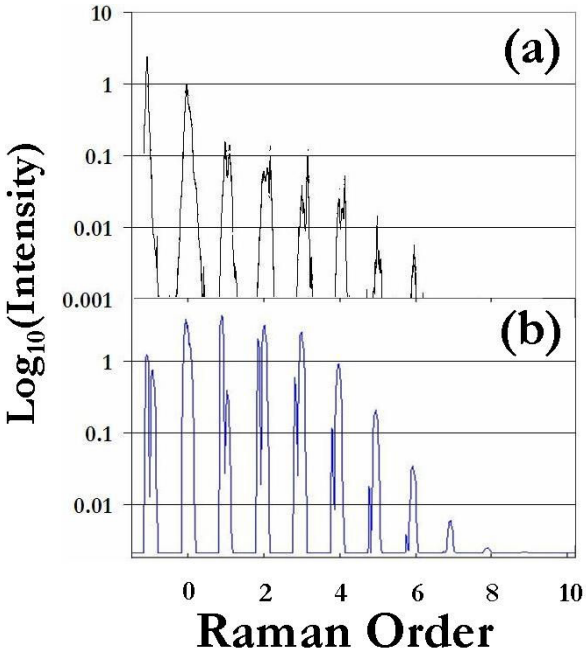

Figure 4-14: Comparison between experiment and computer model. (a) 1.2mJ scan in Figure 4-10. (b) Output of the model using the Regen Spectrum from that run.

4.7. Pressure and Dispersion

As discussed in **§3.5**, the balance between the negative dispersion of the fibre and the normal dispersion of the gas forms a dispersion null that moves to higher frequencies as the fibre diameter is decreased. This effect was utilized in impulsive pump-probe MRG to match the group velocities of the 800nm pump and a 400nm probe, which resulted in a significant enhancement of the generated bandwidth [Nazarkin 2002b]. This null could not reach our pump frequencies in the 250μm fibre within the 1 to 3atm pressure range afforded by the apparatus, but by switching to a hollow fibre with a diameter of 129μm, it would reach these frequencies at a pressure of about 2atm, right in the middle of the pressure range available to us. If dispersion were to have an effect on the generated spectrum we should be presumably be able to observe it.

The dispersion of the hollow fibre can be determined by considering the total wavevector γ as described in Marcatili & Schmeltzer (1964), along with the dispersion discussion in Chapter 9 of Siegman (1986). In terms of the normal wavevector $\boldsymbol{k}$ in SF_6, the total wavevector is given by

$$\gamma \approx \boldsymbol{k}\left[1-\frac{1}{2}\left(\frac{\boldsymbol{u}_{nm}\lambda}{2\pi\boldsymbol{a}}\right)^2\left(1-\frac{i\boldsymbol{\nu}_n\lambda}{\pi\boldsymbol{a}}\right)\right] \qquad \textbf{[Eq. 4-1]}$$

In the equation, u_{nm} is the m^{th} root of the ordinary Bessel function of order $n-1$ (since the hollow fibre contains the beams in its fundamental hybrid mode, n and m will both equal 1), a is the inner radius of the hollow fibre, λ is the wavelength of the light, and ν_n is an effective index of refraction of the guiding material (in this case fused silica), which is given in terms of its normal index of refraction ν by

$$\nu_n = \frac{\left(\nu^2 + 1\right)}{2\sqrt{\nu^2 - 1}} \qquad \textbf{[Eq. 4-2]}$$

Note that γ is a complex-valued function, where its real part describes the dispersion and its imaginary part gives the fibre attenuation. The n^{th} order dispersion is then determined by taking the n^{th} order derivative of the real part of γ with respect to frequency – the effects of various orders of the dispersion are illustrated in Figure 3-3.

If the dispersion was to have an effect on the generated MRG spectrum, it should be readily observed by comparing the effect of intensity and pressure, as they should both equally affect the strength of the nonlinearity in the absence of dispersion. The first experiment was therefore to compare what happens when the energy was reduced by half relative to when the pressure was halved. In keeping with our findings in the intensity scan, we avoided self-phase modulation on the pumps by stretching the 383THz and 360THz pulses to approximately 550fs. The energy was balanced between the two beams, but was considerably lower than obtained earlier, where each pulse contained an energy of ~0.4mJ. I chose not to maximize the energy, as this was the first experiment with the smaller fibre and I wanted to avoid damaging it as much as possible. However, even without our maximum energy the results of were spectacular – as can be observed in Figure 4-15, a significant difference between halving the pressure versus halving the energy was observed even on a logarithmic scale. By halving the pressure from three atmospheres to one and a half, the intensity of the generated spectrum experiences a huge enhancement in the higher anti-Stokes orders, which is opposite to what would be expected if the dispersion did not affect the spectrum.

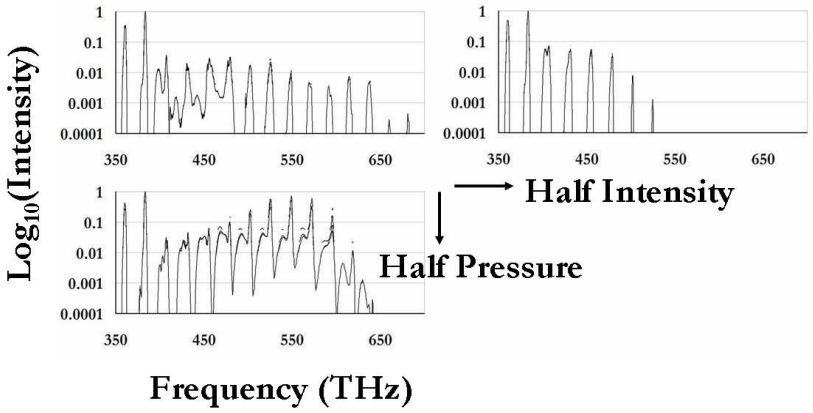

Figure 4-15: Demonstration of how dispersion affects transient MRG.

To further investigate the effect of dispersion and the occurrence of the complex structure on the peaks, a detailed pressure scan was conducted, where just like in **§4.3**, the pressure was reduced in increments of 5psi (with an extra scan at 1atm + 7.5psi from Figure 4-15). The dramatic results of this scan are compiled in Figure 4-16, where the spectra as a function of pressure is plotted on a linear scale. While the initial MRG spectrum at three atmospheres was modest compared to earlier results, as the pressure was decreased down to one atmosphere a number of orders grow to become comparable to the pump beams – even surpassing the transmitted long-wavelength pump beam in intensity! This enhancement was not observed when the 250μm fibre was used (see the pressure scan of Figure 4-7), again highlighting the importance of the dispersion in the smaller fibre.

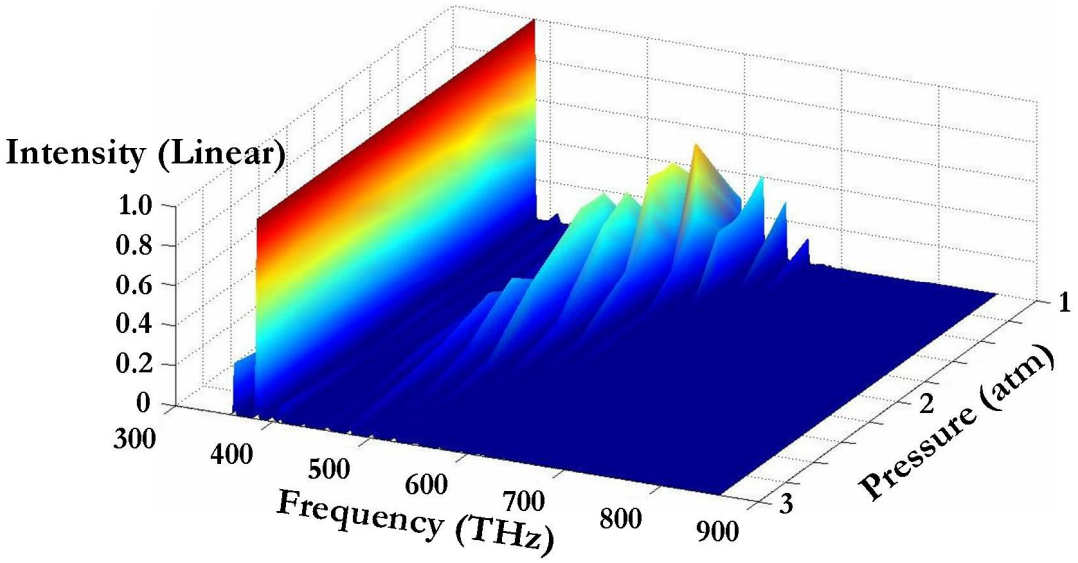

Figure 4-16: Dependence of the spectra with pressure on a linear scale. The pressure scale is decreasing into the page.

Further details can be observed in Figure 4-17, where the individual spectra from this same scan are plotted on a logarithmic scale. It is interesting that the spectrum at first retreats as the pressure is reduced, but then around two atmospheres becomes successively broader, with intensities that are far enhanced compared with the original 3atm case and with orders that grow a broad red-shifted shoulder. One might attribute these shoulders to self-phase modulation, however contrary to what one would expect this broadening is largely absent at both the highest pressure and on the more intense pump beams. Finally, the manner in which the orders broaden – into a red-shifted shoulder with a number of peaks – is inconsistent with the normal idea of SPM, where the broadening depends on the derivative of the intensity and as such should generate both a red-shifted and blue-shifted wing due to the leading and trailing edge of the pulse respectively. That is, they are inconsistent with the idea of SPM from a symmetric pulse, but could potentially be explained by the formation of a pulse that has a sharp front edge and a gentle trailing tail.

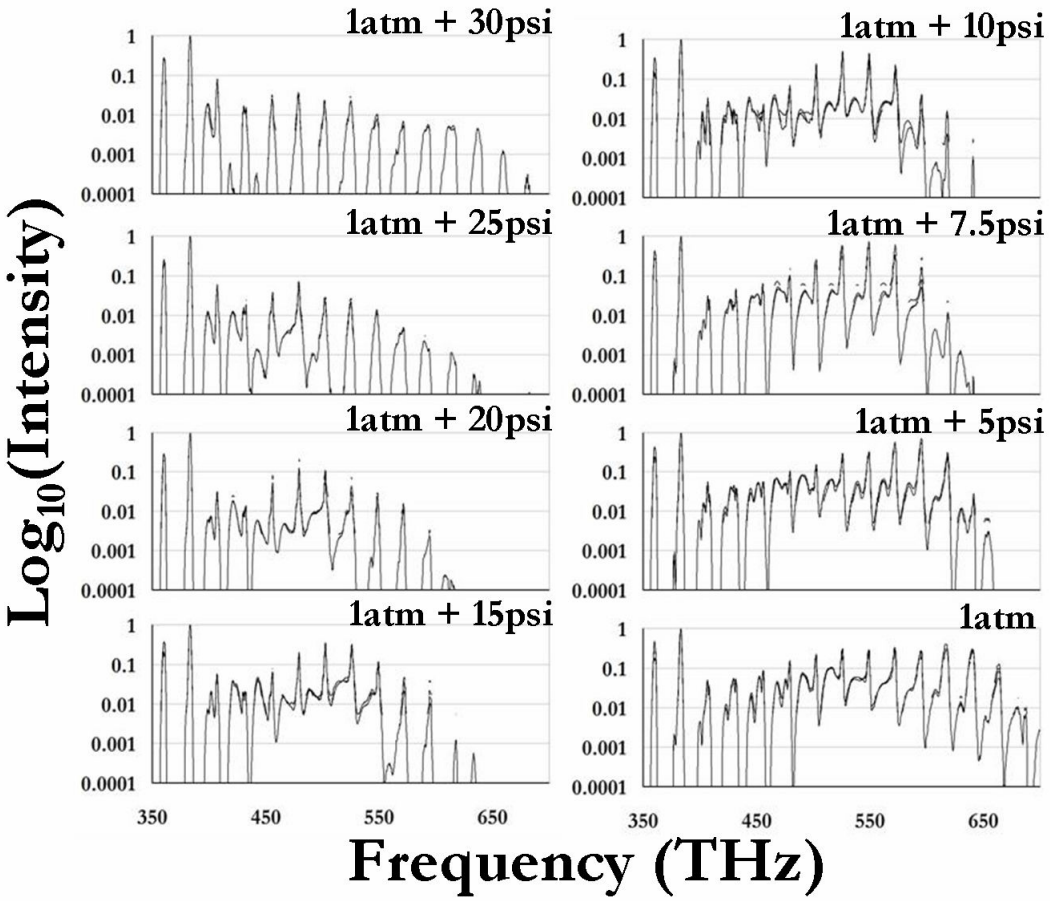

Figure 4-17: The dependence of the generated spectrum with pressure on a logarithmic scale, where the pressure for each spectrum is given in the top right-hand corner.

To get a sense of the dispersion we chose to consider the group delay, which was used in **§3.5** to get a sense of the dispersion characteristics of a hollow fibre. Again, it is a measure of the delay one frequency experiences relative to another, and is inversely related to the group velocity. Plotted in Figure 4-18 is a reproduction of Figure 4-17 overlaid with the group delay, which is taken relative to the minimum group delay in the frequency range of the plots. The only clear correlation between the spectrum and the group delay is that the enhancement lies within a range where the group delay is less than 40fs/m. Put another way, given that the fibre is about one metre long, the broadened and enhanced Raman orders are only evident when they have been delayed with respect to one another by less than a vibrational period, which is 43fs for the A_{1g} vibration of SF_6. It is likely that the enhanced bandwidth is simply due to the fact that the orders do not walk off the pump beams as much during their propagation. This however would not explain the complex red-shifted shoulders on the Raman orders themselves.

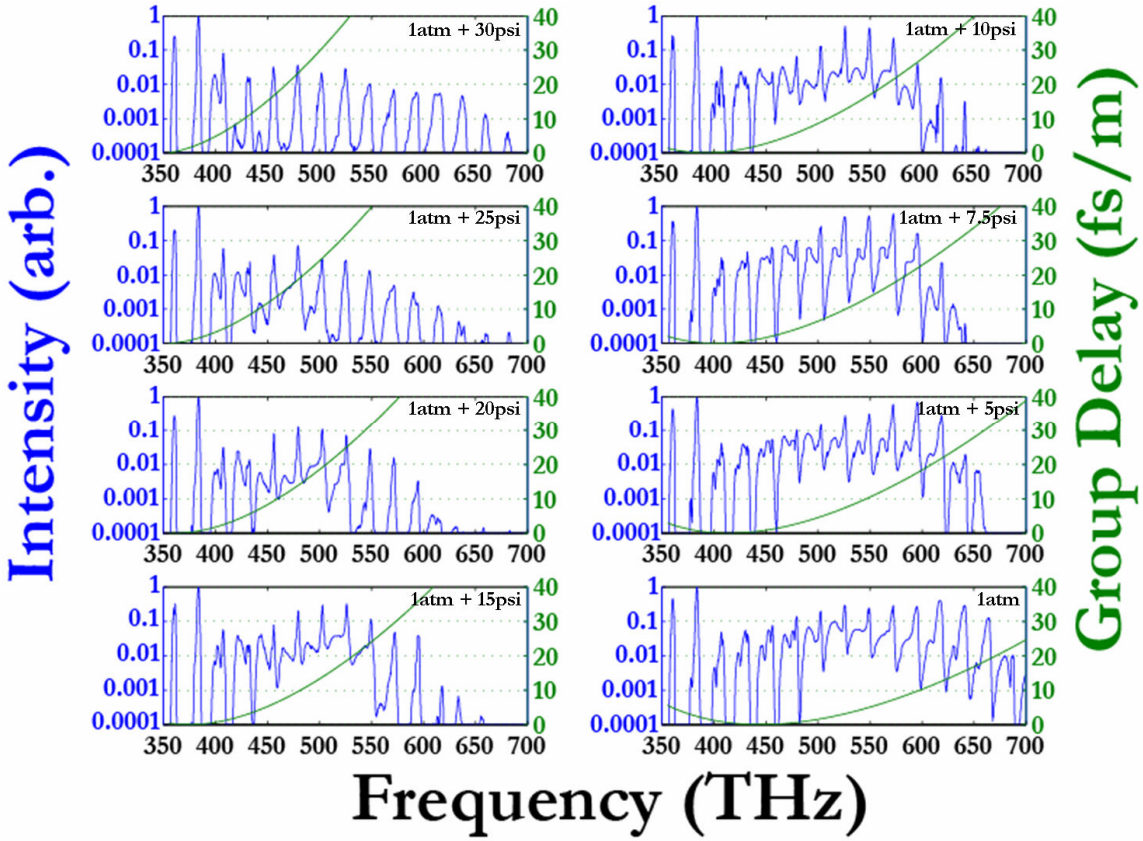

Figure 4-18: A reproduction of Figure 4-17 overlaid with a plot of the group delay relative to the short-wavelength pump.

The first attempt to explain this red-shifted and multi-peaked shoulder was the idea that other vibrational levels had been accessed, which due to the anharmonicity of the molecular potential may lead to peaks that are red-shifted. However, the data in Herzberg (1945) states that the anharmonicity of SF_6 is only two wavenumbers, corresponding to a frequency of 0.06THz. This would not be observable on the scale in Figure 4-17, and cannot account for the 12THz shift that is observed in some of the peaks.

One other feature that was noticed during the experiment was that the peaks would jitter around, as if shifting in response to fluctuations in the laser intensity. Upon re-examination of the spectra, a subset that were taken at three atmospheres but with different energies were placed together to check the position of the side peaks (Figure 4-19). Note the shifting of the peaks relative to their Raman orders as the intensity changes, which is highlighted in the first order by the line drawn down the plot.

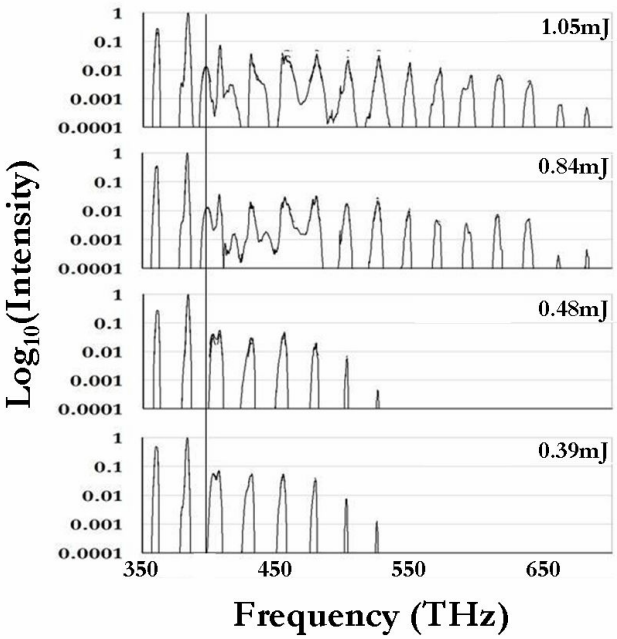

Figure 4-19: Series of spectra taken at three atmospheres. Note the shifting of the side peaks with a change in intensity.

The consistent downshift experienced by these orders is reminiscent of an effect predicted by McDonald (1995). In this paper he predicts that transient MRG should (with no dispersion), spontaneously generate solitons – stationary solutions of the electric field where the pulses do not change their temporal shape. These solitons are distinct form the multifrequency solitons predicted for the steady-state regime, as each Raman order should break into a train of solitons travelling at different group velocities, as opposed to all of the

orders becoming locked into a single train. The red-shifted peaks provide a hint that this may be the case, as solitons in general experience a shift to lower frequencies [Gordon 1986]. While this frequency shift is not strictly intensity-dependent as observed in the experiment, it does depend on the soliton pulse duration, which may in some way depend on the strength of the MRG interaction. As well, while it has been shown that typical two-colour Raman solitons are unstable with positive dispersion, the solitons predicted by McDonald (1995) were described as being robust to phase dispersion and other complicating factors, and indeed it was said that the nonlinear dynamics of transient MRG were strongly attracted to this solution.

The final attempt at understanding the complex broadening of the orders was to map the positions of the side peaks to the pressure, to see if there was a noticeable trend. This was done by subjectively deciding where the peaks lay in the spectrum given their proximity to one another. That is, if there was a single broad shoulder that had a flat top, it was assumed that it consisted of two peaks, where because of their jittering during the average they blended into one another. The peaks on the first few orders seemed to be relatively stable in their position, and it was thought that the other peaks might also be shifted by a definite amount. Their behaviour turned out to be more complicated than expected as shown in Figure 4-20, and no clear pattern has yet been established. The primary Raman orders are highlighted with arrows, and the way the peaks seemed to meld into and away from each other as the pressure is changed is depicted by the curved lines drawn on the plot.

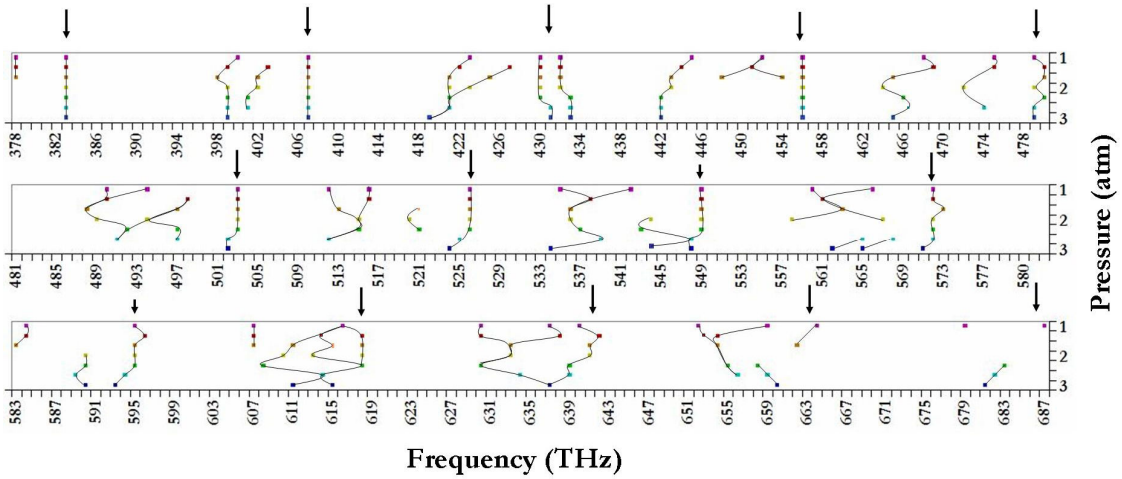

Figure 4-20: Mapping of the position of the peaks with pressure. The arrows show the primary Raman orders, and the pressure is on a scale that decreases as it goes up the page.

5. Concluding Comments

It was the main goal of this research to determine the potential of this laser system for producing few-cycle pulses. In the absence of an experimental demonstration, this potential can be investigated using a numeric fast Fourier transform (FFT), which converts a discrete intensity spectrum into a temporal profile. The choice of which spectra to use was determined by considering how we expected to compress the resulting radiation. To maintain high energies, and to avoid purchasing expensive optical devices such as a liquid-crystal phase modulator, we opted to consider the compression setup described in Sokolov et al (2001), where a series of prisms and delay lines were used to time up individual orders. As such, only the truly discrete spectra – not those exhibiting strong SPM – were Fourier transformed, even though the ones with SPM might give a more isolated pulse. These Fourier transforms are given in Figure 5-1. In part (a), the 2.4mJ spectrum from the intensity scan is Fourier transformed, yielding a central pulse with a duration of 3.2 fs and an estimated energy of 120μJ. Part (b) gives the Fourier transform of the pump-probe spectrum of Figure 4-6, which results in a central pulse that has a duration of 3.3fs and an estimated energy of 14μJ. If these pulse energies could be obtained, they would be an order of magnitude more energetic than comparable pulses generated using other techniques, such as the 25μJ, 3.8fs pulse synthesized using continuum generation [Steinmeyer 2006], and the 1.5μJ, 3.8fs pulsed synthesized using impulsive pump-probe MRG [Zhavoronkov 2002].

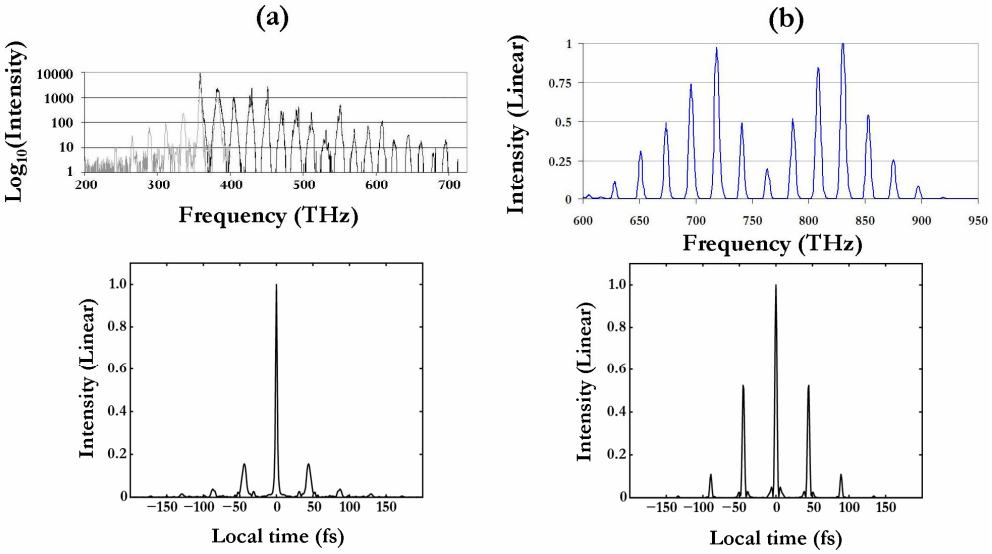

Figure 5-1: Fast Fourier Transforms. (a) The 2.4mJ MRG spectrum of Figure 4-10 and its FFT. (b) The pump-probe spectrum of Figure 4-6 and its FFT.

Along with the exhibiting the potential of transient MRG to generate high-energy few-cycle pulses, this study has also discovered very exciting behaviours when examining the generation in a system of low dispersion – behaviours that have not yet been reported in the literature. The peculiar enhancement with decreasing pressure is likely to have implications in how to optimize the apparatus to generate the largest bandwidth, and therefore synthesize the shortest pulse. As well, regardless of whether the Raman orders are generating solitons, there is sure to be some interesting physics to be discovered in the low-dispersion regime.

From this vantage, there are a number of direction which we intend to follow. First and foremost we intend on further examining the behaviour of transient MRG in the small-diameter fibre, with further experiments and the development of a comprehensive nonlinear computer model. As well, we have been developing a system similar to that described in Sokolov et al (2001), where we will use a system of prisms and delay lines to compress the pulses, and use the ionization signal of a noble gas in a time-of-flight chamber to measure the pulse duration. Another potential study is testing the growth of the MRG bandwidth with the propagation distance, by using a number of shorter hollow fibres. In the experiment it was consistently noticed that significant Raman generation was occurring within the first few centimetres of propagation, as the small amount of light that leaked out of the fibre looked as white as the output beam. With the realization of that experiment, we can investigate the growth of MRG independent of both dispersion and the other nonlinear effects such as self-phase modulation, and compare that to both an energy and pressure study.

With the experience gained throughout this study and the many areas of research that are now left open to us, the study of transient multifrequency Raman generation is sure to continue to have a rich future at the University of Waterloo.

Appendix A: Modelling the Regenerative Amplifier

While the core of this research is presented in sections one through five, as is usually the case there was a significant amount of supplemental work required for the development of this study. To outline the details for future reference, it has been organized into a series of appendices, where appendices A and B focus on the practical parts of daily lab work, including how to model, build, and align optical systems, and appendix C contains a transcript of the final computer code used in the simulations.

This appendix will primarily deal with modelling physical optical systems, with particular attention to designing a regenerative amplifier. Much of this discussion will be in reference to two particular textbooks: Anthony E. Siegmans *Lasers*, and Orazio Sveltos *Principles of Lasers* [Siegman 1986; Svelto 1998]. However, a slightly modified notation is used for the sake of clarity.

The effort to model the Regen began after the regular occurrence of damage on the crystal, and occasionally one of the back mirrors. The first thing to be determined was whether changing the focal length of one of the curved mirrors from 50cm to 100cm might solve the problem, keeping in mind that damage to the Pockels Cell must be avoided at all cost. The effect of other parameters was to be studied as well, to determine if there might be a more suitable design. In the end, it was decided that switching the mirror was not practical, but that along with some minor adjustments to various lengths in the cavity, the problem should be solved simply by moving the crystal further from the focus of the cavity mode.

A.1 ABCD Matrices

One of the formalisms used to describe the propagation of light is that of *ABCD* or *Ray* Matrices. As the name implies, it uses a geometrical description of light rays in the form of a matrix to model the action of an optical element on a wavefront. It begins by considering the propagation of a ray of light through a general optical element such as in Figure A-1. The incident ray is labelled $\vec{r}_1$ and the ray transmitted ray is labelled $\vec{r}_2$. The ABCD matrix for this optical element describes the effect of that element on the distance (d), and direction $\left(\frac{\partial d}{\partial z}\right)$ of the ray relative to the optical axis. In general, it is assumed that there is a

linear relation between the distances and directions of the input and output rays. These linear relations are given by

$$\begin{aligned} d_2 &= A \cdot d_1 + B \cdot d_1' \\ d_2' &= C \cdot d_1 + D \cdot d_1' \end{aligned} \qquad \textbf{[Eq. A-1]}$$

where $d' = \partial d / \partial z$. These equations can be then be rewritten as

$$\vec{r}_2 = \begin{pmatrix} d_2 \\ d_2' \end{pmatrix} = \begin{pmatrix} A & B \\ C & D \end{pmatrix} \cdot \begin{pmatrix} d_1 \\ d_1' \end{pmatrix} = M \cdot \vec{r}_1 \qquad \textbf{[Eq. A-2]}$$

where M is the ABCD matrix of the element. An important property of these matrices is that in free space, the behaviour of the optical element should simply be reversed when sending the beam back through the other direction, thus the determinant of the matrix $AD - BC$ is equal to 1 (with two separate materials on either side of the element, the determinant is equal to the ratio of their indices of refraction).

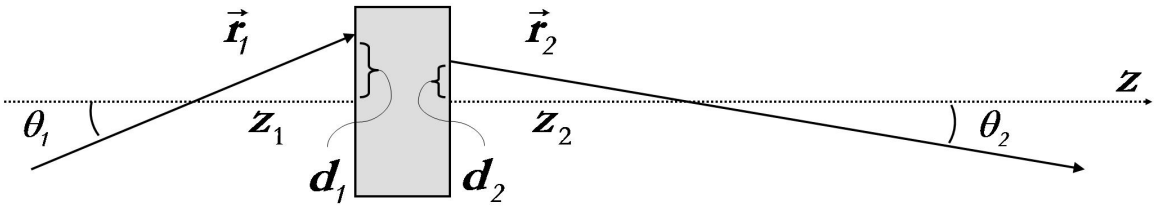

Figure A-1: Action of a general optical element on a ray of light

The particular choice of using d and d' to describe the vector $\vec{r}$ is not arbitrary. A key attribute of an optical wavefront is the radius of curvature R, which in the paraxial approximation can be written as $R = d/d'$. In the case of a spherical wave the radius of curvature can completely describe its propagation, and as such it is useful to consider the change in R as a wave propagates through an optical element. Assuming a wave of with a radius of curvature $R_1 = d_1/d_1'$, the new radius after propagation through a general optical element is found to be

$$R_2 = \frac{A \cdot R_1 + B}{C \cdot R_1 + D} \qquad \textbf{[Eq. A-3]}$$

. As an example of how to construct one of these ray matrices, consider the passage of a ray of light starting in vacuum and going through a dielectric block of length L and index of refraction n (Figure A-2). By Snell's Law,

$$\begin{aligned} &\sin(\theta_1) = \boldsymbol{n} \cdot \sin(\theta_n) \\ &\boldsymbol{n} \cdot \sin(\theta_n) = \sin(\theta_2) \\ &\therefore \sin(\theta_1) = \sin(\theta_2) \end{aligned} \qquad \textbf{[Eq. A-4]}$$

Now in the paraxial approximation,

$$\sin(\theta) \approx \tan(\theta) = \frac{\boldsymbol{d}}{\boldsymbol{z}} \qquad \textbf{[Eq. A-5]}$$

so $\boldsymbol{d'} = \partial \boldsymbol{d} / \partial \boldsymbol{z} \approx \sin(\theta)$. This leads to the expression

$$\boldsymbol{d}_1' = \left(\boldsymbol{n} \cdot \boldsymbol{d}_n'\right) = \boldsymbol{d}_2' \qquad \textbf{[Eq. A-6]}$$

which implies that $\boldsymbol{C} = 0$ and $\boldsymbol{D} = 1$. Furthermore, the new distance $\boldsymbol{d}_2$ is found to be

$$\begin{aligned} \boldsymbol{d}_2 &= \boldsymbol{d}_1 + \tan(\theta_n) \cdot \boldsymbol{L} \\ &= \boldsymbol{d}_1 + \boldsymbol{d}_n' \cdot \boldsymbol{L} \\ &= \boldsymbol{d}_1 + \boldsymbol{d}_1' \cdot \boldsymbol{L} / \boldsymbol{n} \end{aligned} \qquad \textbf{[Eq. A-7]}$$

implying that $\boldsymbol{A} = 1$ and $\boldsymbol{B} = \boldsymbol{L} / \boldsymbol{n}$. These equations therefore lead to the ABCD matrix

$$\boldsymbol{M}_{\boldsymbol{Block}} = \begin{pmatrix} 1 & \boldsymbol{L} / \boldsymbol{n} \\ 0 & 1 \end{pmatrix} \qquad \textbf{[Eq. A-8]}$$

The ray matrices for a variety of optical elements have been tabulated in Siegman, chapter 15 page 585.

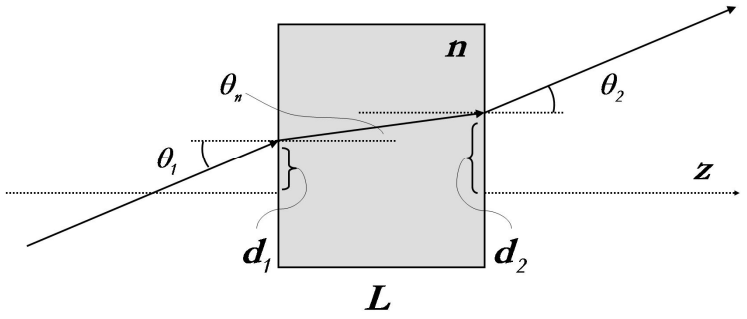

Figure A-2: Ray of light going through a dielectric block from vacuum

For complex systems, the overall ray matrix is the left product of the ray matrix for each individual element, in the order that the elements are reached. Taking the system in Figure A-3 as an example, the total ray matrix describing this system would be the product (from right to left), of the ray matrix of the lens, that for propagation through free space, and that of a tilted curved mirror. The resulting propagation equation would be

$$\begin{pmatrix} \boldsymbol{r}_2 \\ \boldsymbol{\theta}_2 \end{pmatrix} = \boldsymbol{M}_{\boldsymbol{tilt}} \cdot \boldsymbol{M}_{\boldsymbol{space}} \cdot \boldsymbol{M}_{\boldsymbol{lens}} \cdot \begin{pmatrix} \boldsymbol{r}_1 \\ \boldsymbol{\theta}_1 \end{pmatrix} \qquad \textbf{[Eq. A-9]}$$

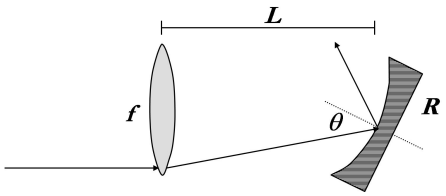

Figure A-3: Propagation through multiple optical elements

A.2 Gaussian Beams

While these ray matrices can completely describe the propagation of a spherical wavefront, in the laboratory one typically uses a laser beam, which has a Gaussian profile instead of a spherical one. Fortunately, Gaussian beams can be treated in a way that is exactly analogous to that of spherical waves. To help motivate the discussion, consider first the mathematical representation of a paraxial spherical wave propagating in the z-direction. By saying the wave is paraxial, it is assumed that we are considering only those points in space where the distance ρ from a source at the origin can be written as

$$\rho \approx z + \frac{x^2 + y^2}{2z} \qquad \textbf{[Eq. A-8]}$$

which in turn allows one to write the electric field as

$$\tilde{E}(\rho,t) = \frac{e^{-i(k\rho-\omega t)}}{\rho} + c.c. \approx E(z)\cdot e^{-ik\left(\frac{x^2+y^2}{2R}\right)}\cdot e^{-i(kz-\omega t)} + c.c. \qquad \textbf{[Eq. A-9]}$$

In this approximation, the radius of curvature is approximately equal to z (instead of as a function of $\mathbf{x}$, $\mathbf{y}$, and z). Taken literally, this form of the electric field is infinite in extent along the x and y directions, which is not physically realistic (starlight being the only possible exception). A Gaussian beam is modified by having a finite beam waist w in the directions transverse to that of propagation, such that the electric field can be described as

$$\tilde{E}(x,y,z,t) = E(z)e^{-\left(\frac{x^2+y^2}{w^2}\right)}e^{-ik\left(\frac{x^2+y^2}{2R}\right)}e^{-i(kz-\omega t)} + c.c. \qquad \textbf{[Eq. A-10]}$$

Note how the new exponential factor is real-valued. Bringing this into the transverse phase factor, one can define a new complex radius of curvature q to put the equation in the form

$$\tilde{E}(x,y,z,t) = E(z)e^{-ik\left(\frac{x^2+y^2}{2q}\right)}e^{-i(kz-\omega t)} + c.c. \qquad \textbf{[Eq. A-11]}$$

where $\mathbf{q}$ is found to be

$$\frac{1}{2q} = \frac{1}{2R} - \frac{i}{kw^2} \qquad \textbf{[Eq. A-12]}$$

The resulting expression [Eq. A-11] looks exactly like that of a spherical wave [Eq. A-9] with $\boldsymbol{R}$ replaced by $\boldsymbol{q}$. A Gaussian beam can then be modelled using ray matrices in exactly the same fashion as a spherical wave by replacing $\boldsymbol{R}$ with $\boldsymbol{q}$ everywhere in [Eq. A-3].

A number of insights can be found by considering the propagation of a Gaussian beam using ray matrices. Consider for example an initially collimated beam, such that the radius of curvature is infinite and it has an initial size $\boldsymbol{w}_0$ as in Figure A-4. In this case

$$\frac{1}{\boldsymbol{q}_0} = -\frac{\boldsymbol{i}\lambda}{\pi \boldsymbol{w}_0^2} \qquad \textbf{[Eq. A-13]}$$

(note that $\boldsymbol{k}$ has been replaced by its free-space value $2\pi/\lambda$). Rearranging [Eq. A-3], one can find the new $\boldsymbol{q}$ after propagating a distance $\boldsymbol{z}$ as

$$\frac{1}{\boldsymbol{q}_z} = \frac{\boldsymbol{C} + \boldsymbol{D}/\boldsymbol{q}_0}{\boldsymbol{A} + \boldsymbol{B}/\boldsymbol{q}_0} \qquad \textbf{[Eq. A-14]}$$

where

$$\begin{pmatrix} \boldsymbol{A} & \boldsymbol{B} \\ \boldsymbol{C} & \boldsymbol{D} \end{pmatrix} = \begin{pmatrix} 1 & \boldsymbol{z} \\ 0 & 1 \end{pmatrix} \qquad \textbf{[Eq. A-15]}$$

is the ray matrix for propagating in free space. With some manipulation, one can find expressions for the new beam waist and radius of curvature

$$\boldsymbol{w} = \boldsymbol{w}_0 \sqrt{1 + \left(\frac{\lambda \boldsymbol{z}}{\pi \boldsymbol{w}_0^2} \right)^2}; \quad \boldsymbol{R} = \boldsymbol{z} \cdot \left(1 + \frac{\pi^2 \boldsymbol{w}_0^4}{\lambda^2 \boldsymbol{z}^2} \right) \qquad \textbf{[Eq. A-16]}$$

As is demonstrated in Figure A-4, this implies that a Gaussian beam cannot maintain a particular finite beam waist indefinitely. This leads to the idea of the Rayleigh range, which is the length that it takes an initially collimated beam of initial $\boldsymbol{w}_0$ to expand to a size of $\sqrt{2} \cdot \boldsymbol{w}_0$, which is $\boldsymbol{z}_{\boldsymbol{R}} = \pi \boldsymbol{w}_0^2 / \lambda$. This is standard measure of how long a beam will remain collimated. As an example, a typical beam in our laboratory will be 1cm in diameter with a wavelength of 800nm, and so will remain collimated for approximately 100 metres.

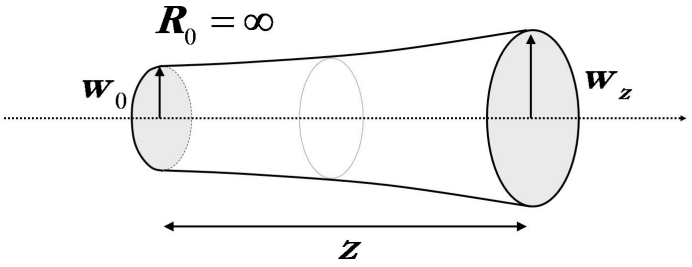

Figure A-4: Propagation of a Gaussian beam through a distance z in free space.

Another derivation that is particularly useful is the spot size of a Gaussian beam after going through a thin lens. Assuming a collimated beam, the beam would first go through a lens and then propagate a distance z through free space, such that the overall ray matrix would be

$$M_{total} = M_{space} \cdot M_{lens} = \begin{pmatrix} 1 & z \\ 0 & 1 \end{pmatrix} \cdot \begin{pmatrix} 1 & 0 \\ -1/f & 1 \end{pmatrix} = \begin{pmatrix} 1 - z/f & z \\ -1/f & 1 \end{pmatrix} \qquad \textbf{[Eq. A-17]}$$

leading to a complex radius of curvature

$$\frac{1}{q} = \frac{-1/f - i\lambda/\pi w_0^2}{1 - z/f - i\lambda z/\pi w_0^2} \qquad \textbf{[Eq. A-18]}$$

To find where the beam is focussed, we set the real part equal to zero, giving

$$z = \frac{\pi^2 w_0^4 f}{\lambda^2 f^2 + \pi^2 w_0^4} \qquad \textbf{[Eq. A-19]}$$

In the usual case where $\lambda f << \pi w_0^2$, this turns out to be the focal length f as expected.. Plugging in $z = f$ into the imaginary part of $1/q$ we can find the beam waist* after focussing with a lens

$$w \cong \frac{\lambda f}{\pi w_0} \qquad \textbf{[Eq. A-20]}$$

A.3 Modelling a Laser Cavity

When modelling the Regen cavity, it is to ones advantage that the lowest order transverse mode of a cavity mode is that of a Gaussian distribution. While higher-order transverse

* **Note that this equation and many others found in the literature assumes that the beam waist is defined as the radius at which the *field* has dropped to $1/e$ of its maximum value.** I don't know how many times I've mucked up an intensity calculation by using the statistical Gaussian distribution $e^{-r^2/2w^2}$, or had forgotten to switch the beam waist from the waist of the field to that of the intensity (which is the field squared, yielding a new beam waist which is $\sqrt{2}$ smaller than the field waist).

modes can be generated due to damage or obstacles in the cavity, it is usually only the TE_{00} that is excited. As such, it becomes convenient to model the cavity by using simple ray matrices, with a few rules governing the propagation of the beam as it oscillates in the cavity.

The most important of these rules is that, to be a stable cavity mode, the wavefront must be self-consistent. That is, it must repeat itself after a full round trip so that

$$\frac{1}{q_{final}} = \frac{1}{q_{initial}} = \frac{C + D/q_{initial}}{A + B/q_{initial}} \qquad \textbf{[Eq. A-21]}$$

where the ABCD matrix is formed by the left product of the individual ray matrices as the wavefront traverses the cavity. The model used to determine the round-trip ray matrix (shown in Figure A-5(b)), is a simplified version of the actual Regen shown schematically in Figure A-5(a). The changes are as follows:

1. For the purposes of the model, the Pockels Cell, crystal, and prisms only affect the optical path length the light has to go through, so these have been absorbed into the lengths L_1, L_2, and L_3.
2. The curved mirrors are modelled as lenses, where $f = R_{Mirror}/2$. Astigmatism is considered by modelling the modes in the both the sagittal and tangential directions (see the ray matrices in Siegman (1986)).
3. The extra positions of z_1, z_2, and z_3 are added to help determine the cavity mode at any point within the cavity.

The round-trip ABCD matrix is then found by following the path depicted in Figure A-5(b):

$$\begin{aligned} M_{Round-Trip} = {} & M_{Mirror1} \cdot M_{L1} \cdot M_{Lens1} \cdot M_{L2} \cdot M_{Lens2} \cdot M_{L3} \cdot M_{Mirror2} \\ & \cdot M_{L3-Z3} \cdot M_{Z3} \cdot M_{Lens2} \cdot M_{L2-Z2} \cdot M_{Z2} \cdot M_{Lens1} \cdot M_{L1-Z1} \cdot M_{Z1} \end{aligned} \qquad \textbf{[Eq. A-22]}$$

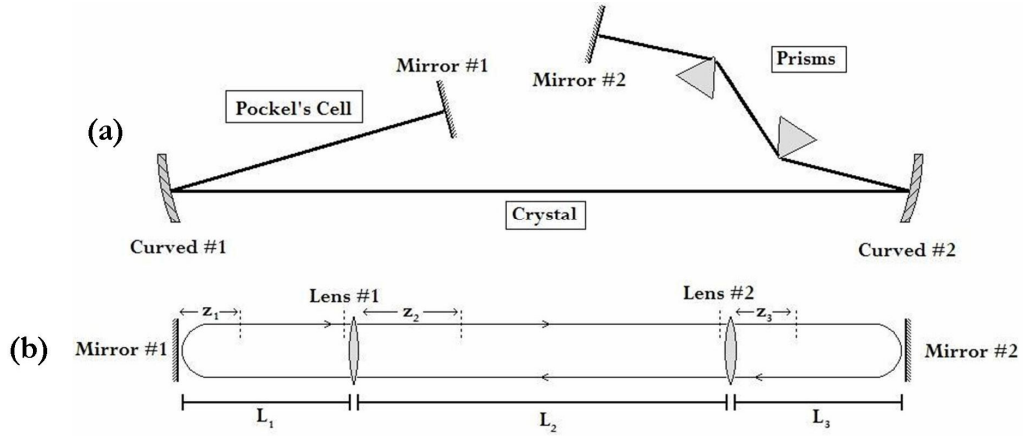

Figure A-5: Modelling the Regen. (a) Schematic of the Regen. (b) Simplified model.

The elements in the round-trip ray matrix can then be used to generate the self-consistent solution. Eq. A-21 can be rearranged to form

$$\frac{\boldsymbol{A}}{\boldsymbol{q}} + \frac{\boldsymbol{B}}{\boldsymbol{q}^2} = \boldsymbol{C} + \frac{\boldsymbol{D}}{\boldsymbol{q}} \qquad \textbf{[Eq. A-23]}$$

where the subscripts have been dropped. By using the fact that the determinant $det(\boldsymbol{M}) = \boldsymbol{AD} - \boldsymbol{BC} = 1$ when an optical element is in free space, one can obtain the solution

$$\frac{1}{\boldsymbol{q}} = \frac{\boldsymbol{D} - \boldsymbol{A}}{2\boldsymbol{B}} \pm \frac{\boldsymbol{i}}{\boldsymbol{B}} \sqrt{1 - \left(\frac{\boldsymbol{A} + \boldsymbol{D}}{2} \right)^2} \qquad \textbf{[Eq. A-24]}$$

Now for this solution to be realistic, it must follow two other criteria. Firstly, it must be a confined solution, such that is has a finite beam waist. This implies the solution must have a negative imaginary component as $Im\left(\boldsymbol{q}^{-1}\right) = -\lambda / \pi \boldsymbol{w}^2$. The condition can be quantified by inspection of the solution [Eq. A-24]. If all the matrix elements are real, the condition that the mode be confined simply requires

$$\left(\frac{\boldsymbol{A} + \boldsymbol{D}}{2} \right)^2 = \boldsymbol{m}^2 < 1 \qquad \textbf{[Eq. A-25]}$$

and that one choose the appropriate solution for $1/\boldsymbol{q}$. While in general the matrix elements can be complex-valued, in practice they are not unless one includes the radially decreasing gain in the Ti:Sapphire crystal. This acts to stabilize the cavity mode – permitting lasing even if the cavity is geometrically unstable. This effect is neglected in the final calculations as it makes them unnecessarily complicated, plus a test of the program with and without this effect could not determine a difference between the two situations.

The other condition is that the solution must be perturbation-stable. To be perturbation-stable simply means that if the wavefront is slightly different than that of the cavity solution [Eq. A-24], the small deviations from this solution should decrease with each round trip. This is similar to the difference between the stable equilibrium of a damped pendulum, and the unstable equilibrium of a pencil balanced on its head. Mathematically, assume a cavity solution $\boldsymbol{q}_{Cavity} = \boldsymbol{q}_C$, then if one actually starts with a beam where $\boldsymbol{q}_1 = \boldsymbol{q}_C + \Delta \boldsymbol{q}_1$, after one round trip the new complex wavefront curvature

$$q_2 = \frac{Aq_1 + B}{Cq_1 + D} = q_C + \Delta q_2 \qquad \textbf{[Eq. A-26]}$$

should be such that $|\Delta q_2| < |\Delta q_1|$. An analytical condition can be found by replacing q_1 into q_2, making the assumption that $|\Delta q| << |q|$, and removing q_C from both sides of the resulting equation. This gives

$$\frac{\Delta q_2}{\Delta q_1} = \left(\frac{A+D}{2} \mu \sqrt{\left(\frac{A+D}{2}\right)^2 - 1} \right)^2 \equiv \lambda^2 \qquad \textbf{[Eq. A-27]}$$

where the sign is opposite to the corresponding solution in q_C determined from [Eq. A-24]. λ corresponds to the eigenvalues of the ABCD matrix, and is often termed the perturbation eigenvalue, even though the perturbations actually grow as λ^2. With real matrix elements, m^2 must be less than 1 or the deviations from the cavity solution will simply grow in time. While this is basically the same criterion for having a confined cavity mode, the difference becomes apparent when the matrix elements are complex, as the element B is present in [Eq. A-24] but not in the perturbation eigenvalues, so a confined but unstable solution is possible (again, much like a pencil on its head – the solution exists, but is unstable).

A.4 Results of the program

The entire purpose of modelling the Regen was to help determine whether we could replace one of the curved cavity mirrors, so the first step was to determine the cavity mode with the Regen as it was. The parameters of our Regen were as follows (see Figure A-5 and follow from the first plane mirror): $L_1 = 29cm$, $\theta_1 = 15^o$, $R_{Mirror1} = 1m$, $L_2 = 78.5cm$, $R_{Mirror2} = 0.5m$, $\theta_2 = 15^o$, and $L_3 = 64.5cm$, where the folding angles θ_1 and θ_2 are the angles between the crystal arm and the Pockels Cell and Prism arm respectively. This led to the cavity mode in Figure A-6. To switch the second curved mirror to a 1m mirror, different parameters needed to be chosen to maximize the size of the beam at the Pockels Cell within realistic limits for the size of the Regen given our workspace. The cavity mode in Figure A-7 was obtained using parameters of $L_1 = 50cm$, $L_2 = 102cm$, and $L_3 = 90cm$. Note that while the size of the mode was found to increase as the value of L_2 decreased, the cavity mode quickly became more unstable. As a compromise, L_2 was chosen to be at least 1 inch away from the point where the cavity would be completely unstable.

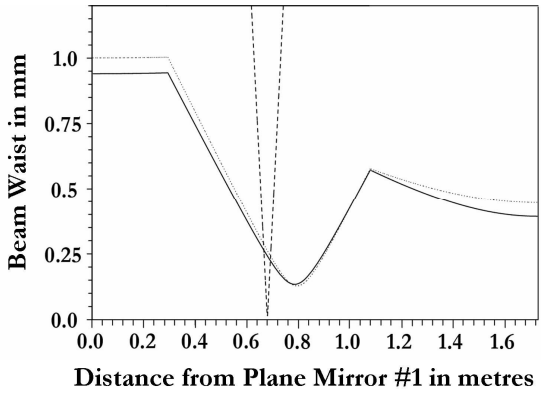

Figure A-6: Cavity mode in the present Regen with astigmatism included. The solid line is the tangential cavity mode, the dotted line is the sagittal cavity mode, and the dashed line is the pump beam entering the cavity through the second curved mirror.

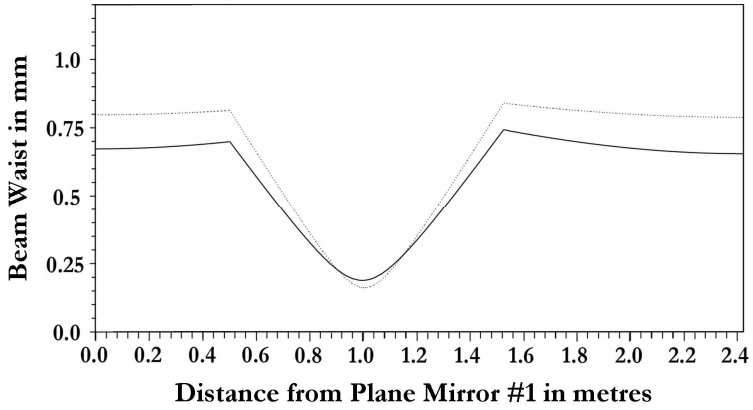

Figure A-7: Cavity mode when the 50cm curved mirror was replaced by a 1m. The solid and dashed lines are as described in Figure A-6.

Comparing the graphs in Figure A-6 with Figure A-7, the first thing to notice is that while the beam size is better at the second plane mirror, the beam size at the Pockels Cell has decreased significantly, which is definitely not acceptable. As well, the Regen would be operating close to the edge of unstable operation making its operation tricky. Finally the physical dimensions would be significantly larger, necessitating the rearrangement of practically the entire optical bench. As the damage to the crystal had been remedied simply by moving the crystal away from the focus during the development of this program, the switching of the mirror was deemed unnecessary. However, having developed a program that could look a the behaviour of the Regen, it was interesting to get a sense of how it behaved as a function of the lengths between different optical elements L_1, L_2, and L_3.

The crucial details to pay attention to were again the perturbation-stability determined by m^2, and the energy densities at the mirrors and in the Pockels Cell. While

the plane mirrors should be able to withstand between 1 and 3J/cm^2, the focussing mirrors and Pockels Cell would damage above 1J/cm^2. The peak energy density was calculated by assuming it followed a form much like the intensity: a Gaussian profile where the beam waist w marks the $1/e^2$ point. The spatial integral over energy density

$$\int_0^{2\pi} d\theta \int_0^{\infty} D_0 \cdot e^{\frac{-2r^2}{w^2}} \cdot r \cdot dr \qquad \textbf{[Eq. A-28]}$$

should then equal the total energy in the pulse. This yields the relation

$$D_0 = \frac{2E}{10^{-4}\pi w^2} \qquad \textbf{[Eq. A-29]}$$

in J/cm^2 when w is in metres. The plots of the energy density for the mirrors as a function of L_1, L_2, and L_3 are shown in Figure A-7, where the maximum energy in the cavity was taken to be 5mJ. The legend follows the optical elements from the one experiencing the highest energy density to that with the lowest, plus a plot of m^2 where the magnitude of the scale is the same, but the units are dimensionless. Note that the plots for the Plane Mirror #1 and Lens #1 (Curved Mirror #1) overlap for all three graphs, and as such they also describe the energy density at the Pockels Cell.

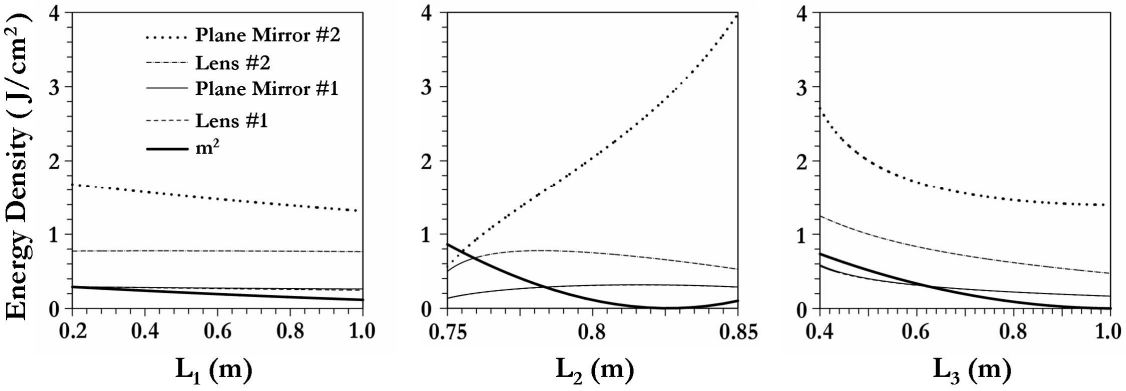

Figure A-8: Variation in the energy densities at various optical elements with the separations L_1, L_2, and L_3. Note that the when plotting the Energy Density against one of the lengths, the other two are kept at their nominal values of L_1=29cm, L_2=78.5cm, and L_3=64.5cm

In terms of the flexibility in the design, the most restrictive condition seems to be that on L_2 – within a range of about 10cm the cavity mode can switch from being unstable but having low energy densities on all the optics, to a point where it is incredibly stable but the energy density is dangerously high on the second plane mirror. The other two distances

however can both be increased significantly, with an overall increase in mode stability and a reduction in the energy density at the mirrors. Recalling that the damage thresholds for the curved mirrors and Pockels Cell are ~1J/cm^2, for the crystal and prisms ~5J/cm^2, and for the plane mirrors are between 1J/cm^2 and 3J/cm^2, it should be noted that for the current design of the Regen plane mirror #2 is in danger of damaging. However, since none of the other optical elements should damage, and as the damage to this mirror has been infrequent (once every couple of months), the design has been pretty much left as it was, with any successive adjustments made to the cavity tending to increase the distances $\boldsymbol{L}_1$ and $\boldsymbol{L}_3$ to reduce the probability of damaging this mirror (as far as its allowed by the space on the optical bench).

Appendix B: Alignment

Some of the most valuable experience I've obtained working with ultrafast lasers have been when things have broken down and needed repairing. However, the construction and alignment of the different systems in the lab typically relied heavily on the advice of my supervisor, with little supplementary documentation or illustration available to assist the student. While the process of alignment is not difficult conceptually, it is one of the most common and sometimes most frustrating tasks that a student encounters in a laser lab. This appendix is designed to fill this gap somewhat by providing an account of the things I took into account when building various optical setups, starting with general ideas for simple optics, progressing to the alignment of more complicated elements such as the Pockels Cell, and concluding with the construction and alignment of a Regenerative Amplifier. These are some of the practical skills one must learn to be effective in the laboratory, and as such this section will hopefully be an instructive guide for new students in the laser lab.

B.1 Plane Mirrors

By far the most common element used in our lab, the alignment of plane mirrors is relatively simple, yet can have some unexpected effects on the performance of an optical system. The first thing to be considered is the design specifications of the mirror itself – the dependence of the reflectivity on the angle of reflection, the polarization, and the wavelength. All of these have a major impact on the throughput of a given system, especially given the ultra-broad bandwidths that are produced in a femtosecond lab, and as such each mirror should be labelled appropriately on its edge and a data sheet filed.

As a concrete example of why such care should be taken, our initial investigations into MRG suffered from mirrors that had a very poor reflectivity at longer wavelengths. Note that in the spectrum of Figure 4-1, the Stokes orders after the strongly saturated 845nm peak drop drastically, but produce a plateau on the linear scale. A plateau is normally suggestive of the saturation of MRG, and as such should not be as weak as what was observed (note that the saturated peaks are likely orders of magnitude stronger than shown in the Figure, as they were very strongly saturating the detector). Using the wrong mirrors was an oversight that contributed to significant delays in this experiment.

One thing that is affected by the alignment specifically is the polarization of the beam. This is often exploited in periscopes to switch the polarization from p- (parallel)

polarized relative to the optical bench, to s- (perpendicularly) polarized relative to the optical bench. The action of a periscope on the polarization is depicted in Figure B-2. In an analogous way, combinations of mirrors that are angled away from the plane of the optical bench can skew the polarization and thus affect things such as the transmission through the experiment (see the P and S curves in Figure 4-1(b)). This is particularly significant when using a pair of mirrors that are very close together, since they can be skewed at large angles while still redirecting the beam in the right direction.

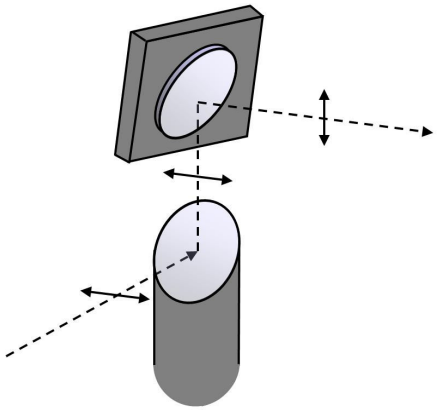

Figure B-2: All reflective polarization rotation

My final comment on the alignment of plane mirrors concerns aligning a beam into an optical system using a pair of mirrors. As opposed to something on translation stages where the alignment can be thought of in terms of a Cartesian "x and y" system, plane mirrors lend themselves more to a polar "position and angle" sort of idea, since a single mirror can only adjust the direction of a beam. With this sort of thinking, the mirror closest to a given setup acts as the angle adjustment, while an earlier mirror acts as the position adjustment. A system of two irises provides a convenient demonstration of this idea (Figure B-3). While the position mirror does affect the angle of entry, and the angle mirror does affect the position of the beam at the entrance of the system, these effects can be minimized by placing the position mirror as far away from the system as possible (to maximize the movement of the beam for a given adjustment in angle), and placing the angle mirror as close to the system as possible (to minimize the movement of the beam for a given angle adjustment). By iteratively adjusting the position and angle mirrors, one can quickly achieve the desired alignment. Conversely, if one wants to set a pair of irises for future alignments, the first iris should be placed as close to the angle mirror as possible, and the second iris should be placed as close to the optical system as possible.

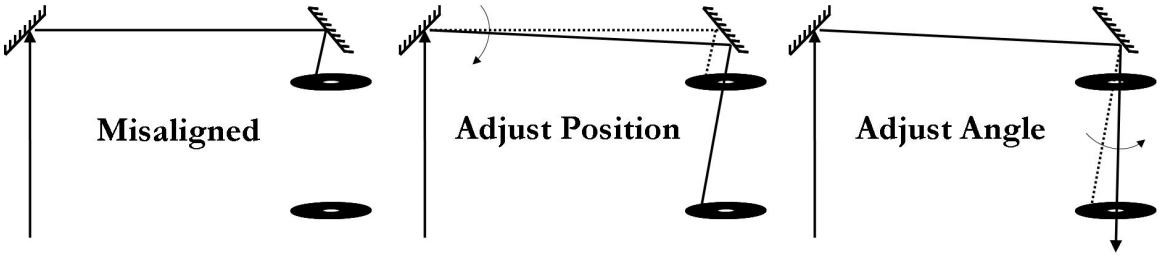

Figure B-3: Using plane mirrors for a Position-Angle alignment

B.2 Lenses

Aligning a lens is relatively simple, as there are only a few things that need to be considered. The first thing to note is that if the beam enters off-axis, it will be skewed towards the opposite direction as it exits the lens. This can be avoided by setting a reference point for the beam before the lens is in place, and adjusting the position of the lens to bring the beam back on that reference.

For a short-focal-length lens where this may be difficult, one can take advantage of the light reflected from the two surfaces of the lens. There will typically be one diffuse (sometimes plane) reflection, and one focusing reflection as demonstrated in Figure B-4. To see these reflections the lens will have to be slightly tilted to send them off-axis, where they can be viewed on a card without interrupting the incoming beam. When the lens is moved in the x and y directions, the relative positions of the reflections will change – the proper alignment being when they lie one on top of the other. It is important that after any alignment with the lens, these reflections should be sent into some sort of beam dump, or better yet a diagnostic of the system. Otherwise, there is unnecessary stray light in the lab, and there is the potential to damage other optical elements that may happen to be in the focus of the second reflection.

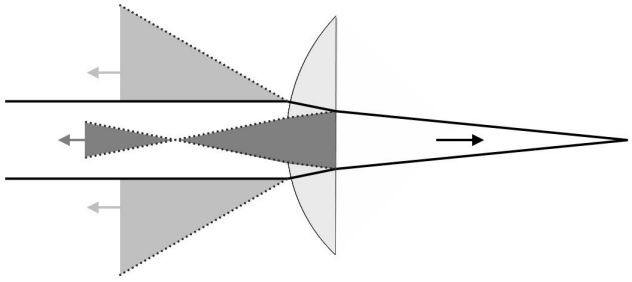

Figure B-4: Aligning a lens. The diffuse (or possibly plane) reflection is from the front surface and is depicted in light grey. The focussed reflection is from the second surface and is in dark grey.

B.3 Prisms

As the lasers used in this ultrafast lab typically lase at two colours simultaneously, many systems use components such as prisms and gratings that spatially disperse the two colours. This is used as a way of independently manipulating the beams, such as when selecting colours or compressing the pulses. When using prisms, there are three major adjustments needed for alignment – the angle of the prism relative to the beam, the tilt of the prism along its length, and the tilt along its breadth (Figure B-5b, c, and d respectively). For the principle angle alignment, a useful reference is the angle of least deviation. This is defined as the angle at which the beam is deflected the least from its original path (see Figure B-5a). This is important partly because the alignment is reproducible, and since the prisms are used in pairs, for one to undo the action of the other the opposite faces must be parallel (this can be thought of as a block of free-space placed at an angle within a block of material – recalling that a block of material should not angularly disperse a beam of light. Try drawing it if you don't know what I mean). Two prisms can then be aligned by setting each one at this angle of least deviation. As a convention, I approach this angle by rotating the prism clockwise (if it were positioned as in Figure B-5a), until the front edge (long wavelength edge), of the dispersed beam has stopped.

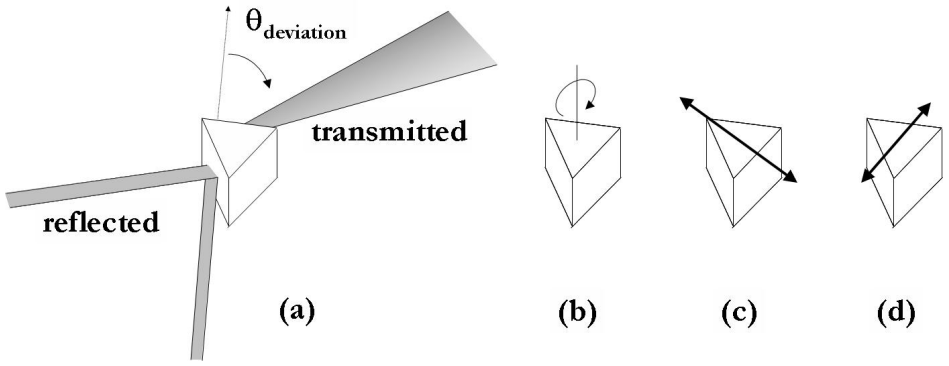

Figure B-5: Alignment of a prism. (a) Angular dispersion of a beam through the prism. (b) Primary angle adjustment. (c) Tilt of the prism along its length. (d) Tilt of the prism along its breadth.

The remaining two adjustments for the tilt of the prism affect the vertical deviation of the transmitted and reflected beams. There should be two screws on the prism holders to adjust these tilts. The tilt of the prism along its length (Figure B-5c) primarily affects the alignment of the transmitted beam, whereas the tilt along its breadth (Figure B-5d) affects both beams roughly equally. For alignment purposes then, one should start by adjusting the tilt along the breadth of the prism to bring the reflected beam into alignment, and then

adjust the tilt along its length. These two alignments should be done iteratively, until there is no noticeable difference between the height of the input beam and the two output beams.

B.4 Gratings

The gratings in the lab are typically reflective-type gratings, where a repetitively scored surface reflects a beam into various diffractive orders. Usually they are designed to primarily reflect the beam into the first order, so that much like a prism the beam will undergo an angular dispersion to spatially separate its frequency components. The gratings cannot perfectly reflect the beam into the first order however, so a zeroth order reflection is typically generated as well, which acts as if the grating were a simple mirror. A schematic of the reflection from a grating is shown in Figure B-6a. Note that this zeroth order reflection is a useful diagnostic of the spectrum of the pulse, as it remains a collimated beam, however if it is not used in this fashion, it should be blocked to prevent stray laser light in the lab.

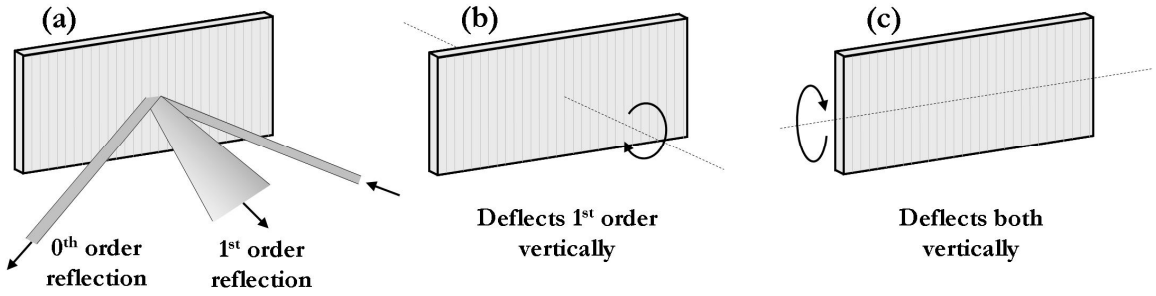

Figure B-6: Alignment of a grating. (a) Angular dispersion of the first order reflection. (b) Rotation about the face of the grating. (c) Rotation of the grating along its length

The alignment of the gratings is in many ways very similar to the alignment of a prism. The primary angle adjustment affects the direction of the first order reflection relative to the input beam, and for maximum dispersion the first order should be set as close to the Littrow angle as possible, which is the angle at which the first order is reflected back along the input beam. The two adjustments analogous to the tilt of a prism are the rotation of the grating about an axis normal to the face of the grating (Figure B-6b), and the rotation of the grating about its length (Figure B-6c). By rotating the grating about its face, the zeroth order remains unaffected as the normal to the surface hasn't changed direction. However, the orientation of the grooves will have rotated, deflecting the diffracted first-order beam accordingly. Rotating the grating about its length affects both beams roughly equally, and so analogous to the prism one should first adjust the grating about its length to bring the zeroth order into alignment, and then adjust it about its face to bring in the first

order. Note that since the grating mounts cannot be set perfectly the adjustments will not be exactly along those axes, so they should be adjusted iteratively to bring the grating into as good an alignment as possible.

B.5 Grating Compressor

While the compressor in the lab compresses two beams simultaneously, it is sufficient to consider the alignment for the case of a single-beam compressor. Following the path as depicted in Figure B-7a, the incident horizontal beam travels over the top of the output mirror, and is dispersed into the first grating order at an angle that is as close to Littrow as possible (as close to going back on itself as possible). The beam is then re-collimated by orienting the second grating so that the beam travels parallel to its original path. A mirror reflects the beam back on itself, but with a slight tilt downward to aim the beam at the output mirror placed below the incoming beam. The input beam and its retro-reflection should then be vertically separated on the two gratings as in Figures B-7b and c.

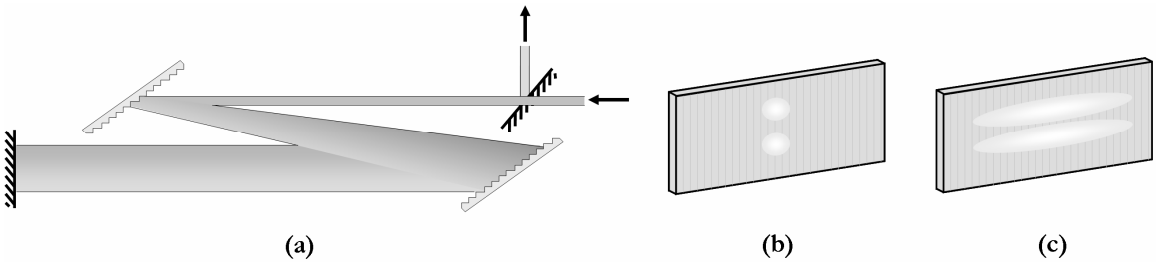

Figure B-7: Alignment of a grating compressor. (a) Top view of a compressor. (b) & (c) Diagram of the beams on the first and second grating as seen through an IR viewer.

B.6 Pockels Cell

The alignment of the Pockels Cell is a bit trickier than that of the simpler optical elements described up to now. A Pockels Cell acts as an optical switch in a Regen cavity as it uses a voltage-dependent birefringent wedge (the wedge shape helps prevent damage). When in use, the birefringence is usually set to act as a quarter-wave plate when a voltage is off, changing the polarization of the light that passes through it from linear to circular (this is described in more detail in **§3.2.1**). The typical alignment procedure (known as the "Eye of God" alignment), takes advantage of this affect on the polarization. The alignment setup using the seed for our Regen is demonstrated in Figure B-8, where the Pockels Cell is the box, in front of it is a linear polarizer with a diffuser (piece of tape), on the back is another linear polarizer that is crossed with the first one, and the light is depicted in grey. Note that

we actually only have large circular polarizers in the lab, but in the proper orientation these will act as linear polarizers. The alignment procedure is as follows:

1. Position the Pockels Cell without the polarizers in place so that the seed goes through as well as possible. This may require lifting it vertically depending on the optical axis of the cavity.
2. Place the polarizers on either side (without the diffuser), to get them crossed as well as possible. This won't be perfect so some seed will still get through, which will actually become an asset later.
3. Place the tape on the front polarizer. When the Pockels Cell is aligned properly this should give a circle of light with a dark cross in the centre, with an overall surrounding ring of light. It should look like the left-most pattern in Figure B-8, however without the central spot. If the seed were strong enough the spot would be there, but the tape generally attenuates the beam to the point where this isn't visible.
4. For the fine adjustment of the position, the dark cross and the central spot should line up on each other. Since the spot isn't visible with the tape in place, I simply moved the polarizer back and forth to move the tape in and out of the beam.
5. For the angular alignment, the dark cross should line up with the broad background circle of light (and forms a ring when properly aligned).

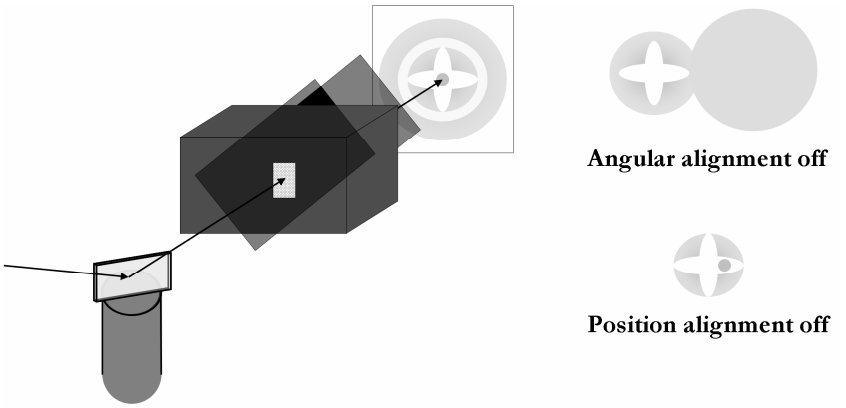

Figure B-8: "Eye of God" alignment for a Pockels Cell

As with all alignments, the last two steps may have to be repeated iteratively. Once this is done, the Pockels Cell will act as a quarter-wave plate when the voltage is on, which is opposite to the desired operation in the Regen. This can be remedied by using the

adjustment screws, which will be discussed in the section on building the Regenerative Amplifier.

B.7 Building the Regenerative Amplifier

There have been a few times that the Regen has needed to be rebuilt, usually after something became seriously damaged (like the crystal), or its operation was substandard. When all the mirrors and elements had been tweaked to no effect, the last resort was to take the Regen apart bit by bit to find where the problem might be. The one time it was taken apart completely was when we thought the pump beam was misdirected vertically, setting an odd optical axis that was likely sending the infrared beam up and down throughout the Regen cavity, possibly affecting the polarization and hence the cavity gain and losses. This complete disassembly should be done truly as a last resort, as it is very time-consuming to realign properly.

This section will present a particular way of constructing the Regen, but keep in mind that there are many other ways of doing it, and this should really be used as a guideline. The main thing to remember is that regardless of the procedure, when doing this alignment ***only one optic should be adjusted at a time*** before setting some sort of reference. This is to ensure that it's possible to go back to an earlier configuration if a mistake is made.

B.7.1 Align the Pump Beam

The most important consideration for an amplifier is the overlap of the seed beam with the pump beam, as there can be no amplification if there is no overlap. As such, it is the pump beam that defines the optical axis of the laser, and so that is where the construction of the Regen should start.

Initially, send the pump beam through its lens and the mirror that to this point has been labelled the second curved mirror. Check to see that it is going flush to the table, and then insert the crystal. Rotate the crystal about its length so that the reflection from the front surface is also going flush to the table, and then rotate the crystal as shown in Figure B-9, until the reflection at the front surface is minimized. The crystal will then be at the Brewster's angle, which is where p-polarized light experiences no reflection. Note that this is slightly different than the Brewster's angle for an IR beam, but it should be close enough. Once this is done, the axis should be recorded using two irises, positioned such that they are

as close to either end of the cavity as possible, without getting in the way of the cavity mode itself. The first curved mirror and a beam dump should also be in place.

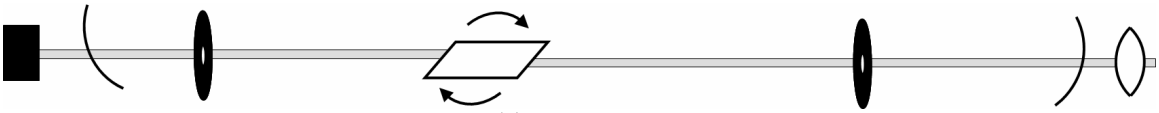

Figure B-9: Alignment of the pump beam. The irises are a reference for the optical axis of the cavity.

B.7.2 Align the Polarizer and Curved Mirrors

The next step is to align the polarizer and mirrors using the seed beam. Position the polarizer roughly where it should be, and use two redirecting mirrors (position and angle), before the cavity as shown in Figure B-10 to direct the seed into the first curved mirror. Using the first curved mirror and one of the redirecting mirrors, align the seed to the two irises in the cavity. The alignment will probably not be perfect, as the deviation of the green pump beam in the crystal will be slightly different than the deviation of the IR beam.

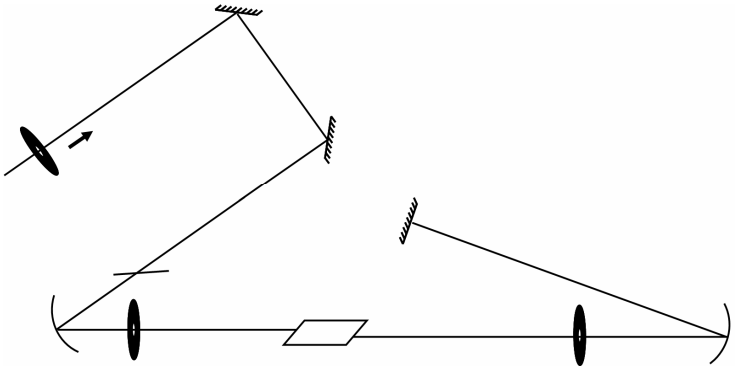

Figure B-10: Alignment of the curved mirrors

To set the alignment of the polarizer, use a half-wave plate to make the beam s-polarized, which should be completely reflected by the polarizer when everything is aligned correctly (depending on where the seed is taken from, it may already be s-polarized). Look for a minimum in the transmitted beam when adjusting the polarization, as it is easier to find than the maximum of the reflected beam. Note that both the reflection and transmission of the beam through the polarizer should be flush to the table, and if they are not there should be two adjustment screws on the polarizer mount. With the polarization set, determine the optimal angle of the polarizer by rotating the polarizer and again finding the minimum in the transmitted beam.

Once through the second iris, angle the second curved mirror towards a third plane mirror, which for the time being will act as plane mirror #2 as shown in Figure A-5. Ensure

that the beam is flush to the table. This plane mirror should then be aligned to send the beam back *exactly* on itself – this will be critical to get the Regen lasing later in the procedure, and once this is set do not adjust it until it is up and lasing. To aid in this alignment, use another iris as far back along the beamline as possible.

B.7.3 Align the Input of the Seed

With three of the four cavity mirrors set, ensure that the seed will keep this alignment when it is injected by reflection off the polarizer. Using another iris to mark how it went into the cavity in the previous step, reflect it off the polarizer and use a pair of mirrors earlier in the beamline to bring it into alignment (Figure B-11).

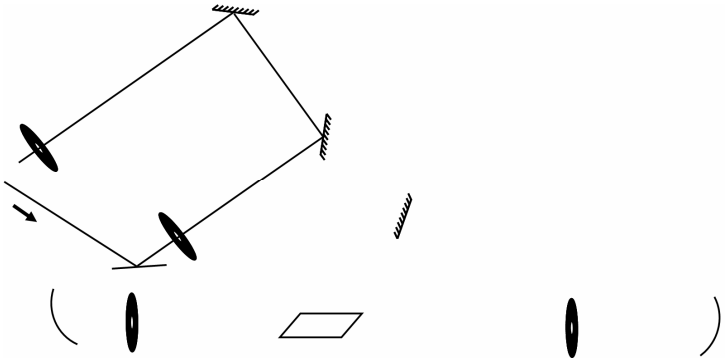

Figure B-11: Setting the input of the seed as it will be used in regular operation.

B.7.4 Align the Last Cavity Mirror and the Pockels Cell

With the seed aligned, introduce the Pockels Cell into the cavity, and align it as described in **§B.6**. Note that the Pockels Cell will currently be working opposite to what is desired, as it will act like a quarter-wave plate with the voltage on. To remedy this, set up the last cavity mirror as shown in Figure B-12, which was earlier called plane mirror #1. The beam should be sent back on itself so that it again goes through the two irises in the cavity. By introducing a fast diode in the path of the beam, it is possible to observe the effect of the Pockels Cell on the seed, which can then be used to set it to the proper configuration.

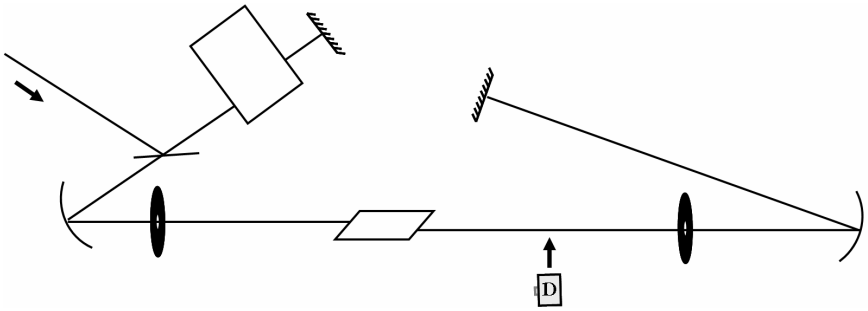

Figure B-12: Alignment of the Pockels Cell using a diode.

When the Pockels Cell is working as a voltage-on quarter-wave plate, a diode placed in the path of the seed will read a trace much like Figure B-13a, where the period between the peaks is determined by the repetition rate of the oscillator. To interpret what is happening, note that when the Pockels Cell is doing nothing, the s-polarized seed should reflect off the polarizer, go through the Pockels Cell twice, and then again reflect off the polarizer as the polarization should be the same. As the Pockels Cell cannot be set to have exactly zero birefringence (and the polarizer may not be aligned perfectly), there will be some light that leaks into the cavity, and therefore a small signal will be apparent. When the voltage is turned on, the Pockels Cell should let almost all of the seed into the cavity by changing it first to circular polarized light, and then to p-polarized as it is reflected back through. When it is turned off again the signal should go back down. To get it to work in the opposite configuration, adjust one of the screws at the back of the Pockels Cell (while being careful of the high voltage line), to make the pattern switch from Low-High-Low to Low-Low-High (or High-Low-Low). At this point, adjust the other screw until the pattern becomes High-Low-High, as in Figure B-13c. The ratio of the peak heights should be 8:1 or better.

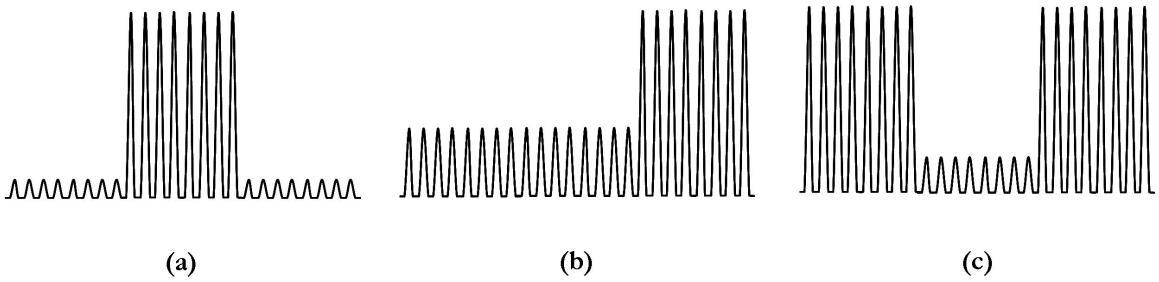

Figure B-13: Typical traces from a fast diode when aligning the Pockels Cell. (a) Operation when it is acting like a voltage-on quarter-wave plate. (b) Intermediate stage by adjusting one of the alignment screws. (c) Operation when it is acting like a voltage-off quarter-wave plate.

B.7.5 Remove the Diode and get it Lasing

With the diode removed from the cavity, it should be possible to get the Regen lasing. Try to only use plane mirror #1 to bring the cavity into alignment, as it was aligned only by using the irises, and if necessary it can be brought back to that alignment. If this does not work, make sure that the output timing on the Pockels Cell is set to 100, so that the lasing is not being cut off prematurely. If lasing is still not possible, plane mirror #2 can be adjusted. Once the Regen is acting like a laser, iteratively adjust both of the plane mirrors to maximize the energy in the pulses. Do not adjust the curved mirrors.

B.7.6 Insert the Prisms and finish the Alignment

To finish the Regen, the beam must be dispersed in the cavity to obtain a two-colour output. This is done using a system of three prisms as shown in Figure B-14. Using again the angle of least deviation as a reference, align the prisms as described in **§B.3** to disperse the two colours in the cavity. They must be well separated so that the colours can be spatially dispersed enough to allow for two-colour operation. Adjusting only plane mirror #2, first bring one colour and then the other back into alignment. The slits used for control of the two colours can then be placed after the prisms, as can an optional attenuator using a combination of a polarizer and a half-wave plate. This can be used to control the relative energy between the two colours. With this done, you now have a two-colour regenerative amplifier!

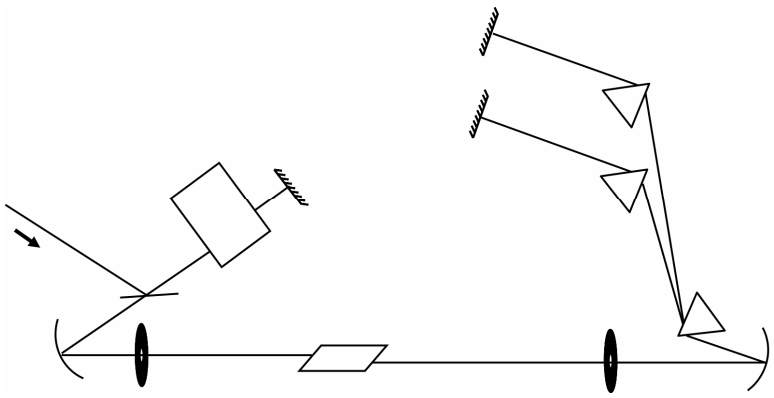

Figure B-14: Final alignment of the Regen.

Appendix C: Computer Code

This is a transcript of the computer code used to model MRG. It was created in Matlab, and as such any percent signs (%), are commented code, and are ignored in the program. These are used to provide notes, or to switch back and forth from one variable to another.

```
clear;
tic

%%%%%%%%%%%%%%%%%%%%
%Defining constants%
%%%%%%%%%%%%%%%%%%%%

%%Assume a value of the Raman gain - figure it out later
g= 1.6e-13;
c= 3e8; %%in m/s

%%The Raman transition
omegaRaman= 775; %%in wavenumbers
dephasingTime= 6.6; %%in picoseconds
HWHMRaman= .2206/(dephasingTime*1e-12)/3e10/2; %%in wavenumbers
%HWHMRaman= 100; %%in wavenumbers
convolution= 0; %%over what TOTAL range should a convolution be carried out in
wavenumbers
                %% Note that a higher value is more accurate, but also much more taxing
                %% Also note that this will affect the value for g

%%Define the fibre characteristics
FibreLength= 1;  %%in meters
Intervals= 1000;  %%number of points per meter; this number must be large for the program
to work
plotPoints= 1000; %%when plotting in 3d, it's best to have only 1000 points
fibreRadius= 250; %%in microns
Pressure= 3; %%in atmospheres
u11= 2.405; %%zero of the Bessel function J[0](x)
dz= FibreLength/Intervals;

%%Define largest Stokes and Anti-Stokes order you want to include
S_Orders= 20; %%including the long-wavelength beam
A_Orders= 20;

%%You can't interactively change the scale on a surface plot, so set the number you want
to plot
minorder= -S_Orders; %%use -S_Orders for all of them
maxorder= A_Orders; %%use A_Orders for all of them

%%Set the frequency resolution
%%Note that a typical bandwidth is about 80 wavenumbers, so a spacing of 16 is
appropriate
omegaRes= 7; %%In wavenumbers

%%Set the initial intensity of the Pump, and then the energy ratio between it and the
Stokes
Intensity= 6e12; %%in W/cm^2, but I don't think it matters, as g is a parameter to be
determined
ratio= 1.5;

%%Finally, set the smallest intensity (relative to the Pump), that you want to plot
plotmin= 1e-4;

%%Labeling convention: short-wavelength beam (Pump beam) is order# S_Orders+3
%%                     long-wavelength beam (Stokes beam) is order# S_Orders+2
%%I'm adding two extra orders on either end for programming considerations
Pump= S_Orders + 3;
Stokes= S_Orders + 2;
```

```
toc

%%%%%%%%%%%%%%%%%%%%%%%%%%%%%%%%%%%%%%%%%%%%%%%%%%%%%%%%%%%%%%%%%%%%%%%%%%%%
%Determining resolution and constructing the input spectrum from our data%
%%%%%%%%%%%%%%%%%%%%%%%%%%%%%%%%%%%%%%%%%%%%%%%%%%%%%%%%%%%%%%%%%%%%%%%%%%%%

omegaIntervals= ceil(omegaRaman/omegaRes); %%number of intervals per order

%%I'm going to make sure that there are an odd number of intervals per order.  By forcing
%%  an odd number, I can define the array elements by using the orders as a reference.
%%  Notice how in the diagram below there are two points on either side of each order
%%  when there's 5 intervals per order.
%%  ..|....|....|....|....|..
%%Equivalently, the # of side elements = (# of intervals - 1)/2

%%The pump frequency is therefore at an index of (Pump Order)*(elements/order)
%%  - the bit on the side

%%  ..|....|....|....|....|....|....|..
%%  1   ^n   ^2n  ^3n  ^Pump*n          the arrows point to the element in question
%%                            n=5, Pump Order=3, S_orders=1, A_orders=1, bit on the
side=2


if (mod(omegaIntervals, 2)== 0)
    omegaIntervals= omegaIntervals + 1;
end
side= (omegaIntervals - 1)/2;

%%This now sets the actual resolution, which will be as good as or better than
%%  the specified resolution
omegaRes= omegaRaman/omegaIntervals;

%%Read in the Regen Spectrum
path(path, 'C:/Documents and Settings/Compaq/My Documents/Frasers/Frasers
Junk/Waterloo/Work/MRG/Data/Data Analysis/mrg104_308_AND036-AND064');
[lambdaReg, IntensReg]= textread('AND064.mat', '%f %f', 'expchars', 'E', 'commentstyle',
'matlab');
omegaReg= 1e7./lambdaReg;

RegenSpec= zeros(length(omegaReg), 2);
RegenSpec= [omegaReg IntensReg];

%I'm artificially subtracting the background, as I didn't take one to begin with.
RegenSpec(1: length(omegaReg), 2)= sqrt((RegenSpec(1: length(omegaReg), 2) - 9e-7).^2);
RegenSpec(1: length(omegaReg), 2)= sqrt((RegenSpec(1: length(omegaReg), 2) - 3.5e-7).^2);
RegenSpec(1: length(omegaReg), 2)= sqrt((RegenSpec(1: length(omegaReg), 2) - 1.75e-
7).^2);
RegenSpec(1: length(omegaReg), 2)= sqrt((RegenSpec(1: length(omegaReg), 2) - 0.9e-7).^2);
RegenSpec(705: length(omegaReg), 2)= 0;
RegenSpec(220: 620, 2)= 0;
RegenSpec(1: 70, 2)= 0;

%%Determine the frequency spacing
points= length(omegaReg);
range= omegaReg(1) - omegaReg(points);
dOmegaReg= range/points;

%%Determine the desired index spacing from the specified resolution.  This should
%%  give a resolution that is as good or better than that specified
spacing= floor(omegaRes/dOmegaReg);
omegaRes= spacing*dOmegaReg;

RegIntervals= floor(points/spacing); %%number of intervals over entire Regen range

%%This is an example of what the array could look like; this time the lines are
%%  showing the array elements we want to keep
%%    |........|........|........|....  "points= 32, spacing= 9, intervals= 3"
%%   1^     9+1^   2*9+1^   3*9+1^ 32^      Listing the index at the arrow

%%Now to get rid of all the extraneous points.  Follow the diagrams above and below
```

```
%%    |........|........|........|....
%%    |........|........|........|
%%    ||........|........|
%%    |||........|
%%    ||||
RegenSpec((spacing*RegIntervals + 2): points, :)= [];
for n= 1: RegIntervals
    RegenSpec(1 + n: spacing + n - 1, :)= [];
    omegaReg(1 + n: spacing + n - 1, :)= [];
end

%%Now to set the ratio between the pump and the Stokes.  We measure energy, so integrate
%%  the two peaks in the spectrum and determine the ratio of the areas.
[pumpmax, pumpindex]= max(RegenSpec(:, 2));
omegaPump= omegaReg(pumpindex);
RegenSpec(:, 2)= RegenSpec(:, 2)./pumpmax; %normalize the array to the Pump intensity

StokesArea= 0;
PumpArea= 0;

%%In the original file, the Stokes beam is between the 70th and 220th data point,
%%  and the Pump beam is between the 570th and 710th data point
for n= floor(70/spacing): ceil(220/spacing)
    StokesArea= StokesArea + (RegenSpec(n, 2) + RegenSpec(n - 1, 2))/2;
end

for n= floor(570/spacing): ceil(710/spacing)
    PumpArea= PumpArea + (RegenSpec(n, 2) + RegenSpec(n - 1, 2))/2;
end

SpectraRatio= PumpArea/StokesArea;
scale= ratio/SpectraRatio;

RegenSpec(floor(70/spacing): ceil(220/spacing), 2)= RegenSpec(floor(70/spacing):
ceil(220/spacing), 2)...
                                                        ./scale;

%%Initialize the Frequency and Intensity arrays
%%I'm adding a couple extra orders on either end as it's needed later
omega= (omegaPump - (omegaIntervals*(S_Orders + 2) + side)*omegaRes: omegaRes: ...
    omegaPump + (omegaIntervals*(A_Orders + 2) + side)*omegaRes);
%%Translation: Start at the centre, go back by ((the number of Stokes orders + two extra)
%%  *(number of array elements per order) plus the bit on the side),
%%  increment by the frequency resolution until you get to (Pump + Anti-Stokes +
%%  two extra orders), then add the number of elements on the side

In= zeros(1, length(omega));
for n= pumpindex: length(RegenSpec(:, 2));
    In(Pump*omegaIntervals - side - n + pumpindex)= RegenSpec(n, 2);
end

for n= 1: pumpindex - 1;
    In(Pump*omegaIntervals - side + n)= RegenSpec(pumpindex - n, 2);
end

%GVD= 0000e-6; %%I've set it to 10000; for Steve it was -1877
%TOD= 000000e-9; %%I've set it to 1000000; for Steve it was 18719
%extraphase= GVD/2.*(omega*100*3e8*2*pi).^2 + TOD/6.*(omega*100*3e8*2*pi).^3;

%lambda= 1e4./omega; %%this gives the wavelength in microns

toc

%%%%%%%%%%%%%%%%%%%%%%%%%%
%Set the phase dispersion%
%%%%%%%%%%%%%%%%%%%%%%%%%%

ngas= zeros(1, length(omega));
k= zeros(1, length(omega));
%ngas= ngas + 1; %%comment what's below to set no dispersion
```

```
%%Sellmeier equations for the gas

ngas= 1 + Pressure*0.7e30./((31.9e15)^2 - (2.*pi.*c.*100.*omega).^2); %%from
physrevA68_023812p15_2003

%%Sellmeier equation for fused silica
%nsilica= sqrt(1.2955 + 0.80985*lambda.^2./(lambda.^2 - .0107945) + ...
    0.91714*lambda.^2./(lambda.^2 - 100));
nsilica= 1.5;
n1= (nsilica.^2 + 1)./(2.*sqrt(nsilica.^2 - 1));

%%Axial wavevector for the EH11 hybrid mode
k= 2.*pi.*omega.*100.*ngas.*(1 - 1/2.*(u11./(omega.*100)./(2.*pi.*fibreRadius)).^2).*(1 -
i*n1./(omega.*100)/pi/fibreRadius);

%%%%%%%%%%%%%%%%%%%%%%%%%%%%%
%Electric Field Amplitudes%
%%%%%%%%%%%%%%%%%%%%%%%%%%%%%

toc;
A= zeros(size(In));
B= zeros(size(In));
C= zeros(size(In));
P= zeros(1, Intervals + 1);

A= sqrt(In);
B= A;
C= A;
%%I'll use A, B, and C to keep track of things as I go through the program

%%These next two things are what I'll use to graph the pulses
%surfacegraph= zeros(Intervals+1, (A_Orders + S_Orders + 5)*omegaIntervals);

%%Propagate in z
for z= 0: Intervals

    %%Sum over the absorption(i)->emission(j) events within a reasonable range
    %%  Convolving each contribution with a particular detuning range
    for x= -ceil(convolution/2/omegaRes): ceil(convolution/2/omegaRes)
        %%I don't want to include the extra orders I put in, so start just beyond the
        %%  first order and go to the end of the Anti-Stokes (see diagram below)

        %%  ..|....|....|....|....|....|....|..
        %%  1   ^n   ^2n  ^3n  ^Pump*n          the arrows point to the element in
question
        %%                            n=5, Pump Order=4, S_orders=1, A_orders=1, bit on
the side=2

        %%Initialize the material excitation for each detuning
        %%  (de-excitation is given by its complex-conjugate)
        Q= 0;

        for n= 3*omegaIntervals + 1: (Pump + A_Orders)*omegaIntervals
        %%Using the definition of Q below, I need to start from one order above the
minimum

%            Omega= omega(n) - omega(n - omegaIntervals + x);
            Q= Q + B(n)*conj(B(n - omegaIntervals + x))...
                *exp( -i*(k(n) - k(n - omegaIntervals + x))*dz);%...
%                *1/(omegaRaman^2 - Omega^2 - 2*i*Omega*HWHMRaman);
        end

        P(z + 1)= real(Q);

        %%Increment each order
        for n= 2*omegaIntervals + 1: (Pump + A_Orders)*omegaIntervals
            C(n)= B(n) + g*Intensity/ngas(n)*omega(n)/omega(Pump)*...
                (conj(Q)*B(n + omegaIntervals - x)*exp(i*(k(n) - k(n + omegaIntervals -
x))*dz)...
                    - Q*B(n - omegaIntervals + x)*exp(i*(k(n) - k(n - omegaIntervals +
x))*dz))*dz;
```

```
        end
    end

    %%Now to define the values for a 3d plot in frequency and distance
    for n= 2*omegaIntervals + 1: (Pump + A_Orders)*omegaIntervals
        surfacegraph(z + 1, n)= C(n).*conj(C(n)).*Intensity;
    end

    B= C;
end


%%%%%%%
%Plots%
%%%%%%%

toc;
%%Now I'm changing the convention - the Pump is of order 0, and the Stokes is of order -1
X= ( -(S_Orders + 2) - side/omegaIntervals: 1/omegaIntervals: (A_Orders + 2) +
side/omegaIntervals);
Y= ((C.*conj(C))*Intensity);
L= log10((C.*conj(C) + plotmin)*Intensity);
figure(1)
%plot(X, Y)
plot(X, L)
xlim([-0.5 7])

SX= (0: FibreLength/Intervals: FibreLength);
SY= (minorder - side/omegaIntervals: 1/omegaIntervals: maxorder + side/omegaIntervals);
%%See diagram below

%%    ..|....|....|....|....|....|....|..
%%               min   P   max

%%The 3d plot works okay for 500 intervals; above and below that it gets messy
%plotinterval= floor(Intervals/500);

    %%Delete elements up to just before the side of the minorder (use the diagram)
    surfacegraph(:, 1: (Pump + minorder - 1)*omegaIntervals - 1) = [];

    %%Delete elements beyond the side of the maxorder, note that I've already deleted
    %%  some elements in the line above (the 2 is because of that extra order I added
earlier)
    surfacegraph(:, (-minorder + maxorder + 1)*omegaIntervals:...
        (-minorder + A_Orders + 3)*omegaIntervals - 1)= [];

    %%Delete elements in z to have only 1000 elements - this makes the best plot
    plotInterval= floor((Intervals)/plotPoints);
    for n = 1: plotPoints - 1
        surfacegraph((n + 1): (n + plotInterval - 1), :) = [];
        SX((n + 1): (n + plotInterval - 1)) = [];
    end
    if (length(surfacegraph(:, 1)) > plotPoints)
        surfacegraph((plotPoints + 1): length(surfacegraph(:, 1)), :) = [];
    end
    if (length(SX) > plotPoints)
        SX((plotPoints + 1): length(SX)) = [];
    end
SZ= surfacegraph;
    %%Delete some elements so that there's at most 500 points along z
%    if (Intervals> 500)
%        for n= Intervals + 1: -1: 1
%            if (mod(n, plotinterval)~= 1)
%                SZ(n, :)= [];
%            end
%        end
%    end

%SL= log10(plotmin.*Intensity + surfacegraph);

%SL = loggraph;
```

```
%    SL(:, 1: (Pump + minorder - 1)*omegaIntervals - 1) = [];
%    SL(:, (-minorder + maxorder + 1)*omegaIntervals:...
%        (-minorder + A_Orders + 3)*omegaIntervals) = [];
%    if (Intervals> 500)
%        for n= Intervals + 1: -1: 1
%            if (mod(n, plotinterval)~= 1)
%                SL(n, :)= [];
%                SX(n)= [];
%            end
%        end
%    end

figure(2)
mesh(SY, SX, SZ)
%mesh(SY, SX, SL)
%shading interp
toc
```

References

Abrams R.L. (1972) *Coupling losses in hollow waveguide laser resonators*, **IEEE Journal of Quantum Electronics 8**, pp.838-843

Akhmanov S.A. et al (1972) *Nonlinear and Active Spectroscopy with Tunable Parametric Oscillators*, **IEEE Journal of Quantum Electronics 8 (issue 6)**, p.524

Armstrong J.A. (1967) *Measurement of Picosecond Laser Pulse Widths*, **Applied Physics Letters 10**, pp.16-18

Aussenegg F.R. et al (1981) *Collinear and Noncollinear Emission of Anti-Stokes and Second Order Stokes Raman Radiation*, **Optics Communications 37**, pp.59-66

Backus et al (1998) *High power ultrafast lasers*, **Review of Scientific Instruments 69**, pp. 1207-1223

Bloembergen N. (1967) *The Stimulated Raman Effect*, **American Journal of Physics 35**, pp.989-1023

Boyd R.W. (2003) *Nonlinear Optics Second Edition*, Academic Press, San Diego, CA (USA)

Corkum P.B. (1993) *Plasma Perspective on Strong-Field Multiphoton Ionization*, **Physical Review Letters 71**, pp.1994-1997

Corkum P.B. et al. (1994) *Subfemtosecond pulses*, **Optics Letters 19**, pp. 1870-1872

Everall N.J. et al (1987) *Threshold Measurements of Stimulated Raman Scattering in Gases Using Picosecond KrF Laser Pulses*, **Optics Communications 64**, pp.393-397

Farkas Gy. and Toth Cs. (1992) *Proposal for attosecond light pulse generation using laser induced multiple-harmonic conversion processes in rare gases*, **Physics Letters A 168**, pp.447-450

Ferray M. et al. (1988) *Multiple-harmonic conversion of 1064nm radiation in rare gases*, **Journal of Physics B: Atomic Molecular and Optical Physics 21**, pp.L31-L35

Fleck J.A. Jr. and Layne C. (1973) *Study of self-focusing damage in a high-power Nd:glass-rod amplifier*, **Applied Physics Letters 22**, pp.467-469

Fork R.L. et al. (1981) *Generation of optical pulses shorter than 0.1psec by colliding pulse mode locking*, **Applied Physics Letters 38**, pp.671-672

Fork R.L. et al. (1984) *Negative dispersion using pairs of prisms*, **Optics Letters 9**, pp.150-152

Franken P.A. et al. (1961) *Generation of Optical Harmonics*, **Physical Review Letters 7**, pp.118-119

Gordon J.P. et al. (1954) *Molecular Microwave Oscillator and New Hyperfine Structure in the Microwave Spectrum of NH_3*, **Physical Review 95**, pp.282-284

Gordon J.P. (1986) *Theory of soliton self-frequency shift*, **Optics Letters 11**, pp.662-664

Hargrove L.E. et al. (1964) *Locking of He-Ne Laser Modes Induced by Synchronous Intracavity Modulation*, **Applied Physics Letters 5**, pp.4-5

Harris S.E. (1973) *Generation of Vacuum-Ultraviolet and Soft-X-Ray Radiation Using High-Order Nonlinear Optical Polarizabilities*, **Physical Review Letters 31**, pp.341-344

Harris S.E. and Sokolov A.V. (1997) *Broadband spectral generation with refractive index control*, **Physical Review A 55**, pp.R4019-R4022

Harris S.E. and Sokolov A.V. (1998) *Subfemtosecond Pulse Generation by Molecular Modulation*, **Physical Review Letters 81**, pp.2894-2897

Hecht E. (2002) *Optics Fourth Edition*, Addison Wesley, San Francisco CA (USA)

Hentschel M. et al. (2001) *Attosecond metrology*, **Nature 414**, pp.509-513

Herzberg G. (1945) *Molecular Spectra and Molecular Structure II. Infrared and Raman Spectra of Polyatomic Molecules*, D. Van Nostrand Company Inc., Princeton, NJ (USA)

http://cnyack.homestead.com/files/modulation/modfm.htm; **Java applet describing FM radio**

http://www.newport.com/store/genproduct.aspx?id=141092&lang=1033&Section=Spec; **BD.1 curve**

Imasaka T. et al (1989) *Generation of More Than 40 Laser Emission Lines from the Ultraviolet to the Visible Regions by Two-Color Stimulated Raman Effect*, **Applied Physics B 49**, pp.389-392

Janszky J. et al (1977) *On a Possibility of Analysing the Temporal Characteristics of Short Light Pulses*, **Optics Communications 23**, pp.293-298

Johnson F.M. et al (1967) *Complex Stimulated Raman Vibrational-Rotation Spectra in Hydrogen*, **Applied Physics Letters 10**, 157-160

Kalosha V.P. and Herrmann J. (2000) *Phase Relations, Quasicontinuous Spectra and Subfemtosecond Pulses in High-Order Stimulated Raman Scattering with Short-Pulse Excitation*, **Physical Review Letters 85**, pp.1226-1229

Kalosha V.P. and Herrmann J. (2003) *Ultrawide spectral broadening and compression of single extremely short pulses in the visible, uv-vuv, and middle infrared by high-order stimulated Raman scattering*, **Physical Review A 68**, art.023812

Kaplan A.E. (1994) *Subfemtosecond Pulses in Mode-Locked 2π Solitons of the Cascade Stimulated Raman Scattering*, **Physical Review Letters 73**, pp.1243-1246
Kaplan A.E. and Shkolnikov P.L. (1996) *Subfemtosecond pulses in the multicascade stimulated Raman scattering*, **Journal of the Optical Society of America B 13**, pp.347-354
Kato M. (2006) *Wavelength-Tunable Multicolor Raman Soliton Generation Using an Ellipse Polarized Pump Pulse and Highly Birefringent Optical Fibers*, **Journal of Lightwave Technology 24**, pp.805-809
Kienberger R. et al. (2004) *Atomic transient recorder*, **Nature 427**, pp.817-821
Kinsler P. and New G. H. C. (2005) *Wideband pulse propagation: Single-field and multifield approaches to Raman interactions*, **Physical Review A 72**, art.033804
Knox W.H. et al. (1985) *Optical pulse compression to 8 fs at a 5-kHz repetition rate*, **Applied Physics Letters 46**, pp.1120-1121
Kolmeder C. et al (1979) *Second Harmonic Beam Analysis, a Sensitive Technique to Determine the Duration of Single Ultrashort Laser Pulses*, **Optics Communications 30**, pp.453-457
Korn G. et al (1998) *Observation of Raman Self-Conversion of fs-Pulse Frequency due to Impulsive Excitation of Molecular Vibrations*, **Physical Review Letters 81**, pp.1215-1218
Lacovara P. et al. (1985) *Growth, Spectroscopy, and Lasing of Titanium-Doped Sapphire*, **IEEE Journal of Quantum Electronics QE-21**, pp.1614-1615
Liang J.Q. et al (2000) *Sideband Generation Using Strongly Driven Raman Coherence in Solid Hydrogen*, **Physical Review Letters 85**, pp.2474-2477
Losev L.L. and Lutsenko A.P. (1993) *Parametric Raman laser with a discrete output spectrum equal in width to the pump frequency*, **Quantum Electronics 23**, pp.919-926
Losev L.L. and Lutsenko A.P. (1996) *Ultrabroadband parametric stimulated Raman scattering in a highly transient regime*, **Optics Communications 132**, pp.489-493
Losev L.L. et al (2002a) *The influence of beam diffraction on multifrequency parametric Raman generation*, **Optics Communications 204**, pp.379-383
Losev L.L. et al (2002b) *Multifrequency parametric infrared Raman generation in $KGd(WO_4)_2$ crystal with biharmonic ultrashort-pulse pumping*, **Optics Letters 27**, pp.2100-2102
Maiman T.H. (1960) *Simulated Optical Radiation in Ruby*, **Nature 187**, pp.493-494
Maiman T.H. et al. (1961) *Stimulated Optical Emission in Fluorescent Solids. II. Spectroscopy and Stimulated Emission in Ruby*, **Physical Review 123**, pp.1151-1157
Maine P. et al. (1988) *Generation of Ultrahigh Peak Power Pulses by Chirped Pulse Amplification*, **IEEE Journal of Quantum Electronics 24**, pp.398-403
Maker P.D. and Terhune R.W. (1965) *Study of Optical Effects Due to an Induced Polarization Third Order in the Electric Field Strength*, **Physical Review 137**, pp.A801-A818
Marcatili E.A.J. and Schmeltzer R.A. (1964) *Hollow Metallic and Dielectric Wave-guides for Long Distance Optical Transmission and Lasers*, **Bell System Technical Journal 43**, pp.1783-1809
McClung F.J., and Hellwarth R.W. (1962) *Giant Optical Pulsations from Ruby*, **Journal of Applied Physics 33**, pp.828-829
McDonald G.S. et al (1994) *Ultrabroad-bandwidth multifrequency Raman generation*, **Optics Letters 19**, pp.1400-1402
McDonald G.S. (1995) *Ultrabroad-bandwidth multifrequency Raman soliton pulse trains*, **Optics Letters 20**, pp.822-824
Mennicke H. et al (1976) *Tunable High Order Stimulated Raman-Anti-Stokes Radiation Produced by Light Mixing*, **Physics Letters A 57**, pp.477-479
Minck R.W. et al (1966) *Nonlinear Optics*, **Proceedings of the IEEE 54**, pp.1357-1374
Mohebbi M. (2004) *Dispersion of femtosecond laser pulses in hollow fibers*, **Journal of the Optical Society of America B 21**, pp.893-896
Nazarkin A. et al (1999a) *Generation of Multiple Phase-Locked Stokes and Anti-Stokes Components in an Impulsively Excited Raman Medium*, **Physical Review Letters 83**, pp.2560-2563
Nazarkin A. and Korn G. (1999b) *Pulse Self-Compression in the Subcarrier Cycle Regime*, **Physical Review Letters 83**, pp.4748-4751
Nazarkin A. et al (2002a) *All-linear control of attosecond pulse generation*, **Optics Communications 203**, pp.403-412
Nazarkin A. et al (2002b) *Group-velocity-matched interactions in hollow waveguides: Enhanced high-order Raman scattering by impulsively excited molecular vibrations*, **Physical Review A 65**, art.041802
Nisoli M. et al. (1996) *Generation of high energy 10 fs pulses by a new pulse compression technique*, **Applied Physics Letters 68**, pp.2793-2795
Perry M.D. et al. (1999) *Petawatt laser pulses*, **Optics Letters 24**, pp.160-162
Rauschenberger J. et al (2006) *Carrier-envelope phase-stabilized amplifier system*, **Laser Physics Letters 3**, pp.37-42

Sali E. et al (2004) *High-order stimulated Raman scattering in a highly transient regime driven by a pair of ultrashort pulses*, **Optics Letters 29**, pp. 495-497
Sali E. et al. (2005) *Behaviour of high-order stimulated Raman scattering in a highly transient regime*, **Physical Review A 72,** art.013813
Schmidt W. and Appt W. (1974) *Generation of Tunable IR-Radiation Using a Dye Laser Pumped Raman Laser with Low Threshold*, **IEEE Journal of Quantum Electronics 10**, p.792
Seka W. et al. (1980) *High-power phosphate-glass laser system: design and performance characteristics*, **Applied Optics 19**, pp.409-419
Shon N.H. et al (2002) *Two-dimensional model for femtosecond pulse conversion and compression using high-order stimulated Raman scattering in solid hydrogen*, **Physical Review A 65**, art.033809
Shverdin M.Y. et al (2005) *Generation of a Single-Cycle Optical Pulse*, **Physical Review Letters 94**, art.033904
Siegman A.E. (1986) *Lasers*, University Science Books, Mill Valley CA (USA)
Sokolov A.V. et al (2000) *Raman Generation by Phased and Antiphased Molecular States*, **Physical Review Letters 85**, pp.562-565
Sokolov A.V. et al (2001) *Femtosecond Light Source for Phase-Controlled Multiphoton Ionization*, **Physical Review Letters 87**, art.033402
Speck D.R. et al. (1981) *The Shiva Laser-Fusion Facility*, **IEEE Journal of Quantum Electronics QE-17**, pp.1599-1619
Spiegel M.R. and Liu J. (1999) *Schaum's Outlines: Mathematical Handbook of Formulas and Tables Second Edition*, p.151, McGraw-Hill (USA)
Steinmeyer G. and Stibenz G. (2006) *Generation of sub-4-fs pulses via compression of a white-light continuum using only chirped mirrors*, **Applied Physics B 82**, pp.175-181
Strickland D. and Mourou. G. (1985) *Compression of Amplified Chirped Optical Pulses*, **Optics Communications 55**, pp.447-449
Svelto O.; Translated by Hanna D.C. (1998) *Principles of Lasers Fourth Edition*, Plenum Press, New York NY (USA)
Syed K.S. et al (2000) *Transverse effects in ultrabroadband multifrequency Raman generation*, **Journal of the Optical Society of America B 17**, pp.1366-1374
Terhune R.W. (1963), **Bull. Am. Phys. Soc. 8**, p.359 *as quoted in [Maker 1965]*
Treacy E.B. (1969) *Optical Pulse Compression With Diffraction Gratings*, **IEEE Journal of Quantum Electronics QE-5**, pp.454-458
Turner F.C. et al (2006) *Transient Multi-frequency Raman Generation in SF_6*, **Optics Communications**, doi:10.1016/j.optcom.2006.09.021
Wittmann M. et al (2000) *fs-Pulse Synthesis Using Phase Modulation by Impulsively Excited Molecular Vibrations*, **Physical Review Letters 84**, pp.5508-5511
Wittmann M. et al (2001) *Synthesis of periodic femtosecond pulse trains in the ultraviolet by phase-locked Raman sideband generation*, **Optics Letters 26**, pp.298-300
Wynne J.J. (1972) *Nonlinear Optical Spectroscopy of $\chi^{(3)}$ in $LiNbO_3$*, **Physical Review Letters 29**, pp.650-653
Xia J.F. et al (2002) *Development of a dual-wavelength Ti:sapphire multi-pass amplifier and its application to intense mid-infrared generation*, **Optics Communications 206**, pp.149-157
Xia J.F. et al (2003) *Experimental observation of Raman chirped adiabatic rapid passage*, **Journal of Physics B 36**, pp.L409-L414
Yamashita M. (2006) *Quasi-Automatic Phase-Control Technique for Chirp Compensation of Pulses With Over-One-Octave Bandwidth – Generation of Few- to Mono- Cycle Optical Pulses*, **IEEE Journal of Selected Topics in Quantum Electronics 12**, pp.213-222
Yan Y-X et al (1985) *Impulsive stimulated scattering: General importance in femtosecond laser pulse interactions with matter, and spectroscopic applications*, **Journal of Chemical Physics 83**, pp.5391-5399
Yavuz D.D. et al (2000) *Eigenvectors of a Raman Medium*, **Physical Review Letters 84**, pp.75-78
Yavuz D.D. (2003) *Quasiperiodic Raman Technique for Ultrashort Pulse Generation*, **Physical Review Letters 91**, art.233602
Yoshikawa S. and Imasaka T. (1993) *A new approach for the generation of ultrashort optical pulses*, **Optics Communications 96**, pp.94-98
Zewail A.H. (1991) *Femtosecond Transition-state Dynamics*, **Faraday Discussions of the Chemical Society 91**, pp.207-237
Zewail A.H. (1995) in: *J. Manz and L. Wöste (Ed.), Femtosecond Chemistry Volume 1*, VCH Publishers, Inc. NY (USA) and VCH Verlagsgesellschaft mbH, Weinheim (Federal Republic of Germany), p.21
Zhang Z. et al (2000) *Dual-wavelength chirped-pulse amplification system*, **Optics Letters 25**, pp.581-583

Zhavoronkov N. and Korn G. (2002) *Generation of Single Intense Short Optical Pulses by Ultrafast Molecular Phase Modulation*, **Physical Review Letters 88**, art.203901